DR 0849-4

FOSSIL

DOE/MC/23248-2709
(DE89000994)

Development of a New Method for Improving Load Turndown in Fluidized Bed Combustors

Final Report

R.C. Brown

December 1988

Work Performed Under Contract No.: DE-AC21-86MC23248

For
U.S. Department of Energy
Office of Fossil Energy
Morgantown Energy Technology Center
Morgantown, West Virginia

By
Iowa State University
Ames, Iowa

DISCLAIMER

DISCLAIMER

Price: Printed Copy A05
Microfiche A01

Printed in the United States of America, Office of Scientific and Technical Information, Oak Ridge , Tennessee

DOE/MC/23248-2709
(DE89000994)
Distribution Category UC-103

Development of a New Method for Improving Load Turndown in Fluidized Bed Combustors

Final Report

R.C. Brown

Work Performed Under Contract No.: DE-AC21-86MC23248

For
U.S. Department of Energy
Office of Fossil Energy
Morgantown Energy Technology Center
P.O. Box 880
Morgantown, West Virginia 26507-0880

By
Iowa State University
Ames, Iowa 50010

December 1988

TABLE OF CONTENTS

I.	Executive Summary	1
II.	Background	2
	A. Statement of Problem	2
	B. Objective of Research	2
	C. Scientific Basis	2
III.	Technical Approach	5
	A. Computational Model	5
	B. Heat Transfer Experiments	6
	C. Combustion Experiments	6
IV.	Computational Model	7
	A. Development	7
	B. Model Predictions	12
V.	Experimental Apparatus and Procedures	13
	A. High Temperature Heat Transfer Apparatus	13
	B. Cold Flow Model	17
	C. Combustion Apparatus	21
VI.	Results and Discussions	24
	A. High-Temperature Heat Transfer	24
	B. Cold Flow Model	27
	C. Combustion Tests	28
VII.	Conclusions	30
VIII.	References	31
IX.	Nomenclature	33
X.	Appendix	72

List of Figures

Fig. 1. Heat transfer and combustion rate vs. gas velocity.

Fig. 2. Schematic of a two-bed combustor.

Fig. 3. Effect of particle sizes on load turndown.

Fig. 4. Effect of annular bed width on load turndown.

Fig. 5. Schematic of high temperature heat transfer model.

Fig. 6. Top view of test bed: Large Insert.

Fig. 7. Top view of test bed: Small Insert.

Fig. 8. Piping schematic for test bed.

Fig. 9. Close-up view of thermocouple attachment in central bed.

Fig. 10. Side view of test bed showing heat exchanger core and LP-gas burner.

Fig. 11. Orifice plate flow meter assembly.

Fig. 12. Detail of flow metering system.

Fig. 13. Typical power vs. wire temperature curve.

Fig. 14. Schematic of experimental apparatus.

Fig. 15. Correction factor curve.

Fig. 16. Schematic of fluidized bed combustor.

Fig. 17. Experimental apparatus.

Fig. 18. Effect of bed particle size.

Fig. 19. Effect of particle thermal conductivity.

Fig. 20. Effect of annular bed width on UA (experimental data).

Fig. 21. Error in convection coefficient due to heat conduction along thermocouple wires.

Fig. 22. Comparison of predicted and experimentally determined wire temperature.

Fig. 23. Convection coefficients for 250 μm sand.

Fig. 24. Convection coefficients for 510 μm sand.

Fig. 25. Convection coefficients for 1000 μm sand.

Fig. 26. Effect of annular bed velocity on overall heat transfer coefficients.

Fig. 27. Combustion bed temperature vs. coal feed rate.

Fig. 28. Sulfur retention vs. combustion bed temperature.

Fig. 29. Nitrogen oxide emission vs. combustion bed temperature.

Fig. 30. Combustion rate vs. annular air flow rate.

List of Tables

Table 1. Granulated material used in Task 1.

Table 2. Granulated material used in Task 2.

Table 3. Analysis of Illinois No. 5 Rapatee Coal.

Table 4. Comparison of calculated and measured bed temperatures.

Table 5. Comparison of maximum convection coefficients for 1000 μm sand.

Table 6. Turndown test results for crushed coal.

Table 7. Turndown test results for briquettes.

Table 8. Turndown test results for CWLM.

I. Executive Summary

Fluidized bed combustion has grown with the prospect that it can burn coal and low grade fuels in an environmentally acceptable manner. Among the technical problems that exist, however, is the inherent inability to produce large variations in heat transfer rate from the fluidized bed. Generally, changes in heat transfer rate (or load turndown control) by conventional means are modest and are accompanied by degradation in combustion.

The objective of this research was to investigate a new concept in fluidized bed design that improves load turndown capability. This improvement is accomplished by independently controlling heat transfer and combustion in the combustor. The design consists of two fluidized beds, one central and one annular. The central bed serves as the combustion bed. The annular bed is fluidized separately from the combustion bed and its level of fluidization determines the overall heat transfer rate from the combustion bed to the surrounding water jacket. Early theoretical considerations suggested a load turndown exceeding ten was possible for this design.

This research consisted of three major phases; development of a computational model to predict heat transfer in the two-bed combustor, heat transfer measurements in hot-and-cold flow models of the combustor, and combustion tests in an optimally designed combustor.

The computational model was useful in selecting the design of the combustor. Annular bed width and particle sizes were chosen with the aid of the model.

The heat transfer tests were performed to determine if the existing correlations for fluidized bed heat transfer coefficients were sufficiently accurate for high aspect ratio fluidized beds (such as the annular bed in the combustor). Results of the heat transfer tests showed that heat transfer coefficients were generally higher than predicted by theory and existing correlations.

Combustion tests were performed in an optimally designed combustor. Three fuel forms were used: double screened, crushed coal, coal-water-limestone mixtures (CWLM), and coal-limestone briquettes. A load turndown (ratio of maximum fuel feed rate to minimum fuel feed rate) of 12.3 was obtained while burning crushed coal. Slightly lower load turndowns were observed for the coal-water-limestone mixture and coal-limestone briquettes. Sulfur dioxide emission reduction of 42% to 93% was observed for a fuel Ca/S ratio of 2.0. Both SO_2 and NO_x emissions met or exceeded EPA New Source Performance Standards of 0.20 to 0.34 kg/GJ. Computer model predictions were in reasonable agreement with experimental observations.

II. Background

A. Statement of Problem

Fluidized bed combustion (FBC) has grown with the prospect that it can burn coal and lov grade fuels in an environmentally acceptable manner. Long fuel residence times in fluidized beds provide fuel flexibility. Use of inexpensive sorbents for bed material reduces emissions of sulfur dioxide. Staged firing reduces emissions of nitrogen oxides. Unfortunately, technical problems remain that must be overcome before wider markets are developed. Prominent among these difficulties is the poor load turndown capability of fluidized bed combustors. Inherent to conventional FBC designs is an inability to produce larger variations in heat transfer rate from the fluidized bed. Generally, changes in heat transfer rate are modest and are accompanied by degradation in combustion. Innovative concepts in bed design are required to control heat transfer independently of combustion. This capability is especially important for fluidized beds targeted for coal-fired gas turbine power systems and small-scale boilers and furnaces.

B. Objective of Research

The objective of this research is to investigate a new concept in fluidized bed design that improves load turndown capability. This improvement is accomplished by independently controlling heat transfer and combustion in the combustor. The goal of this research is to develop a fluidized bed combustor with turndown ratio exceeding ten.

C. Scientific Basis

Heat transfer from a fluidized bed to water tubes is determined by three factors:

1. The temperature gradient between bed and water.
2. The heat transfer area.
3. The overall heat transfer coefficient between bed and water.

Boiler application usually sets the water-side temperature; attempts to control load with temperature gradients require large variations in bed temperature. However, even small variations in bed temperature from optimum design values will greatly degrade both sorbent utilization (Roberts, 1975) and combustion efficiency (Anson, 1976). Reduction of heat transfer area has been suggested as a method for reducing loads in FBC. This condition can be accomplished by either reducing fluidization velocity, which contracts bed volume, or discharging bed material. The former approach is of little practical value because bed contraction is limited to about 30% (Kunii and Levenspiel, 1979); the corresponding load turndown is modest at best. Discharging, storing, and reinjecting hot particles is fraught with many technical difficulties and has

little to recommend as a method for load turndown. In addition to the above difficulties, both methods for reducing heat transfer area will expose tubes to erosion when they are in the splash zone of the bed. Another method for reducing heat transfer area requires the air distributor to be partitioned which allows zones of the bed to be independently fluidized. Load turn down is achieved by selectively slumping part of the bed. Heat transfer area in defluidized zones is effectively zero. This technique has some undesirable effects on combustion including fuel smoldering and agglomeration in the slumped regions. Although bed slumping is frequently employed in commercial FBC units, turndown capability is rather modest.

Variation of the overall heat transfer coefficient between bed and tubes can also be employed for load turndown control. Heat transfer coefficients in fluidized beds show large variation with fluidization velocity; in principle, turndown ratios exceeding ten can be achieved by reducing fluidization velocity from its maximum heat transfer value to the minimum fluidization condition. However, as Figure 1 illustrates, the dependence of heat transfer coefficient on fluidization velocity is strongly non-linear; since combustion rate is proportional to fluidization velocity, a match between heat release and heat transfer rates is difficult to achieve. Horio et al., 1985, have developed a baffled heat transfer tube with the goal of achieving a linear response in average heat transfer coefficient with changes in fluidization velocity. Although they were successful in obtaining a linear response in the velocity range of 0.3 to 0.5 m/s, this achievement represents only a modest turndown ratio. It is far from evident that a sufficiently linear response can be achieved over larger velocity intervals. In addition, the baffle arrangements produce a linear response at great sacrifice in heat transfer rates; tube surface area might have to be increased by as much as 100%.

A more promising approach to improved load turndown is control of heat transfer rate independent of combustion rate. Iowa State University is preparing a patent disclosure on an invention that embodies such an approach. The device as described here can be employed in fluidized beds that remove heat around the perimeter of the bed, i.e., water jackets or water wall construction; however, the principle can also be applied to any vertical water tube design. Independent control of heat transfer rate and combustion rate is accomplished by surrounding the fluidized bed in which fuel is burned, hereafter called the combustion bed, by another fluidized bed, hereafter called the heat transfer bed, that establishes the overall heat transfer rate from the inner combustion bed. The two beds, physically divided by a wall, are fluidized independently by separate air plenums.

Figure 2 illustrates the device in a water jacketed, cylindrical fluidized bed. The central combustion bed is provided with fluidization air through a circular distributor plate from an air plenum which is designed to give even distribution of air through the bed. Coal or other fuel is fed into the combustion bed at a rate determined by the desired heat generation rate while air flow into this bed is set consistent with good combustion. The heat transfer bed is the annular fluidized bed surrounding the combustion bed. The two beds are separated by a wall constructed of heat resistant material of reasonably high thermal conductivity. Stainless steel is an appropriate choice but other materials may also be suitable. The heat transfer bed is supplied with fluidization air from a plenum separate from the combustion bed plenum. The heat transfer bed is enclosed by a water jacket that removes heat from the

combustor in the form of hot water or steam. Overall heat transfer rate from the combustion bed to the water jacket is determined by the heat transfer coefficients associated with the boundary layer of the combustion bed, the conductivity of the wall separating the beds, the boundary layers at the inner and outer diameters of the heat transfer bed, the conductivity of the water jacket wall, and the boundary layer of the water in the jacket. However, control of the overall heat transfer rate will reside in the heat transfer bed and will be accomplished by changing the fluidization velocity of air entering this outer bed. The combustion bed can be operated in Region A of Figure 1 where heat transfer rate is only a weak function of fluidization velocity--air flow rate to this bed can be chosen consistent with good combustion and independent of heat transfer considerations. The heat transfer bed can be operated in region B where large variations in heat transfer rate can be achieved. If no air is passed through the heat transfer bed, then it has the poor heat transfer characteristics of packed granular beds. If only sufficient air is passed through the heat transfer bed to just fluidize it, then increased heat transfer due to convection occurs. Heat transfer continues to increase as air flow increases until enhanced heat transfer characteristic of bubbling fluidized beds is reached; the result is a continuous and large variation in heat transfer rate from the combustor that is controlled independently of combustion rate. The performance of this heat transfer bed depends on such factors as fluidization velocity, bed material composition and particle size, width of the bed, and construction of the wall separating the two beds. A simple analysis provides an estimate of the load turn-down capability of this device.

Let q be the heat transfer per unit wall area of the combustor. The load turndown that can be achieved is the ratio of q for full fluidization of the heat transfer bed to q for the slumped heat transfer bed. For steady state operation of the combustor, the maximum heat transfer from the combustion bed can be approximated by

$$q_{max} = \left(\frac{1}{h_C} + \frac{2}{h_H} + \frac{1}{h_W}\right)^{-1} (T_C - T_W) \qquad (1)$$

where h_C = heat transfer coefficient for the combustion bed
h_H = heat transfer coefficient for the heat transfer bed
h_W = heat transfer coefficient for the water
T_C = temperature in combustion bed
T_W = temperature in water jacket.

In deriving this equation it is assumed that the combustion and heat transfer beds are uniform in temperature due to vigorous mixing. In addition, the heat transfer bed is assumed to be deep compared to its radial dimension; hence, heat loss associated with energy convected out of the heat transfer bed with fluidization air is relatively small. This simplification produces an approximately 20% underestimate in the turn down ratio for the calculations that follow. In the case of minimum heat transfer from the combustor, the heat transfer bed is completely defluidized:

$$q_{min} = \left(\frac{1}{h_C} + \frac{\Delta x}{k} + \frac{1}{h_W}\right)^{-1} (T_C - T_W) \qquad (2)$$

where k = thermal conductivity of (unfluidized bed material)
Δx = width of heat transfer bed.

Further simplification is obtained if it is assumed, for the maximum heat transfer condition, that the beds are equally fluidized and employ identical bed material. If boiling heat transfer is employed in the water jacket, then

$$h_H = h_C \ll h_W \tag{3}$$

For the minimum fluidization condition

$$\frac{k}{\Delta x} \ll h_C \ll h_W \tag{4}$$

hence, the turn down ratio can be approximated by the expression

$$\frac{q_{max}}{q_{min}} = \frac{1}{3}\frac{h_C \Delta x}{k} \tag{5}$$

For a 2.5 cm wide heat transfer bed of sand a typical fluidized bed heat transfer coefficient of 325 W/m^2K, turndown ratios exceeding ten are possible.

The energy convected out of the heat transfer bed with fluidization air does not represent heat loss from the combustor; it can be covered by heat exchange or employed in preheating fluidization air for the combustion bed or in staged combustion in the freeboard (Gibbs, et al., 1977). These applications will be investigated in this study.

III. Technical Approach

The technical approach to this project consisted of three major phases:

A. Development of a computational model that predicts heat transfer in the combustor.

B. Experimental measurements of heat transfer in the new bed geometry.

C. Coal combustion tests in an optimally designed combustor.

A. Computational Model

The ability to predict heat transfer rate through the concentric fluidized beds is important for evaluating different combustor designs and selecting operating conditions for a variety of combustion applications. The computational model was developed for this purpose. It can be used to determine the effect on load turndown of such variables as annular bed

width, annular bed particle size and composition, and air flow rates. Model predictions were used to design the combustor.

B. Heat Transfer Experiments

Heat transfer experiments were performed to investigate the parameters which affect the load turndown capability of the two-bed combustor and to validate the computer model. The parameters of interest deal mainly with the annular heat transfer bed

- air velocity
- bed particle size
- bed width

The values of these parameters were varied and the effect on heat transfer coefficients and load turndown capability determined.

Two different methods of heat transfer measurement were used:

1. Heat transfer measurements in a high-temperature two-bed configuration.

2. Heat transfer measurements in a cold-flow model of high-aspect-ratio fluidized beds.

The high temperature model was used to determine load turndown and heat transfer coefficients at simulated combustion conditions. Preheated air entered the center bed and thermocouple measurements were performed.

The cold flow model employs resistance-wire-wrapped surface in order to measure local convection coefficients in the fluidized bed. The experiments provide a more fundamental understanding of the unique flow characteristics of high aspect-ratio (height-to-width ratio) fluidized beds.

C. Combustion Experiments

Combustion tests were performed in an optimally-designed combustor to determine load turndown and operating characteristics while burning various coal-based fuels. The combustor was instrumented to measure temperatures and flow rates for air, water, and fuel. Gas analyzers were used to determine exhaust gas composition. Sulfur dioxide and nitrogen oxide emissions and combustion efficiency were determined as fuel type and operating conditions were varied.

IV. Computational Model

The computational model simulates heat transfer in the two-bed fluidized combustor. The model is used to predict combustion bed temperature, heat transfer rates in the combustor, and load turndown for varying operating conditions. These conditions include annular bed width, annular bed particle size, annular bed air flow velocity, and firing rate.

A. Development

Several assumptions were employed in model development:

- The central combustion bed is at a uniform temperatures, T_B, due to vigorous mixing and large thermal mass.
- The annular bed is also at a uniform temperature, T_p.
- Steady state conditions exist in the combustor.
- The heat of combustion released in the combustion bed, Q_{in}, is released uniformly in the bed.
- Boiling occurs at the water jacket wall and the water temperature at the wall surface is T_{sat} (saturation temperature).
- Heat conduction occurs normal to wall surfaces.
- Inside wall (wall between central and annular beds) and water jacket wall are at uniform temperatures, T_{iw} and T_{ow}, respectively.
- Heat flow from the annular bed is restricted to the water jacket and the air flow through the annular bed.
- Properties of air are used for exhaust gases exiting the central bed.

The mathematical formulation of the model consists of a system of non-linear algebraic equations describing heat transfer in the combustor due to convection, radiation, and boiling. These equations are:

Combustion bed temperature

$$T_b = \frac{Q_{in} + \rho_o u_o \bar{c}_{p_o} A_c T_o + \pi D_c H_j (h_b + u_{biw}) T_{iw}}{\rho_o u_o \bar{c}_{p_o} A_c + \pi D_c H_j (h_b + u_{biw})} \tag{6}$$

Inside wall temperature

$$T_{iw} = \frac{(h_b + u_{biw}) T_b + h_{gc} T_g + (h_{pc} + u_{piw}) T_p}{(h_b + u_{biw}) + h_{gc} + (h_{pc} + u_{piw})} \tag{7}$$

Annular bed temperature

$$T_p = \frac{\rho_o u_{g_c} \bar{c}_{p_g} A_{ann} T_o + \pi H_j D_c (h_a + u_{piw}) T_{iw} + \pi H_j D_a (h_a + u_{pow}) T_{ow}}{\rho_o u_{g_c} \bar{c}_{p_g} A_{ann} + \pi H_j D_c (h_a + u_{piw}) + \pi H_j D_a (h_a + u_{pow})} \tag{8}$$

Water jacket wall temperature

$$T_{ow} = \frac{(h_{pc} + u_{p_{ow}}) T_p + h_{gc} T_g - q_b''}{(h_{pc} + u_{p_{ow}}) + h_{gc}} \tag{9}$$

Boiling water heat flux

$$q_b'' = B_o (T_{ow} - T_{sat})^3 \tag{10}$$

$$\text{where } D_c = \text{constant} = \mu_l h_{lg} \left[\frac{g(\rho_l - \rho_v)}{\sigma_b} \right]^{\frac{1}{3}} \left[\frac{c_{p_l}}{c_{sf} h_{fg} Pr_w} \right]^3 \tag{11}$$

Water temperature rise

$$\Delta T_w = \frac{\pi D_a H_j}{\dot{m}_w c_{p_w}} \tag{12}$$

Radiation heat transfer coefficients

$$u_{biw} = \frac{\sigma (T_{iw}^2 + T_b^2)(T_{iw} + T_b)}{\left(\frac{1}{\epsilon_b} + \frac{1}{\epsilon_{iw}} - 1 \right)} \tag{13}$$

$$u_{piw} = \frac{\sigma (T_{iw}^2 + T_p^2)(T_{iw} + T_p)}{\left(\frac{1}{\epsilon_p} + \frac{1}{\epsilon_{iw}} - 1 \right)} \tag{14}$$

$$u_{pow} = \frac{\sigma (T_{ow}^2 + T_p^2)(T_{ow} + T_p)}{\left(\frac{1}{\epsilon_p} + \frac{1}{\epsilon_{ow}} - 1 \right)} \tag{15}$$

The preceding equations apply when the annular bed is fluidized. When the annular bed is defluidized, a second set of equations describing conduction across a static bed of particles is used:

Energy released in central bed

$$Q_{IN} = \frac{\pi D_c^2 H_j}{4}\left[\frac{4}{D_c}(h_b + u_{b,w})(T_b - T_{iw}) + \rho_o u_o \bar{c}_{p_a}(T_b - T_o)\right] \tag{16}$$

Inner wall temperature

$$T_{iw} = \frac{(h_b + u_{b,w})T_b + \left[\frac{2k_s}{D_c \ln(\frac{D_c}{D_o})}\right] T_{ow}}{(h_b + u_{b,w}) + \left[\frac{2k_s}{D_c \ln(\frac{D_c}{D_o})}\right]} \tag{17}$$

Water wall temperature

$$T_{ow} = \left(\frac{q''}{B_c}\right)^{\frac{1}{4}} + T_{sat} \tag{18}$$

Boiling heat flux

$$q_b'' = \frac{Q_{COND}}{\pi D_o H_j} \tag{19}$$

Energy conducted across annular bed

$$Q_{COND} = Q_{IN} - \rho_o u_o \bar{c}_{p_a}(T_b - T_o)\frac{\pi}{4} D_c^2 \tag{20}$$

The fluidized bed convective heat transfer coefficients, h_B, h_{p_a}, h_{gp}, are found using the two-phase theory of fluidization described by Xavier and Davidson (1985). The bed convection coefficient, h_b, is composed of particle convection and gas convection:

$$h_b = h_{pc} + h_{gc} \tag{21}$$

The particle convection coefficient is calculated from a packet resistance in series with a film resistance:

$$h_{pc} = \frac{1 - \epsilon_b}{\left(\frac{1}{h_p} + \frac{1}{h_f}\right)} \tag{22}$$

The film coefficient is:

$$h_f = \frac{m k_g}{d_p} \tag{23}$$

The packet resistance is:

$$h_p = 2\left[\frac{k_{mf}\rho_{mf}c_{mf}(u-u_{mf})}{\pi L}\right] \tag{24}$$

where

$$L = 0.5d_b \tag{25}$$

and the product of density and specific heat of the emulsion phase is:

$$\rho_{mf}c_{mf} = \rho_s(1-\epsilon_{mf})c_s \tag{26}$$

The bubble diameter, d_B, can be calculated from

$$d_b = 0.54(u-u_{mf})^{0.4}[H_f + 4\sqrt{A_o}]^{0.8}g^{-0.2} \tag{27}$$

The bed voidage, ϵ_B, is found from

$$\epsilon_b = 1 - \frac{u_b}{u-u_{mf}+u_b} \tag{28}$$

The bubble rise velocity, U_B is calculated from

$$u_b = 0.71\sqrt{gd_b} \quad \text{if} \quad \frac{d_b}{D} < .125 \tag{29}$$

$$u_b = 0.802\sqrt{gd_b}\exp\frac{-d_b}{D} \quad \text{if} \quad .60 \geq \frac{d_b}{D} \geq .125 \tag{30}$$

$$u_b = 0.35\sqrt{gd_b} \quad \text{if} \quad \frac{d_b}{D} > .60 \tag{31}$$

The thermal conductivity of the emulsion phase, k_{mf}, is found from

$$k_{mf} = k_t^o + 0.1\rho_g c_g d_p u_{mf} \tag{32}$$

$$k_t^o = k_g\left[\left(\frac{k_s}{k_g}\right)^{(0.28-0.757\log\epsilon_s-0.057\log(k_s/k_g))}\right] \tag{33}$$

The minimum fluidization velocity, u_{mf}, can be estimated from

$$u_{mf} = \frac{25.7\mu_g}{\rho_g d_p}\left[(1 + 5.53 \times 10^{-5} Ar)^{0.5} - 1\right] \tag{34}$$

where the Archimedes number is given by

$$Ar = \frac{\rho_g(\rho_s - \rho_g)g d_p^3}{\mu_g^2} \tag{35}$$

The gas convective coefficient, h_{gc}, is calculated from a bed resistance in series with a wall resistance:

$$h_{gc} = \frac{1}{\left(\frac{1}{h_{av}} + \frac{1}{h_f}\right)} \tag{36}$$

The bed resistance is:

$$h_{av} = \left(\frac{4k_{mf}\rho_g c_g u}{\pi H_f}\right)^{0.5} \tag{37}$$

The wall resistance is approximately equal to the film resistance calculated previously

$$h_w = h_f \tag{38}$$

Finally, the gas-to-particle heat transfer coefficient, h_{gc}, is calculated from

$$Nu_{gc} = \frac{h_{gc} d_p}{k_g} = \left[2 + 1.1 Re_p^{0.6} Pr^{0.33}\right] \tag{39}$$

One additional condition is used in calculating heat transfer coefficients in the annular bed. Since the annular bed when fluidized is constrained on the top surface by a screen, there is a maximum height, H_{max}, to which the bed may expand. Therefore, once the bed expands to a height of H_{max}, the following condition applies:

$$\epsilon_{b_{max}} = 1 - \frac{H_{mf}}{H_{min}} \tag{40}$$

Once the steady state temperatures are found for the given conditions, the following heat transfer rates are calculated:

Heat transfer to water jacket

$$Q_{H_2O} = q_b'' H_j \pi D_o \tag{41}$$

Heat transfer to annular bed air

$$Q_{HTAIR} = \frac{\rho_o u_{g,o} \bar{c}_{p,g} \pi}{4}(D_c^2 - D_a^2)(T_g - T_o) \tag{42}$$

Heat transfer to central bed air

$$Q_{CAIR} = \frac{\rho_o u_{a,o} \bar{c}_{p,a} \pi}{4} D_c^2 (T_b - T_o) \tag{43}$$

Heat transfer from central to annular bed due to convection

$$Q_{CWALL} = \pi D_c H_j h_b (T_b - T_{iw}) \tag{44}$$

Heat transfer from central to annular bed due to radiation

$$Q_{CRAD} = \pi D_c H_j u_{b,w} (T_b - T_{iw}) \tag{45}$$

Energy released in central bed

$$Q_{IN} = Q_{CAIR} + Q_{CWALL} + Q_{CRAD} \tag{46}$$

Check on overall energy balance

$$Q_{IN} = Q_{H_2O} + Q_{HTAIR} + Q_{CAIR} \tag{47}$$

A listing of the FORTRAN computer code that was written to solve this system of equations appears in Appendix A. The main program contains the system of equations which are solved iteratively. The fluidized bed heat transfer coefficient equations are contained in the subroutine COEFF.

B. Model Predictions

The computer model was used to aid in preliminary design of the two-bed fluidized combustor. Specifically, it was used to determine the effect of annular bed width and annular bed particle size on load turndown. The load turndown is obtained as the ratio of maximum to minimum firing rates in the combustor at constant firing rate is obtained at the point where the central bed is just fluidized (incipient fluidization) with a static (defluidized) annular bed. It is assumed that 100% of the fuel is burned in the central bed; the firing rate is equivalent to energy released in the central bed.

The maximum firing rate is obtained by setting the annular bed air flow rate at the point of maximum convective heat transfer coefficient. The central bed air flow rate is set to obtain an expected maximum allowable gas velocity. For computational purposes this velocity is set at $U/U_{mf} = 6$. Since the combustion bed normally operates substoichiometrically, it is assumed that only 50% of the heat of combustion is released in the bed. The load turndown, then, is calculated as the ratio of twice the maximum Q_{in} to the minimum Q_{in}.

Simulations suggest that use of small particles will not have as dramatic effect on load turndown as might be expected. Fig. 3 demonstrates that reducing annular bed particle size from 1.0 mm to 0.3 mm increases load turndown from 8.3 to only 9.8 in the case of 1.0 mm particles in the combustion bed even though convection coefficients in the annular bed increase by a factor of two. As air flow through the annular bed becomes large, heat transfer in the combustion bed becomes rate-limiting to the overall heat transfer process. Consequently, the overall heat transfer rate between the combustion bed and the annular bed does not increase by a factor of two for this range of particle sizes. Nevertheless, there is an advantage in using small particles in the annular bed. We selected sand sieved to 50 x 70 mesh (0.25 mm average diameter) as the smallest practical bed material that could be employed in the annular bed. Smaller particles were too easily entrained in the gas flow by the action of gas bubbles bursting at the surface of the annular bed. It can also be seen from Fig. 3 that higher load turndowns are achieved with smaller particles by the combustor bed. A load turndown of 15 is predicted for 0.25 mm particles in the combustion bed. However, particles smaller than 1.0 mm are not practical in the combustion bed to prevent bed material elutriation. Therefore, 1.0 mm particles were used in the combustion bed to allow higher air velocities, and hence, higher fuel firing rates.

Simulations and experiments also clearly indicated the advantage of a wide annular bed for producing large turndowns. Results of simulations shown in Fig. 4 predict that load turndowns exceeding 15 can be achieved with an annular bed width of only 65 mm. However, the overall diameter of the combustor used in our experiments was constrained to 254 mm by the fixed dimensions of the waterjacket. Under this constraint, a large annular bed width would have produced an unreasonably small combustion bed volume. We selected a 25.5 mm width as large enough to achieve a targeted load turndown ratio of 10:1.

V. Experimental apparatus and procedure

A. High temperature heat transfer model

The high temperature test rig was constructed to measure load turndown and local fluidized convection coefficients under simulated combustion conditions. Figure 5 illustrates the test bed configuration. The experimental apparatus is divided into two major sections separated by the distributor plate. The upper section is the fluidized bed assembly which consists of the central fluidized bed, annular fluidized bed, and water-cooled jacket.

The lower section is the plenum section which supplies separately controlled flows for the fluidization of the beds.

Three grooves are machined in the distributor plate both top and bottom to accept three different sets of bed and plenum inserts. Variation in annular bed width is attained by selection of insert size. Fig. 6 shows a photograph of the water-jacketed section with the 8-inch bed insert installed, resulting in an annular bed width of 1 inch. Fig. 7 shows the water-jacketed section with the 5-inch insert, resulting in an annular bed width of 2.5 inches. The third set of inserts are 7 inches in diameter.

As seen in Fig. 5, the annular plenum supplies air to the annular bed. The central plenum provides hot combustion gases to the central bed. The combustion gases are produced from a diffusion flame which is supported on a torch external to the plenum section. Separate supplies of L-P gas and compressed air are delivered to the burner. L-P gas is stored in a tank while combustion air is supplied from a compressed air line. The L-P gas and combustion air are independently regulated before mixing in the burner. A spark is used for ignition of the burner flame. Figure 8 illustrates the piping arrangement for the L-P gas, combustion air, and secondary (annular) air.

The water level in the water jacket may be controlled by adjustment of the exit line height. Water level control is used to simplify energy balance calculations.

Twelve thermocouples were spot-welded to each bed insert. The chromel-alumel thermocouples were attached to both inside and outside surfaces of the insert at three equi-distant radial positions; and at one radial position, are attached at three elevations. Fig. 9 is a close-up view of the thermocouple attachment (with sand removed to expose the attachments). The short pieces of white ceramic tube serve as electrically insulating spacers to prevent thermocouple wire shorting.

Rather than attach a thermocouple bead to the wall, each lead of the thermocouple was individually spot-welded to the wall, leaving a 2 mm gap between the wires. Not only is this a simpler installation procedure, but it gives a more robust probe attachment and yields a more realistic wall surface at the point of temperature measurement. These simple wall probes have proved durable in high-temperature shake-down runs although occasionally an interior weld will break. Temperature gradients, ΔT, across the insert wall are measured with high accuracy by wiring the inside and outside thermocouples at any wall position in series to give a voltage difference. Heat fluxes, q, are then calculated by the relationship

$$q = \frac{k\Delta T}{\Delta x} \tag{48}$$

where the thermal conductivity, k, for the AISI 304 stainless steel comes from the literature and the wall thickness, ΔX, was measured at all thermocouple locations with high-precision calipers. Thermocouples located within the beds allow heat transfer coefficients at wall surfaces to be calculated from

$$h = \frac{q}{T_{wall} - T_{\infty}} \tag{49}$$

where T_{wall} is the wall temperature on the side that h is to be determined and T_{∞} is the bed temperature. Thermocouples were also mounted on either side of the wall separating the water jacket from the annular bed; these are used to measure heat transfer coefficients at the outer circumference of the annular bed.

These thermocouples attached to the walls give local heat transfer coefficients. Additional thermocouples were placed in the apparatus to allow overall energy balances and heat transfer coefficients to be calculated as a check on system operation. Thermocouples are located in the gas plenums for both the central and annular beds. The hot gases in the central plenum unavoidably resulted in significant radiation from the wall enclosing the central plenum across the annular plenum. Accordingly, it was necessary to employ a radiation-corrected thermocouple in the annular plenum to get an accurate measure of secondary air temperature entering the annular plenum.

Care was taken in accounting for all energy fluxes leaving the hot, central bed. Most of the heat exited to the enclosing water jacket or was convected out with secondary air flow leaving the annular bed. However, radiation from the bed surface was not insignificant. It was decided that the simplest and most reliable approach to accounting for radiation was to install a finned-tube heat exchanger core at the exit of the central bed. This heat exchanger is visible in Fig. 10, mounted on top of the circular fluidized bed apparatus. It proved effective in intercepting all radiation from the central bed. By measuring the change in temperature and flow rate of the cooling water and the gas temperature exiting the heat exchanger core, an overall energy balance could be performed.

The LP-gas burner can also be seen in the lower left-hand corner of Fig. 10. The burner is designed to operate at close to stoichiometric air-to-fuel ratios; additional air required for fluidization enters the burner tube downstream of the stabilized flame. Air for the turbulent diffusion flame enters along the axis of the burner tube. Gas enters the burner tube from the side and flows through a circular ring of orifices that face upstream in the air flow. The burner tube is wrapped in Alfrax insulation which is held in place by metal foil.

During shake-down trials, an energy balance between the gas streams and the water flows agreed to within 20%. The source of discrepancy was traced to the conduction path between the hot distributor plate and the cold water jacket. A 1/4" thick gasket was formed from insulating material to reduce this heat transfer. Reliable LP-gas firing and data acquisition was also obtained during the shake-down trials. However, the threaded fittings between the bed inserts and external combustor tube tended to bind after operation at high temperature, so the threaded fittings were replaced with flanged fittings to ease disassembly of the bed.

Data Acquisition

A Zenith Z-158 microcomputer equipped with a 20 megabyte hard disk drive was used for data acquisition. The computer has four expansion slots for slide-in expansion boards. Three of the four slots were used in this project. One expansion slot was occupied by a 24-bit, parallel, digital input/output interface board (Metrabyte Model PIO-12). Two 8-channel, high speed, analog/digital converter interface boards (Metrabyte Model DAS-8) occupied the other two expansion slots.

Thermocouple measurements were performed using 3 analog input, expansion sub-multiplexer boards (Metrabyte Model EXP-16). This allowed a maximum of 48 thermocouple readings. The EXP-16 boards performed cold junction compensation and signal amplification, and were connected to the DAS-8 interface board.

Once analog signals were converted to digital data by the DAS-8 interface, the data were processed to obtain the desired output, namely temperatures and mass flow rates.

Temperature, pressure and flow rates were the primary quantities measured. Temperature measurements were made using chromel/alumel (type K) thermocouple wire for surface temperature measurements and chromel/alumel thermocouple probes for bulk fluid temperature measurements. For surface temperature measurements, the thermocouple wires were individually spot welded to the metal surfaces to form intrinsic thermocouple junctions. This method provided a more accurate measurement of the surface temperature as compared to attaching a thermocouple bead to the surface. In regions of high temperature, the thermocouple leads were electrically insulated by threading them through ceramic tubes.

Two airflows and one L-P gas flow were measured using orifice meters. Computer activated solenoid valves were used to allow multiple pressure readings from one pressure to transducer. Pressure taps from each orifice meter were connected to Humphrey Model M31E1 solenoid valves. The solenoid valves were activated by the computer using an electromechanical relay output accessory board (Metrabyte Model ERA-01). The relay board was connected to the PIO-12 interface board. A single pressure transducer (linear variable displacement transformer type) Schaevitz Model P3061, was used to measure the pressure drop across the orifice meter. The output signal of the transducer was connected to the DAS-8 analog/digital converter board. The orifice plates were constructed and calibrated in the laboratory. Fig. 11 shows a typical orifice plate assembly including pressure taps.

Fig. 12 illustrates schematically the arrangement for using a single pressure transducer to measure pressure drop through several orifice plates. The computer/data acquisition system controlled each valve's operation so that flow rate through any line could be determined.

The data acquisition system converted input signals from voltages to pressures and temperatures. Pressure data was further converted to flow rates for the orifice flow meters. Calibration of the orifice meters was performed using a laminar-flow air meter. The converted data was displayed

on the screen so that operating conditions could be observed as the system operated. In addition, data could be stored on floppy disk for later analysis.

Test Plan

Experiments were designed to determine overall heat transfer rates and local heat transfer coefficients in the annular fluidized bed as functions of particle size, particle thermal conductivity, bed width, bed temperature, and fluidization velocity. Experimental data were also used to determine combustion temperature as a function of firing rate and secondary air flow for comparison with model predictions.

Tests were performed with three different sizes of annular bed material. Table 1 shows the size and thermal conductivity of the screened river sand. The sand has a particle density of 2600kg/m^3.

The bulk material thermal conductivity was measured using an apparatus designed for determining thermal conductivity of small diameter particles. It consists of a water-cooled spherical shell surrounding a spherical heating element. The particles are poured through a small opening in the cooled shell and settle between the cooled shell and the heating element. The conductivity as a function of temperature is then determined from measuring power input to the heating element and shell surface temperatures. Bed width in this series of tests was 1.5 inches.

The effect of particle conductivity on load turndown was determined with the three materials in Table 2. All three materials had an average particle size of 1 mm.

It is interesting to note that although the conductivity of the three particles is expected to vary considerably, the measured conductivities are all of the same order of magnitude. Little variation is observed because even for large changes in particle conductivity, bulk conductivity is mainly a function of the contact resistance between individual particles (Krupiczka 1967).

Tests were also performed with the three insert sizes of 5, 7, and 8 inches to determine the effect of bed width on heat transfer and load turndown. Sand with a particle size of 1 mm was used in both the annular and central beds.

B. Cold Flow Model

The resistance-wire technique used in our study was developed by Romani and Richardson (1974). The method determines convection coefficients between an electrically heated surface and the surrounding fluidized bed. The apparent convection coefficient h_{app} is related to the electrical power P dissipated by the resistance-wire:

$$P = h_{app} A (T_w - T_b) \tag{50}$$

where A is the surface area of the wire-wrapped region, T_b is the bed temperature, and T_w is the wire temperature. It is assumed that the surface temperature of the wire-wrapped region is equal to the wire temperature.

Dissipated power can be calculated by measuring the voltage drop and current flow for the resistance wire. The resistance R of the wire can be calculated by using Ohm's law. The temperature of the wire can then be calculated using the relation

$$T_w = (R/R_o - 1)/\alpha + T_o \tag{51}$$

where R_o is the wire resistance at the reference temperature T_o. The temperature coefficient of resistivity a is found by measuring wire resistance as a function of temperature and evaluating the slope of a plot of these data.

Differentiating Eq. 51 with respect to current and voltage gives a relationship for the maximum error in wire temperature calculation due to uncertainty in the voltage and current measurements:

$$\Delta T = \frac{1}{R_o \alpha}\left[\frac{1}{I}\,|\,\Delta V\,| + \frac{V}{I^2}\,|\,\Delta I\,|\right] \tag{52}$$

Equation 50 reveals a linear relationship between the dissipated power and the wire temperature. For constant h_{app}, A, and T_b, power can be plotted against wire temperature to obtain a straight line. The x-intercept of the line gives the bed temperature T_b. The slope of the line is $h_{app}A$, from which the convection coefficient can be calculated (see Fig. 13).

In using Eq. 50 to calculate convection coefficients, we have made two key assumptions: (a) All the power is dissipated from the wire-wrapped region directly to the bed through convection, and (2) the surface temperature of the measurement area is equal to the wire temperature. In fact, some of the power is conducted away from the measurement region through the wall material. This conduction increases the apparent convection coefficients as determined by Eq. 50. In addition, temperature gradients on the surface of the wall between wires make the isothermal assumption a poor one. These temperature gradients decrease convection coefficients as determined by Eq. 50, which results in underestimation of actual bed-to-wall convection coefficients.

The systematic errors arising from conduction and surface temperature gradients can be accounted for in the following manner. Energy enters the wire-wrapped region in the form of electrical power P. The electrical energy is dissipated from the region by conduction through the wall, Q_{cond}, and by convection to the fluidized bed, Q_{conv}. The energy balance is expressed as

$$P = Q_{cond} + Q_{conv} \tag{53}$$

The convection term can be expressed as

$$Q_{conv} = h_{act} A(\bar{T} - T_b) \tag{54}$$

where $\bar{T}$ is the average surface temperature of the wire-wrapped region and h_{act} is the actual bed-to-wall convection coefficient. Substitution of Eqs. 50 and 54 into Eq. 53 results in the following expression relating the apparent convection coefficient to the actual convection coefficient.

$$\frac{h_{act}}{h_{app}} = \left(\frac{T_w - T_b}{\bar{T} - T_b}\right)\left(1 - \frac{Q_{cond}}{P}\right) \tag{55}$$

The first term on the right side of Eq. 55 corrects for the conduction through the solid, while the second term corrects for temperature gradients at the surface of the wall.

The values of T_b, P, and T_w are known for a given experiment. To determine h_{act}/h_{app}, we must also know $\bar{T}$ and Q_{cond}. These quantities are calculated by a finite difference model of heat transfer in the wall. This model is discussed in the next section after the geometry of the wall used in our experiments is described.

Fig. 14 shows a schematic of the experimental apparatus used in this study. Air at 90 psi is passed through a control valve and into a set of rotometers. The flow then enters a humidification chamber located downstream of the flowmeters. The humidifier consists of a 10-cm-I.D. plexiglas cylinder that is 30 cm long. The cylinder is partially filled with water. Air blown over the surface of the water is sufficiently humidified to eliminate static charge in the plexiglas fluidized bed. Static charge affects fluidization as well as interfering with the data acquisition system.

Air exiting the humidifier enters the plenum of the fluidized bed. A nozzle distributes air evenly into the plenum to reduce pressure gradients. Air enters the fluidized bed through a distributor plate drilled with 256 1-mm holes spaced 3 mm apart. A 70-mesh screen is installed above the distributor plate to prevent bed material from entering the plenum.

The freeboard, also constructed of plexiglas, has dimensions 15 cm x 10 cm x 60 cm. Grooves in the side walls allow spacer walls to be inserted. Thus, the aspect ratio of the fluidized bed can be varied. The aspect ratio is calculated as the static bed depth divided by the hydraulic diameter of the bed.

A 0.3-cm-thick test wall constructed of plexiglas is mounted in the center

of the freeboard. Attached to the test wall are three wire-wrapped regions located 10, 15, and 20 cm above the distributor plate. Each region consists of 12 turns of MWS alloy 120 resistance wire seated into grooves in the plexiglas. The grooves were accurately cut on 0.34 cm centers, approximately 0.8 mm deep, with a milling machine. The wire was wrapped around the wall and pressed into the grooves; as a result, the wires are nearly flush with the surface. Plexiglas cement was applied to seat the wires permanently into the grooves. This cement evaporated completely from the surface and left no residue on the wires that might interfere with heat transfer measurements.

A Zenith microcomputer equipped with a Metrabyte Dascon-1 interface board was used to control the experiment and acquire data. The Dascon-1 controls a Metrabyte digital relay board that activates one of three bands of resistance wire. The Dascon-1 also sends an analog signal (0-2mA) to a control circuit to regulate current to the activated band of resistance wire. The control circuit, constructed from an operational amplifier, outputs a current proportional to the input signal from the Dascon-1 in the range of 0 to 0.3 amps.

The Dascon-1 analog input channels are used to measure voltage drop across the bands of resistance wire as well as across ca calibrated resistor. The calibrated resistor is used to determine current flow through the resistance wire. The Dascon-1 measured voltages to 0.01 V and current to 0.0001 amp. At low power levels, $\Delta T/T$ was as high as 0.08; at high power levels, $\Delta T/T$ was less than 0.01.

Pressure drop across the fluidized bed was measured using a mercury manometer. The temperature of the bed was measured with a thermometer suspended in the bed that reads to within 0.25°C.

A control and data acquisition program was written to automate the experiment. For a given air flow rate, the control system incrementally steps through ten power settings that are applied, in turn, to each band of resistance wire. For each power setting and wire band, the data acquisition system measures current and voltage, which are used to calculate wire temperatures. A linear regression analysis of the power versus wire temperature data is performed for each band of resistance wire. Local convection coefficients at each band of wire and the bed temperature can then be calculated. At this point, systematic errors resulting from the measurement technique must be corrected.

A finite-difference model was developed to simulate the wire-wrapped wall. This computer model predicts the temperature distribution through a cross section of the wire-wrapped wall for a given power level, bed-to-wall convection coefficient, and bed temperature.

Two planes of symmetry exist in the cross section of the wire-wrapped wall. This enabled the dimensions of the computer model to be reduced by a factor of four. Two grid meshes were used to model the wall. The finer mesh was used in the region near the nodes that simulate wires. Away from the wire nodes, a coarser mesh was used. This decreased the total number of nodes required in the model by approximately 25%.

The wire cross sections were modeled with four isothermal nodes in a square pattern located at the surface of the wall. Contact resistance was added between the wire nodes and the adjacent wall nodes. The value of the contact resistance was determined by trial and error. Predictions of the numerical model were compared with a set of experimental data for 510 μm sand fluidized with 0.2 m/s of air at a power level of 1.5 watts per meter of wire in a bed with an aspect ratio of 17. The contact resistance was varied until the numerical model predicted wire temperature to within 1°C. The contact resistance was found to be $8 \times 10^{-5} m^2 k/W$. This resistance is assumed to be independent of temperature. Comparisons between other experiments and model predictions, described in the next section, were used to check this assumption.

A parametric study determined that the value of the correction factor h_{act}/h_{app} is independent of the input power and ambient temperature. Thus, by using the numerical model, values of h_{act}/h_{app} were calculated for various h_{app} values and plotted in Fig. 15. The two terms of Eq. 55 that determine the correction factor have also been plotted in Fig. 15. The term corresponding to conduction approaches unity as h_{app} increased. The term associated with temperature distribution increases linearly with h_{app}.

C. Combustion Apparatus

Tasks that were performed to prepare for combustion tests included coal sampling and fuel preparation, combustor design and instrument preparation, and performance of tests.

Coal sampling and fuel preparation

A 3200-pound bulk sample of coal was obtained from the Rapatee mine of the Midland Coal Company in Fulton County, Illinois. The sample consisted of freshly-mined, washed Illinois No. 5 seam coal, 1.5-inch in top-size. The coal was obtained directly from coal load-out facilities at the mine/preparation plant, covered with a tarpaulin, and transported to preparation facilities at Iowa State University.

Two representative bulk samples were obtained by cone-and-quartering from the 3100-pound bulk sample. One sample (1200 lb) was used for briquette and coal-water-limestone mixture (CWLM) preparation and the second sample (2000 lb) was crushed for dry coal tests.

The 1200 lb sample was ground in a Holmes model 45 impact pulverizer fitted with a 0.0625-inch perforated screen. This pulverizer produces a coal product with a top size of approximately 40 mesh (425 μm). This pulverized sample was then divided by riffling into equal portions and stored in plastic bags, under argon, in lined 55-gallon steel drums. An analytical sample was also obtained from the pulverized coal by splitting and grinding to minus 60 mesh (250 μm). The analysis was performed on this sample and the results are shown in Table 3.

The 2000-pound representative bulk sample was sieved to produce a particle

size range of approximately 3/8-inch by 8 mesh (2.36 mm by 0.95 mm). This size range was selected so that the largest particles could be accurately metered into the combustor with an auger feeder and that the smallest particles were large enough not to elutriate from the combustor. After sieving, oversize material was reduced in a Brawn 3-inch jaw crusher to obtain the largest quantity of material in the desired size range while producing a minimum of fines. Approximately 1200 pounds of 3/8-inch by 8 mesh coal resulted from this operation. An analytical sample of this screened coal was also prepared to determine if loss of fines changed the coal analysis. The analysis was performed and the results were not significantly different than those shown in Table 3 for the pulverized coal sample.

A 500-pound sample of Mississipian-age Gilmore City limestone was obtained from Ames, Iowa in Story County. It was prepared for use in briquettes and CWLM by crushing in a Holmes model 45 impact pulverizer fitted with a 0.0625-inch perforated screen. This crusher produced a limestone product with a top-size of about 20 mesh (0.85 mm).

Tests were performed to evaluate briquette forming parameters, including forming pressure, roll speed, screw speed, and binder composition and addition rate. Pre-gelatinized corn starch was selected for use in the binder. The binder was produced by mixing 22% by weight of corn starch in water in an electric blender. Limestone was mixed with the pulverized coal to produce a mixture with a calcium-to-sulfur (Ca/S) molar ratio of 2.0. Inherent calcium content in the coal accounts for about 10% of this limestone addition of 14.9 pounds per 100 pounds of "as-received" coal. The binder was then added to the coal-limestone mixture at the addition rate of 11% by weight. The briquettes were then prepared in a briquetting machine using a forming pressure of 1500 psi, a roll speed of 3, and a screw speed of 2-3. The moisture free composition of the briquettes was 83.2% moisture-free coal, 13.9% limestone, and 2.95 corn starch.

Coal-water-limestone mixture (CWLM) was prepared using the same limestone addition rate as for briquettes (Ca/S = 2.0). Limestone was added to the pulverized coal at an addition rate of 14.9% by weight. Water was then added at a rate of 1.13 pounds of water per pound of coal. The mixture was then stirred in an emulsifier-mixer powered by a 10-hp electric motor for 10 minutes. The resulting mixture had the following composition: 49.7% dry coal, 8.3% limestone, and 42% water. The solids loading was 58%. This was the highest attainable solids loading that produced an easily-pumpable mixture. Both the CWLM and briquettes were stored in sealed 5-gallon buckets until needed for combustion tests.

Combustor design and instrument preparation

Fig. 16 is a section view of the combustor constructed for coal-fired combustion trials. The combustor is constructed in four sections. The bottom section consists of separate plenum chambers serving the combustion and heat transfer beds. Air from these plenums flow through a common distributor plate into the water-jacketed section of the combustor. A smaller, insulated section was added immediately above the water- jacketed section. A stainless steel pipe, running the length of the water-jacketed and insulated sections, divides these combined sections into two concentric

beds: the (central) combustion bed and the (annular) heat transfer bed. Enough sand was added such that when the beds are fluidized, the bed height extends into the insulated bed section. This insulated bed section is not an integral part of the two-bed combustor; it was included in this test combustor to simplify energy balances on the combustion bed and allow us to evaluate overall heat transfer coefficients in the heat transfer bed. The fourth section of the combustor is a 1.2 m long freeboard cast on the inside with 2.54 cm of ceramic.

The central bed supports combustion and the annular bed is used to control heat transfer from the central bed to the water jacket. Air used to fluidize the annular bed is exhausted through nozzles to the combustor freeboard immediately above the combustion bed. This secondary flow of air supports combustion of volatiles and coal fines released from the fuel burning in the central bed. The eight nozzles located just above the central bed are positioned in such a manner as to impart swirl to the secondary air as it mixes with gas exiting the central bed. This arrangement, in addition to the insulated freeboard, should promote burn-up of coal volatiles and fines released to the freeboard.

Fig. 17 is a schematic diagram of the experimental apparatus used to perform the combustion experiments. Three air flows enter the combustor: primary air enters the central bed, secondary air enters the annular bed, and tertiary air enters the freeboard of the annular bed. Secondary air and tertiary air, taken together, represent overfire air required to burn volatiles and char that escape into the freeboard above the combustion bed. These air flows were read manually with rotameters or automatically with calibrated orifice meters. Computer-actuated solenoid valves allowed multiple pressure readings with one electonic pressure transducer.

The data acquisition system is essentially the same as that used for the high-temperature heat transfer tests.

Exhaust is sampled through a 1/4 inch stainless steel heat-traced tube located in the top of the combustor freeboard. The gas flows through a particulate filter, an acid mist filter, then through a Perma-Pure dryer. The gas flows through a final filter before entering the vacuum pump. The gas is then directed to the gas analyzers via a flow-rate-controlled manifold. The gas stream to the NO_x meter passes through a catalytic converter to convert NO_2 to NO. Five gas analyzers were used: SO_2, NO_x, CO_2, CO, and O_2 meters. The oxygen meter is a Beckman paramagnetic type analyzer. The CO_2 and CO meters are Beckman infra-red analyzers. Horiba infra-red analyzers are used to measure NO_x and SO_2.

Solids sampling is performed using a 3 inch diameter cyclone on the exhaust stream. Collection efficiency can also be checked by performing isokinetic sampling on the exhaust tube. In shakedown combustion trials, it was found that the cyclone was catching greater than 90% of all particulates.

Load turndown tests were planned for three different fuel forms: coal-water limestone mixture, coal-limestone briquettes, and double screened crushed coal. In each test the maximum load turndown at constant combustion temperature was found. High combustion efficiency was also maintained for the load turndown tests.

VI. Results and Discussion

A. High-temperature heat transfer

Some of the data obtained in high temperature heat transfer tests is reported as local heat transfer coefficients, however, overall thermal conductances, UA, between the central bed and annular bed, are also presented as useful in understanding the operating characteristics of the dual bed geometry. The overall thermal conductance for the combustor was evaluated for a variety of operating conditions from the relationship:

$$UA = (Q_{jacket} + Q_{conv})/(T_C - T_H) \qquad (56)$$

where

Q_{jacket} = heat transfer into the water jacket
Q_{conv} = heat convected from the annular bed with the secondary air
T_C = combustor bed temperature
T_H = heat transfer bed temperature

The heat flows were determined from measurements of enthalpy changes in the water and secondary air flows. Overall thermal conductances, UA, were plotted as functions of secondary air flow for constant combustor firing rate. As a consequence of the constant firing rate, variations in UA can be attributed to changes in the annular bed operating conditions.

Figure 18 illustrates the variation in UA as function of secondary air flow for three choices of particle sizes in the heat transfer bed. There is little difference in heat transfer for the three particle sizes when the heat transfer bed is operated as a packed bed; the thermal conductivity of the packed beds is not a strong function of particle size (see Table 1). However, once the heat transfer bed is fluidized, considerable differences in heat transfer characteristics for the three particle sizes are observed. The smaller particles not only have lower fluidization velocities but they produced significantly higher heat transfer coefficients than do larger particles at comparable secondary air flows. It is apparent from Fig. 18 that the maximum variation in the heat transfer rate from the combustor due to variation in secondary air alone was about 3.5, although for some firing rates this variation was as large as 6.0. Variation of primary air flow in the combustion bed has been observed to produce at least a factor of 2 variation in the heat transfer rate. In combination, adjustments of primary air and secondary air can be expected to produce maximum load turndowns of between 7 and 12.

When the bed is defluidized, the heat transfer cross the bed is dependent on the thermal conductivity of the granulated material. Our original intent was to test material of similar density and heat capacity but of widely varying thermal conductivities. The properties of material tested in this task are listed in Table 2. Our measurements found only minor differences in the thermal conductivity of granulated materials regardless of the thermal conductivity of individual granules. This observation is in accordance with theoretical predictions of Krupiczka (1967). Nevertheless, experiments were performed with river sand, pure quartz, and silicon carbide to evaluate the effect of different bed materials on load turndown.

Figure 19 illustrates of the effect of thermal conductivity of the granulated bed material on the heat transfer rate from the combustor. The maximum and minimum heat transfer rates appear roughly comparable for the three materials although rates between these limits are distinct for the different materials. These differences are apparently the result of differences in minimum fluidization velocity for the three materials. For example, the silicon carbide, having the highest density of the three materials, has the highest minimum fluidization velocity. Accordingly, it does not show the characteristic rapid rise in heat transfer rate until well after this behavior is observed in other materials.

The effect of annular bed width on load turndown performance is very important to the design of the proposed turndown concept. Three bed inserts were tested that gave annular bed widths of 2.5 cm, 3.8 cm, and 6.35 cm. Experiments were designed to yield overall thermal conductance, UA, for the combustor geometry vs. superficial air velocity in the annular bed for the three annular bed widths. Sand with an average particle diameter of 1 mm was used in both the annular and central (combustion) beds. The results are illustrated in Fig. 20. Our general expectation had been that load turndown (i.e., ratio of maximum UA to minimum UA)would increase as bed width was made larger. Such a trend was observed in the data. However, this expectation was based on the assumption that minimum UA, due to heat conduction across a packed bed, would decrease with bed width while maximum UA, due to particle convection in a fluidized bed, would not be strongly influenced by bed width. The curves for the 2.5 cm and 3.8 cm. bed widths demonstrates these effects. However, the widest annular bed (6.35 cm) showed a maximum UA that was considerably higher than for the two smaller diameter beds. The effect of uncertainties in temperature and gas flow measurements on uncertainty in UA cannot account for the large differences. Because bubbles can become larger and faster as bed width is increased, there is some expectation for higher heat transfer coefficients in these circumstances; however, it seems unlikely that the effect would be as large as suggested by data for the 6.3 cm bed width. Careful examination of the data in this instance revealed that energy balances could not be obtained for the two data points that yielded high UA values. Energy balances for these two points showed discrepancies of 50 to 100%. Other points yielded energy balances to within 5 to 10%. This suggests that air was leaking between the two plenums that supplied air to the fluidized beds.

The high temperature heat transfer measurements were designed to give local heat transfer coefficients in the annular fluidized bed. This knowledge is very important in supporting future design calculations for combustors based on the two-bed load turndown concept.

Determination of heat transfer coefficients between fluidized beds and enclosing walls has been neglected in the last several years in favor of measurements for immersed horizontal tubes. Our goal was to remove this deficiency by making local heat transfer measurements within the combustor at combustion conditions. Extensive analysis of this data has led us to conclude that the results are not sufficiently accurate for our purposes.

We briefly summarize the difficulties that limited the accuracy of the local heat transfer measurements. Local convection coefficients in the

annular beds were measured to be as much as 100% higher than expected from mechanistic models based on two-phase fluidization concepts. We have determined that there were three sources of error in our high-temperature measurements of convection coefficients:

1. Radiation. It is well known that radiation can increase the apparent convection coefficient in fluidized beds by as much as 20-40% (Botterhill , 1986). The computational model was designed to treat radiation and convection separately, hence separate terms are highly desirable. Radiation can be corrected for but the correction is difficult to implement, especially if emissivities of surfaces change with time due to combustion or erosion.

2. Local measurement of convection coefficients required us to determine the heat flux across the stainless steel wall separating the central and annular beds. Great care was taken in obtaining temperature-dependent conductivities and position-dependent conductivities of this wall. Nevertheless, problems in accurately measuring the temperature gradient across the walls introduced significant uncertainty in values for convection coefficients. The high temperature at which our measurements were performed essentially set the limit on the accuracy of our results. We needed to measure temperature gradients of 5-40°F in environments at temperatures of 1000-1400°F; under the best circumstances it was only possible to read temperatures to one part in one hundred. We attempted to overcome this basic limitation by wiring thermocouples attached to either side of a wall in series to get a direct evaluation of temperature difference. Although the concept appeared to be sound, the resulting copper-steel and constantan-steel couples had intrinsically poor sensitivity.

3. We begin to suspect that thermocouple wires attached to the walls served as fins that conducted heat to the wall at the point of thermocouple attachment. The result was an overestimate of heat flux through the wall and, consequently, an overestimate of the convection coefficient. Although we were careful to electrically and thermally insulate the thermocouple leads in ceramic tubes, it was necessary to leave bare wire near the point of wall attachment to prevent interference of flow patterns near the wall. To test this fin effect, a three-dimensional heat transfer model of thermocouple leads attached to a flat surface was developed. This model calculated wall temperatures in the vicinity of wire attachment to walls as a function of actual convection coefficients. From these temperatures, apparent convection coefficients were determined in the same manner as was done in the experiments. The resulting overestimate in convection coefficients (percent error) is plotted against actual convection coefficient in Fig. 21; overestimates of 10-40% are to be expected with the error becoming larger as the convection coefficients become smaller.

These limitations on the accuracy of high temperature heat transfer measurements coupled with measurements of what appeared to be unrealistically high heat transfer coefficients in the annular bed suggested to us the need for the cold-flow measurements described in the next section.

B. Cold Flow Model

Two comparisons were made between the numerical and experimental data to validate the experimental method described previously for the cold-flow tests. The first comparison, shown in Fig. 22, plots power as a function of wire temperature obtained from experiments with data from corresponding computer simulations. Comparisons were made for three convection coefficients, h_{app}, which were obtained from experimental data by the correction procedure described previously. In all cases bed material was 520 μm sand in a fluidized bed of aspect ratio 17. The numerical model predicted wire temperatures within 7% of the measured values regardless of power setting. This good agreement suggests that we have accounted for all energy losses from the heated wall.

Secondly, we compared bed temperature determined from linear regression analysis of experimental wire temperature data with bed temperatures measured directly with a thermometer. These comparisons, performed in a fluidized bed of aspect ratio 16.5 containing 1000 μm diameter sand particles, are found in Table 4. Superficial velocities through the bed ranged between 0.4 m/s and 0.8 m/s. The regression analysis values agree with thermometer measurements within 0.9 C and 1.5 C for the tope and bottom bands on resistance wire, respectively.

The convection coefficients obtained in our experiments are compared to data of other researchers. Table 5 lists maximum convection coefficients for 1000 μm sand as determined in three different investigations. The value from Brown and Foley (1988), which correlates well with the value from this study, is from an annular fluidized bed with an aspect ratio of 7.0. The value from Bearg et al. (1950) was obtained from a correlation derived from data taken in a circular bed of 1.8 aspect ratio. We have found that most correlations derived from data taken in beds of conventional geometry predict lower convection coefficients than found in this study.

Vreedenberg (1952) found that heat transfer rates to vertical tubes in a circular bed increased as the tubes were moved from the center of the bed toward the wall. The lower heat transfer rates at the center of the bed were attributed to higher voidage arising from bubble migration toward the center of the bed. This result is in agreement with accepted hydrodynamic behavior of fluidized beds (Baeyens and Geldart, 1986). However, Vreedenberg (1952) found that heat transfer rates decreased near the containing walls. This was attributed to the lack of particle mixing at the walls. In high aspect ratio beds slugging is predominant. We have observed that slugging enhances particle mixing at the walls of the bed. This may explain the higher bed-to-wall convection coefficients found in our study.

We examined the effect of particle diameter on bed-to-wall heat transfer coefficients in high aspect beds. Figures 23, 24 and 25 show convection coefficients for sands of three different average diameters in beds with aspect ratios of approximately 17. The convection coefficients are plotted versus the ratio of superficial velocity, U, to the superficial velocity at minimum fluidization U_{mf}. These curves show qualitative features of conventional fluidized beds Kunii and Levenspiel, 1969); however, the magnitude of the convection coefficients found in this study is greater

than that found in beds of conventional geometry having similar particle and flow conditions.

Much effort was spent in developing the experimental technique used in the cold-flow tests. The large experimental uncertainties present in the high-temperture tests were absent in the cold flow tests. Nevertheless, both experiments yielded convection coefficients significantly higher than those obtained by other researchers for conventional fluidized bed geometries. We conclude that the unique hydrodynamics of high aspect ratio beds are responsible for these differences. This conclusion is further supported by results of combustion tests described below.

C. Combustion Tests

Load turndown tests have been performed for the three fuel forms: crushed coal, coal-limestone briquettes, and coal-water-limestone mixture (CWLM). Test data for the crushed coal is shown in Table 6. A load turndown of 12.4 at constant combustion temperature (1155 ± 25 K) was achieved. The temperature was held constant by admitting the proper amount of air through the heat transfer bed after the combustion fuel flow and air flow rates are set.

The combustor is designed for air-staged firing. The combustion bed is operated sub-stoichiometrically to suppress NO formation. Overfire is injected above the bed to complete fuel combustion at slightly lean conditions. This overfire air consists of air exiting the heat transfer bed (secondary air) as well as air bypassing the heat transfer bed (tertiary air). The target value of excess air was 20% with a combustion bed equivalence ratio of 1.30. It was not possible to hold the excess air level at 20% for the lowest firing rates to avoid defluidization of the combustion bed. The excess air level ranged from 5 to 50% for the five highest flow rates. This wide range was the result of our inability to accurately meter coal with the auger feeder. In future tests, we decided to use air flow rates instead of fuel flow rates to set excess air level.

No limestone was added to the bed for these trials with dry coal. The sulfur emissions of 1480 ppm to 2385 ppm are in the range expected for the coal. Sulfur balances (which accounted for intrinsic calcium in the coal) agree within a few percent. Emissions of NO_x ranged from 0.10 to 0.27 kg/GJ. All tests met or exceeded New Source Performance Standards of 0.20 to 0.34 kg/GJ.

Load turndown ratio is best defined as the ratio of the maximum to minimum firing rates for a combustor. In developing Eq. 5 and simulating heat transfer in the combustor, it was necessary to employ an alternative, but nearly equivalent definition of load turndown; that is, load turndown was defined as the maximum to minimum heat transfer rate between the combustion bed and the water jacket. We also define the overall heat transfer coefficient, UA, as the total heat transfer rate to the water jacket divided by the temperature gradient between the combustion bed and water jacket. Fig. 26 is a plot of overall heat transfer coefficients measured as a function of annular bed air flow rate for the crushed coal tests. The ratio of maximum to minimum overall convection coefficients represents this alternative definition of load turndown ratio. The value of 9.0 obtained

from Fig. 26 is in excellent agreement with calculations using Eq. 4 and predictions of the computer model (see Fig. 4). Discrepancy between values obtained with the two definitions of load turndown result from neglect in Eq. 4 of heat convected out of the combustor in the air flow through the annular bed.

Load turndown test results for briquettes are shown in Table 7. A load turndown of 9.4 was achieved at constant combustion temperature (1110 K ± 35K). A test to determine conventional load turndown is shown as entry Run B6. Conventional load turndown is defined as the ratio of maximum to minimum firing rate with the annular bed defluidized, regardless of firing rate, and combustion temperature and air-to-fuel ratio held constant. The conventional load turndown in these tests was 5.3.

Test results for CWLM are shown in Table 8. A load turndown of 9.0 was achieved at constant combustion temperature (1110 K ± 45K). Again, the temperature was maintained at the desired level by adjusting secondary air flow through the annular bed for each firing rate.

Although a load turndown of 12.4 was achieved for crushed coal, turndown was limited to 9.0 for briquettes and CWLM. One possible explanation for this is evident by reexamining the minimum fuel flow rates in Tables 6, 7, and 8. For the crushed coal case, 100% of the fuel burned at this lowest firing rate is burned in the bed, while for briquettes and CWLM only 74% and 53% respectively is burned in the bed. A greater percentage of fuel burned in the bed allows lower fuel firing rates to maintain the same combustion temperature. Lower minimum firing rates and correspondingly larger turndowns would probably have resulted in CWLM and briquettes if we had allowed leaner stoichiometries for these fuel forms.

Combustion temperature was held constant at 1121 ± 57 K in all load turndown tests. Fig. 27 shows a plot of combustion bed temperature vs. coal feed rate (fuel flow rate minus limestone and water flow rates). The bed temperatures are well within the 1000-1200 K range for efficient and clean combustion. The bed temperature is easily held constant by adjusting the secondary air-flow rate through the heat transfer bed.

Both the briquettes and the CWLM were formulated with a calcium-to-sulfur molar ratio of 2.0. Sulfur dioxide emission reductions of 42% to 93% were observed in the load turndown tests. The effect of combustion temperature on sulfur retention is shown in Fig. 28.

Our data for CWLM and briquettes burned in sand beds is compared to experimental results of Mesko (1980) who burned low-sulfur peat in a limestone bed. Mesko found the optimal bed temperature for sulfur retention to be close to 1100 K, which is representative of results obtained by other researchers who employed limestone beds. In contrast, we found the optimum bed temperature to be no higher than 1050 K. This discrepancy with results of other researchers probably arises from the fact that limestone in briquettes and CWLM will more closely follow the temperature history of fuel particles, in which they are incorporated, than the bulk bed material. Since fuel particles burn at temperatures 50 to 200 K higher than the bed (Basu, 1977), the optimal bed temperature for sulfur retention is expected to be somewhat lower for fuel forms that contain limestone. Furthermore,

we found higher sulfur retention in our trials than did Mesko (1980). This result, as well, is probably related to the intimate contact of limestone with coal briquettes and CWLM.

The effect of combustion bed temperature on emissions of NO_x is illustrated in Fig. 29. The general trend is for increased emissions of NO_x as temperature is increased, as expected. However, NO formation is also strongly dependent on combustion bed stoichiometry. For low NO emissions, therefore, the bed should be operated sub-stoichiometrically with low combustion temperatures. Emissions of NO ranged from 0.08 to 0.27 kg/GJ. All tests met or exceeded EPA New Source Performance Standards of 0.20 to 0.34 kg/GJ.

Experimental results obtained for briquettes have been compared to simulation predictions. Fig. 30 plots firing rate in the combustion bed vs. secondary air flow rate through the annular bed for a constant combustion temperature. Model predictions and experimental results show two major discrepancies. First, the model predicts a sudden increase in firing rate when secondary air flow is increased to a level high enough to fluidize the annular bed. In contrast, the experimental results show a more gradual increase in firing rate with increasing secondary air flow. Second, the model underpredicts the amount of heat that can be removed from the combustor at the highest secondary air flow rates. Both of these discrepancies arise from the convection coefficients calculated for the annular bed from the two-phase theory of fluidization. These results are consistent with the cold-flow test results. Not only were maximum coefficients higher than predicted by two-phase theory of fluidization but convection coefficients increased more gradually with increasing superficial velocity than is expected from theory.

VII. Conclusions

A load turndown of 12.3 was achieved while burning crushed coal, exceeding the project goal of 10.0. Slightly lower load turndowns of around 9 were obtained for coal water limestone mixtures and coal-limestone briquettes. This was attributed to slightly different operating conditions during the combustion tests. Sulfur reductions of 43% to 92% were observed while burning coal-water-limestone mixtures and briquettes for a calcium-to-sulfur molar ratio of 2.0. Staged firing resulted in low emissions of NO_x. Emissions of both NO_x and SO_2 met or exceeded EPA New Source Performance Standards.

Results of the heat transfer tests showed that heat transfer coefficients in high aspect ratio fluidized beds are generally higher than predicted by theory or correlations developed for fluidized beds of conventional geometry. Computer model prediction of heat transfer in the combustor were in reasonable agreement with experimental observations.

REFERENCES

Anson, D., 1976, "Prog. Energy Combustion Sci. Vol. 2, p. 61.

Baerg, A., Klassen, J., and Gishler, P. E., 1950, "Heat Transfer in a Fluidized Solids Bed," Canadian Journal of Research, 28, No. 8, pp. 287-307.

Baeyens, J., and Geldart, D., 1986, Gas Fluidization Technology, Geldart, D. ed., Wiley, New York, pp. 97-122.

Basu, P., 1977, "Burning Rate of Carbon in Fluidised Beds," Fuel, Vol. 56, pp. 390-392.

Brown, R. C. and W. Buttermore, 1988, "A Method for Improving Load Turndown in Fluidized Bed Combustors," Patent No. 4,762,090.

Brown, R. C. and J. E. Foley, 1988, "A Method for Improving Load Turndown in Fluidized Bed Combustors," Industrial and Engineering Chemistry Research, Vol. 27, pp. 24-30.

Brown, R. C., and Jasper, S. S., 1989, "Immersion Cooling of Electronics In Fluidized Beds of Dielectric Particles," to appear in Heat Transfer Engineering.

Gibbs, B. M., F. J. Pereira, and J. M. Beer, 1977, Sixteenth Symposium (International) on Combustion, The Combustion Institute, pp. 461-474.

Horio, M., Hayashi, H., and Morishita, K., 1985, Proc. of the Eighth Int. Conf. on Fluidized Bed Combustion, Houston, Texas.

Kunii, D. and O. Levenspiel, 1969, Fluidization Engineering, John Wiley & Sons, Inc., New York, pp. 90-91.

Leva, M., Weintraub, M., and Grummer, J., 1949, "Heat Transmission Through Fluidized Beds of Fine Particles,: Chemical Engineering Progress, 45, No. 9, pp. 563-572.

Mesko, J. E., 1980, "Combustion of Low Quality Fuels in Fluidized Bed Steam Generators," Natural Resources Forum, Vol. 4, pp. 265-275.

Mickley, H. S. and Fairbanks, D. F., 1955, "Mechanism of Heat Transfer to Fluidized Beds," AIChE J. Vol. 1, p. 374.

Pflum, D. L., Brown, R. C., and Maxwell, G. M., 1989, "A Resistance Wire Technique Applied to Heat Transfer in High Aspect Ratio Fluidized Beds," 26th National Heat Transfer Conference, Philadelphia, PA.

Roberts, A. G., Stanton, J. E., Wilkins, D. M., Beacham, B., and Hoy, H. R., 1975, Inst. Fuel Symp. Ser., No. 1.

Romani, M. N. and Richardson, J. F., 1974, "Heat Transfer From Immersed Surfaces to Liquid-Fluidized Beds," Lett. Heat Mass Transfer, 1, pp. 55-61.

Vreedenberg, H. A., 1952, "Heat Transfer Between Fluidized Beds and Vertically Inserted Tubes," Journal of Applied Chemistry, 2, Supplementary Issue No. 1, pp. 526-533.

Xavier, A. M. and Davidson, J. F., 1985, "Heat Transfer in Fluidized Beds: Convective Heat Transfer in Fluidized Beds," in Fluidization, 2nd edition, John Wiley & Sons, New York, pp. 437-464.

IX. Nomenclature

A = heat transfer area, m^2

A_{ann} = annular bed cross-sectional area, m^2

A_c = combustion bed cross-sectional area, m^2

A_o = orifice plate area per orifice, m^2

A_r = Archimedes number

B_c = constant in boiling flux equation

C_g = gas specific heat, J/kgK

C_{mg} = fluidized bed specific heat at minimum fluidization, J/kgK

C_{pa} = specific heat of air, J/kgK

C_{pl} = specific heat of water, J/kgK

C_{pw} = specific heat of water, J/kgK

C_s = solid particle specific heat, J/kgK

C_{sf} = surface-combination constant

D = column diameter, m

D_a = annular bed diameter, m

D_C = combustion bed diameter, m

d_b = bubble diameter, m

d_p = particle average diameter, m

g = acceleration due to gravity, m/s^2

H_f = fluidized bed height, m

H_j = water jacket height, m

H_{mf} = fluidized bed height at minimum fluidization, m

H_{min} = defluidized bed height, m

h_a = annular bed convection coefficient, W/m^2K

h_{act} = actual bed-to-wall convection coefficient, W/m^2K

h_{app} = apparent bed-to-wall convection coefficient, W/m^2K

h_{av} = inverse of fluidized bed resistance, W/m^2K

h_b = combustion bed convection coefficient, W/m^2K

h_c = central bed convection coefficient, W/m^2K

h_f = inverse of film resistance, W/m^2K

h_{fg} = latent heat of evaporization, kJ/kg

h_{gc} = gas convection coefficient, W/m^2K

h_H = annular bed convection coefficient, W/m^2K

h_p = inverse of packet resistance, W/m^2K

h_{pc} = particle convection coefficient, W/m^2K

h_w = water convection coefficient, W/m^2K

k_o = defluidized bed conductivity, W/mK

k_e = defluidized bed conductivity, W/mK

k_g = gas thermal conductivity, W/mK

k_{mf} = minimally fluidized conductivity, W/mK

k_s = solid particle conductivity, W/mK

L = characteristic length, m

m = empirical constant

$\dot{m}_w$ = water mass flow rate, kg/s

Nu_{gc} = gas convection Nusselt number

P = power dissipated in resistance wire, W

Pr = Prandtl number

Pr_w = water Prandtl number

Q_{cair} = energy convected out of combustion bed, W

Q_{cond} = conduction heat transfer, W

Q_{conv} = convection heat transfer, W

Q_{crad} = energy radiated from combustion bed, W

Q_{cwall} = energy convection to wall from combustion bed, W

Q_{H2O} = heat transfer to water jacket, W.

Q_{HTAIR} = energy convected out of annular bed, W

Q_{IN} = energy released in combustion bed, W

q = heat transfer flux, W/m^2

q_b'' = boiling heat flux, W/m^2

q_{MAX} = maximum heat transfer from central bed, W/m^2

q_{MIN} = minimum heat transfer from central bed, W/m^2

R = wire resistance, ohms

R_o = reference wire resistance, ohms

Re_p = particle Reynolds number

T_b = combustion bed temperature, K

T_c = combustion bed temperature, K

T_g = gas temperature, K

T_{IW} = dividing wall temperature, K

T_o = inlet air temperature, K

T_p = Annular bed particle temperature, K

T_{SAT} = water saturation temperature, K

T_w = water temperature or wire temperature, K

T_{WALL} = wall temperature, K

T_∞ = fluidized bed temperature, K

U = superficial gas velocity, m/S

U_B = bubble velocity, m/S

UB_{IW} = radiation coefficient, W/m^2K

U_{go} = standard air inlet velocity, m/S

U_{mf} = minimum fluidizing velocity, m/S

U_o = air inlet velocity, m/S

U_{PIW} = radiation coefficient, W/m^2K

U_{POW} = radiation coefficient, W/m^2K

α = temperature coefficient of resistance, K^{-1}

ΔI = resolution of current measurements, amps

ΔT = maximum error in wire temperature, K

ΔV = resolution of voltage measurements, volts

ΔX = annular bed width, m

ε_B = bed emissivity

ε_{IW} = wall emissivity

ε_{mf} = bed voidage at minimum fluidization

ε_o = defluidized bed voidage

ε_{ow} = wall emissivity

ε_p = bed prticle emissivity

ρ_g = gas density, kg/m^3

ρ_l = water density, kg/m^3

ρ_{mf} = bed density at minimum fluidization, kg/m^3

ρ_o = air inlet density, kg/m^3

ρ_s = solid particle density, kg/m^3

ρ_v = saturated vapor density, kg/m^3

σ = Stefan Boltzmann constant, W/m^2K^4

σ_B = bubble surface tension, N/m

μ_g = gas viscosity, Ns/m^2

μ_l = water viscosity, Ns/m^2

Table 1. Granulated material used in Task 1.

Sample	Size Range	Thermal Conductivity (W/m-K)
Large	0.85 - 1.18 mm	$k = 0.234 + 4.24 \times 10^{-4}T$
Medium	425 - 600 μm	$k = 0.238 + 3.33 \times 10^{-4}T$
Small	212 - 300 μm	$k = 0.132 + 4.74 \times 10^{-4}T$

Table 2. Granulated material used in the Task 2.

Material	Density (kg/m3)	Cp (J/kg-K)	Thermal Conductivity (W/m-K)
Sand	2600	840	$k = 0.234 + 4.24 \times 10^{-4}T$
Quartz	2680	754	$k = 0.0634 + 6.07 \times 10^{-4}T$
Silicon Carbide	3145	837	$k = 0.205 + 4.26 \times 10^{-4}T$

Table 3. Analysis of Illinois No 5 Rapatee Coal

Property	As Received	Moisture Free	Moisture, Ash Free
Moisture	10.8	0.0	0.0
Ash	10.1	11.3	0.0
Volatile Matter	36.6	41.0	46.3
Fixed Carbon	42.5	47.7	53.7
Heating Value (BTU)	11,395	12,775	14,405
Free Swelling Index	4	--	--
Sulfate Sulfur	0.07	0.08	0.09
Pyritic Sulfur	0.96	1.08	0.12
Organic Sulfur	1.65	1.84	2.09
Total Sulfur	2.68	3.00	3.39
	Ultimate Analysis		
Carbon	69.47	77.88	87.83
Hydrogen	4.56	3.76	4.24
Nitrogen	1.33	1.49	1.68
Oxygen	11.86	2.57	2.90

(All values given in percent except BTU and Free Swelling Index)

Table 4. Comparison of calculated and measured bed temperatures.

Top Band of Resistance Wire			Bottom Band at Resistance Wire		
Tw_{cal}	Tw_{meas}	ΔT	Tw_{cal}	Tw_{meas}	ΔT
18.7	17.8	0.9	19.3	17.8	1.5
19.8	20.6	-0.8	20.7	20.6	0.1
21.6	21.1	0.5	21.7	21.1	0.6
21.2	21.1	0.1	21.9	21.1	0.8
19.8	20.6	-0.8	20.0	20.6	-0.6
21.8	21.1	0.7	22.6	21.1	1.5
21.3	21.1	0.2	22.2	21.1	1.1
21.7	21.1	0.6	22.2	21.1	1.1
20.0	20.6	-0.6	21.2	20.6	0.6
20.6	20.6	0.0	21.1	20.6	0.5
19.0	18.3	0.7	19.6	18.3	1.3
20.9	20.6	0.3	20.7	20.6	0.1

Table 5. Comparison of maximum convection coefficients for 1000 μ sand.

Study	Aspect Ratio	h_{max}
Our study	17	345
Brown & Foley	7	320
Baerg	2	273

Table 6. Turndown test results for crushed coal

Run	Feed Rate (kg/hr)	Bed Temperature (K)	Bed Equivalence Ratio	Overall Excess Air(%)	Total Air Flow* (kg/hr)	Secondary Air Flow (kg/hr)
1	0.74	1133	0.44	126	15.4	0.0
2	1.28	1172	0.71	67	19.5	0.0
3	1.87	1156	1.30	42	24.2	11.1
4	5.43	1144	1.52	5	52.4	11.3
5	7.19	1161	1.37	10	72.7	14.4
6	7.08	1172	1.05	50	97.1	19.1
7	9.21	1178	1.36	18	100.0	31.2

O_2 (%)	CO_2 (%)	CO (%)	SO_2 (ppm)	NO_x (ppm)	kg NO per GJ	Combustion Efficiency (%)	% Burned in bed
10.6	7.9	.051	--	300	.24	95	100
7.4	10.9	.029	--	325	.19	95	71
5.6	12.4	.034	1480	210	.10	94	71
1.3	16.9	.078	2385	435	.16	95	51
3.9	15.9	.070	1976	510	.20	96	50
6.3	12.1	.015	2000	520	.27	97	57
3.8	15.2	.037	2380	440	.18	95	52

*Sum of primary, secondary, and tertiary air.

Table 7. Turndown test results for briquettes

Run	Feed Rate (kg/hr)	Bed Temperature (K)	Bed Equivalence Ratio	Overall Excess Air(%)	Total Air Flow* (kg/hr)	Secondary Air Flow (kg/hr)
B1	1.08	1073	0.70	44	12.5	0.0
B5	3.46	1091	1.27	20	33.4	5.3
B4	4.85	1109	1.27	22	47.5	8.6
B3	5.77	1144	1.13	35	62.2	11.0
B2	10.10	1141	1.32	24	100.0	30.6
B6	5.69	1142	0.74	48	67.7	0.0

O_2 (%)	CO_2 (%)	CO (%)	SO_2 (ppm)	NO_x (ppm)	Sulfur Capture (%)	Combustion Efficiency (%)	% Burned in bed
5.9	12.2	.102	194	236	90	91	74
4.6	14.3	.008	368	271	84	90	57
4.2	14.3	.010	704	337	68	90	58
5.0	13.2	.024	1170	342	42	92	62
5.0	14.6	.024	936	313	57	95	51
7.2	11.8	.022	706	353	61	92	56

*Sum of primary, secondary, and tertiary air.

Table 8. Turndown test results for CWLM

Run	Feed Rate (kg/hr)	Bed Temperature (K)	Bed Equivalence Ratio	Overall Excess Air(%)	Total Air Flow* (kg/hr)	Secondary Air Flow (kg/hr)
C2	2.49	1064	0.76	31	16.8	0.0
C1	5.28	1106	1.32	14	30.8	4.1
C3	22.29	1152	1.43	8	123.2	30.8

O_2 (%)	CO_2 (%)	CO (%)	SO_2 (ppm)	NO_x (ppm)	Sulfur Capture (%)	Combustion Efficiency (%)	% Burned in bed
5.1	13.2	.190	151	272	93	91	53
2.3	15.5	.083	209	192	91	91	40
1.1	16.7	.200	815	263	68	94	38

*Sum of primary, secondary and tertiary air.

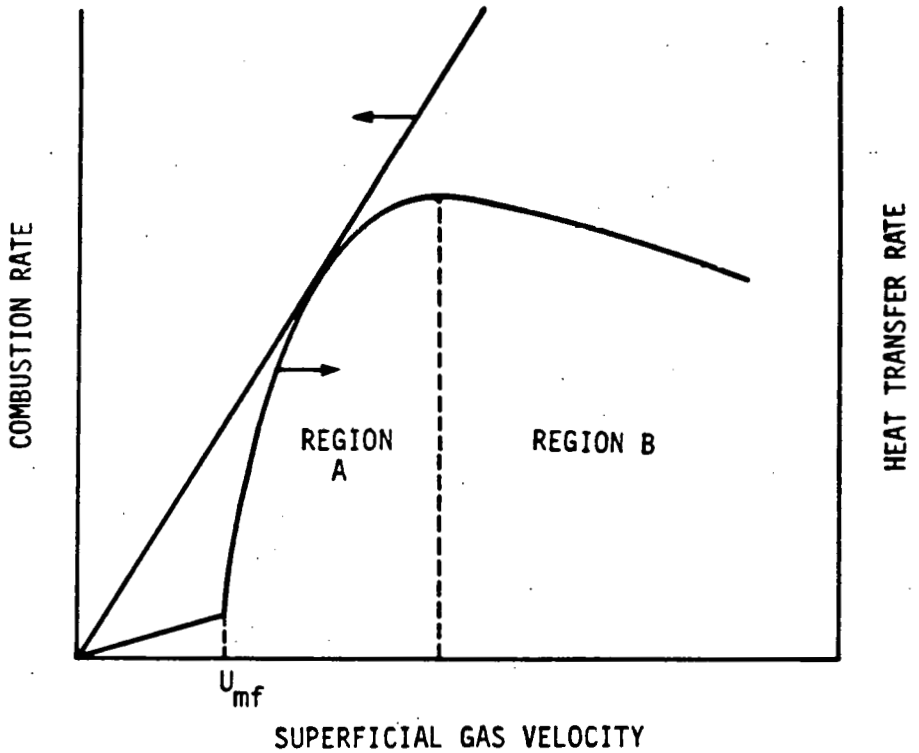

Fig. 1. Heat transfer and combustion rate vs. gas velocity.

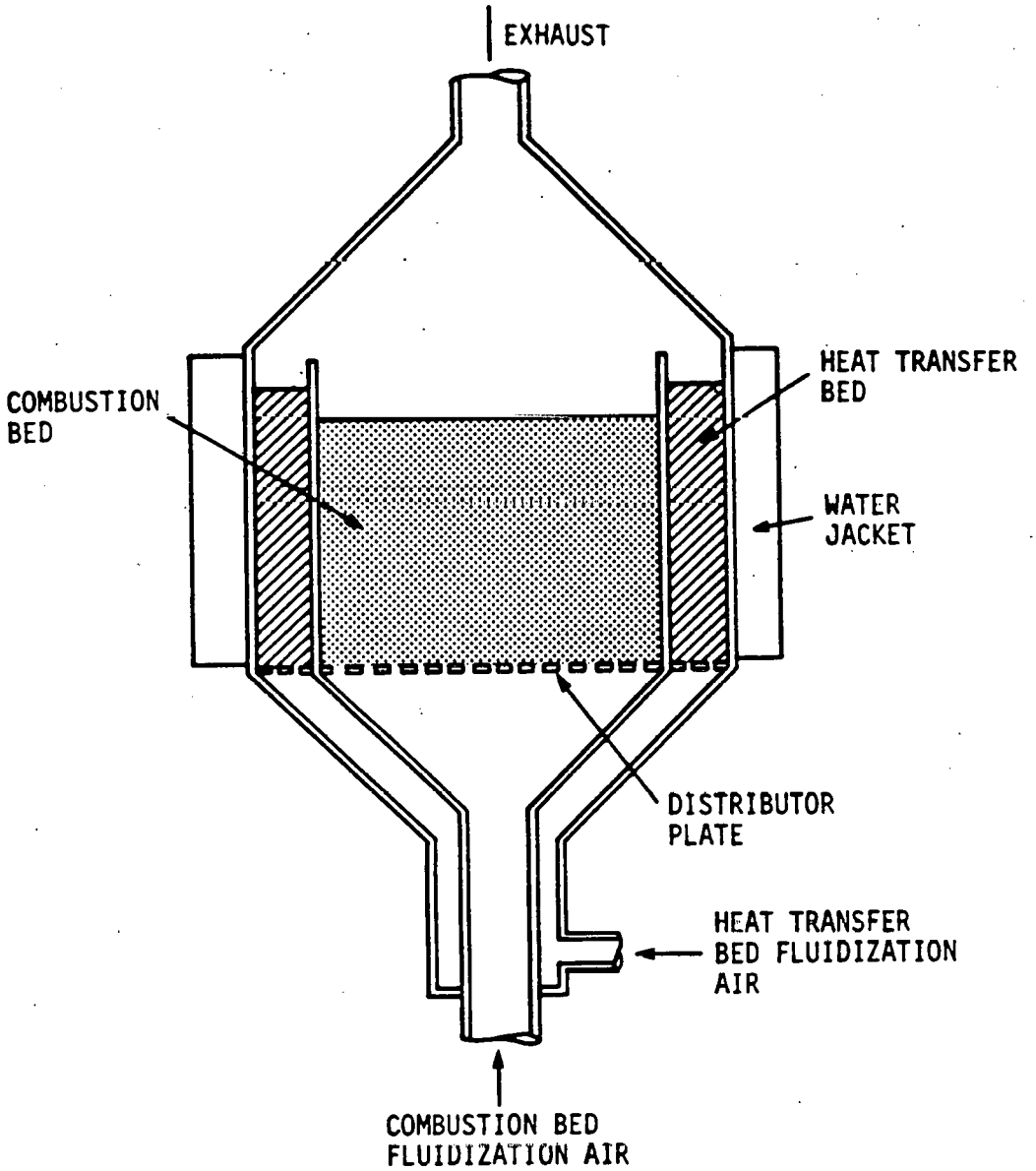

Fig. 2. Schematic of a two-bed combustor.

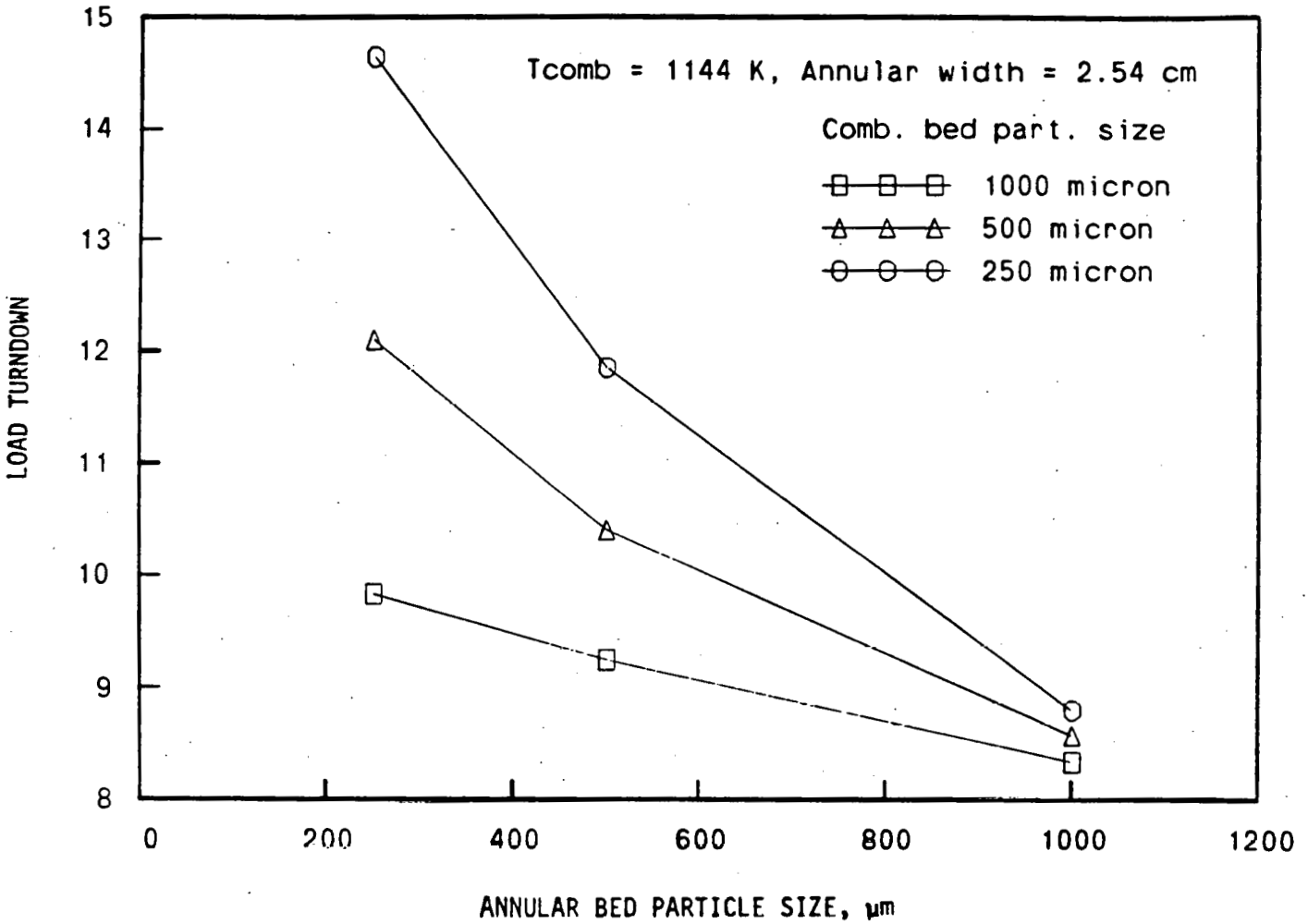

Fig. 3. Effect of particle sizes on load turndown.

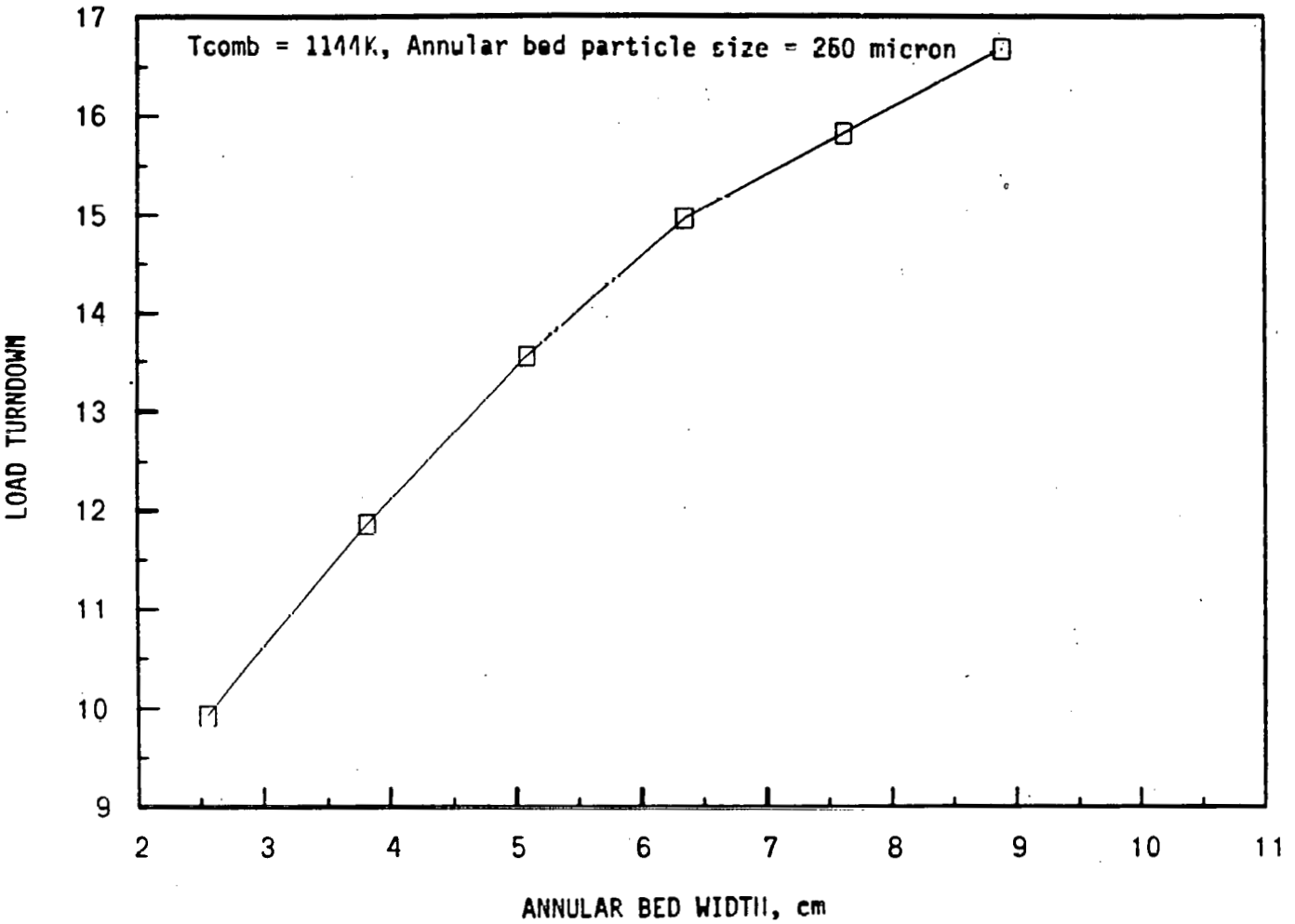

Fig. 4. Effect of annular bed width on load turndown.

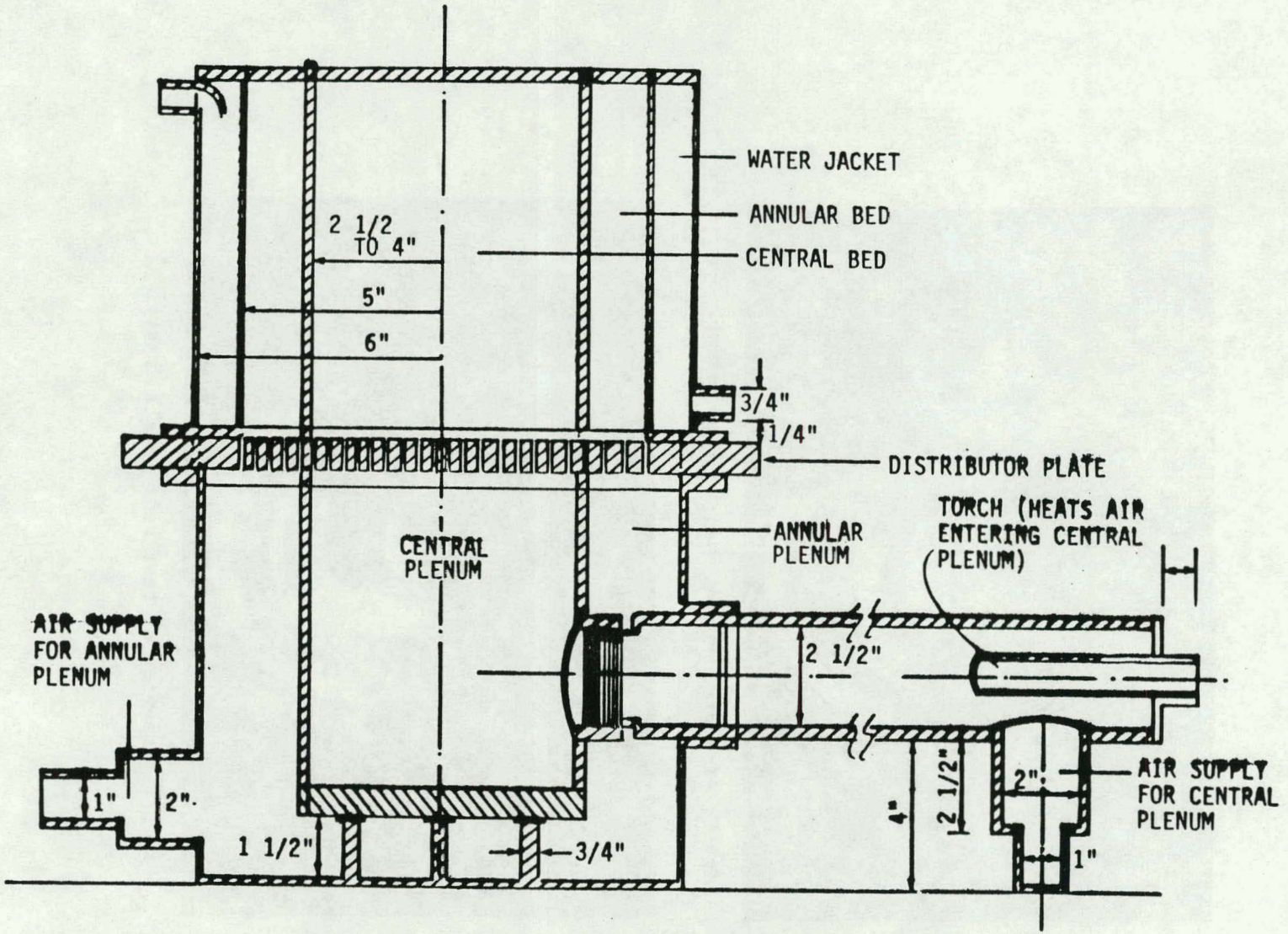

Fig. 5. Schematic of high temperature heat transfer model.

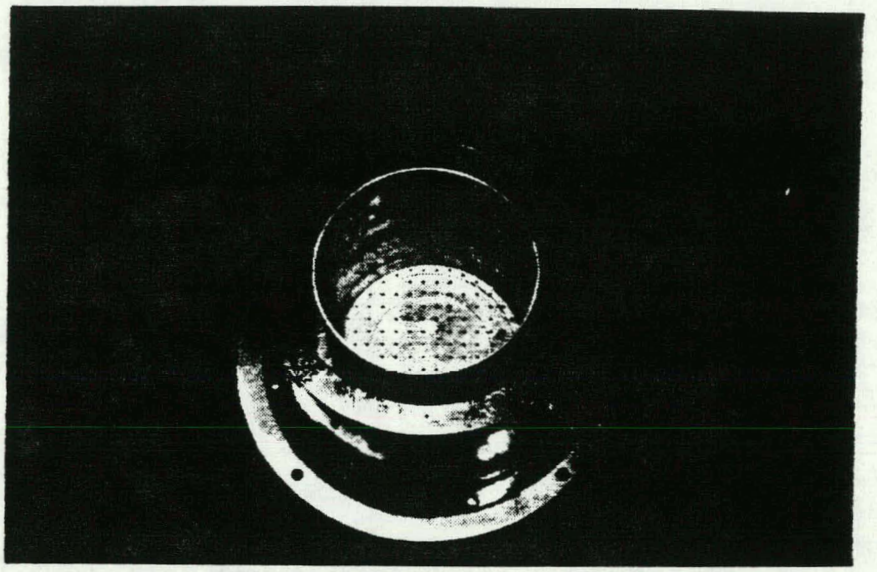

Fig. 6. Top view of test bed: Large Insert.

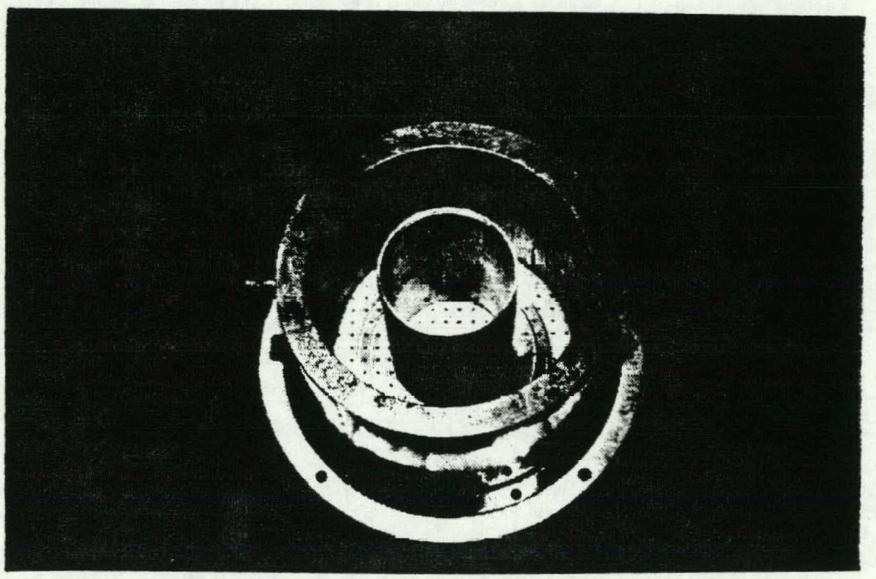

Fig. 7. Top view of test bed: Small Insert.

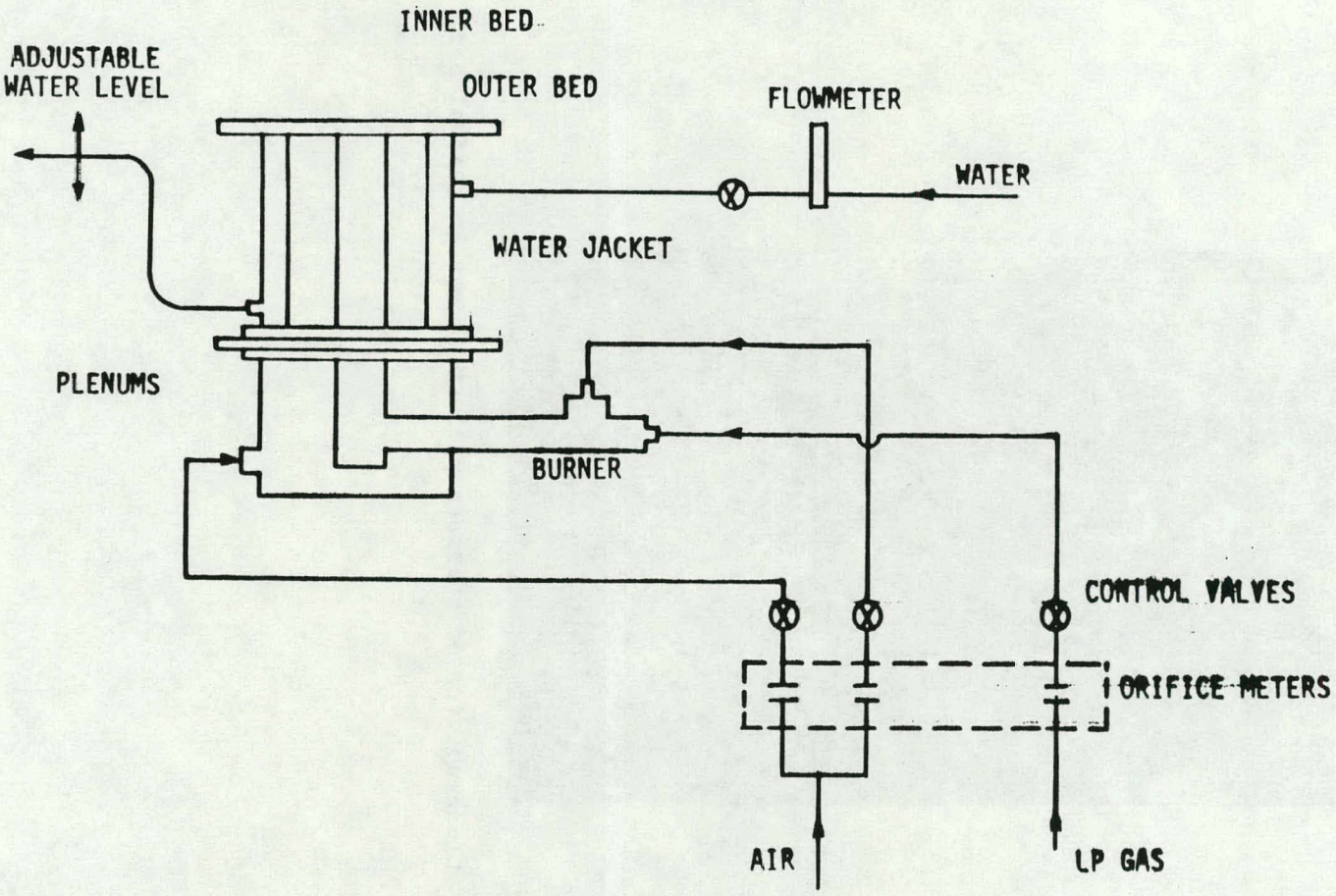

Fig. 8. Piping schematic for test bed.

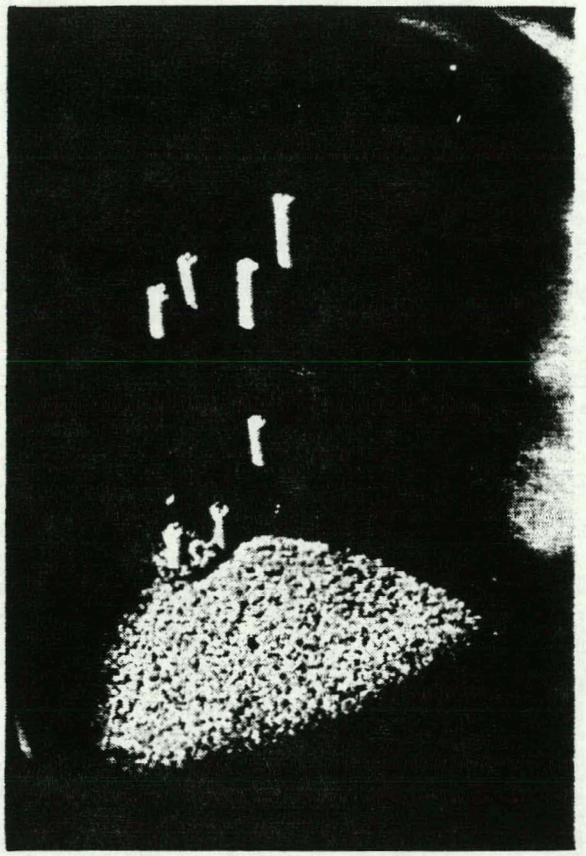

Fig. 9. Close-up view of thermocouple attachment in central bed.

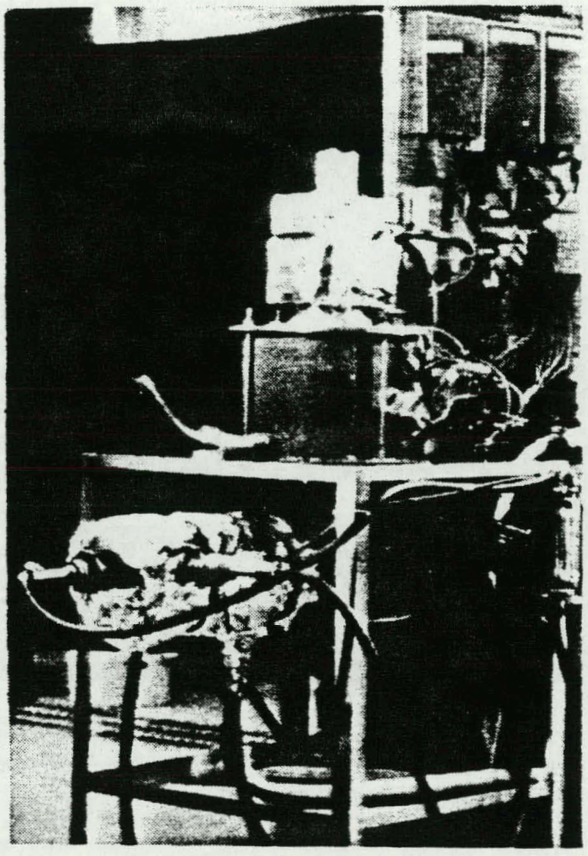

Fig. 10. Side view of test bed showing heat exchanger core and LP-gas burner.

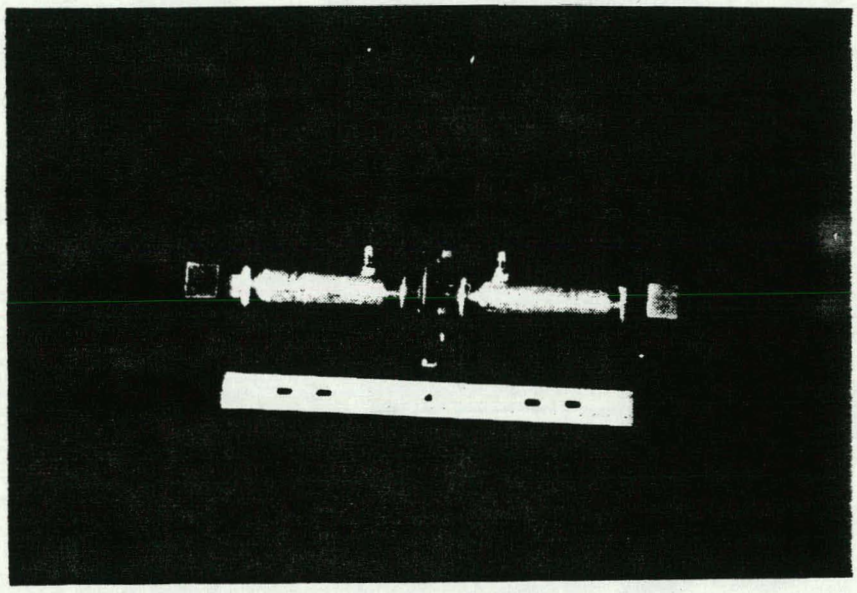

Fig. 11. Orifice plate flow meter assembly.

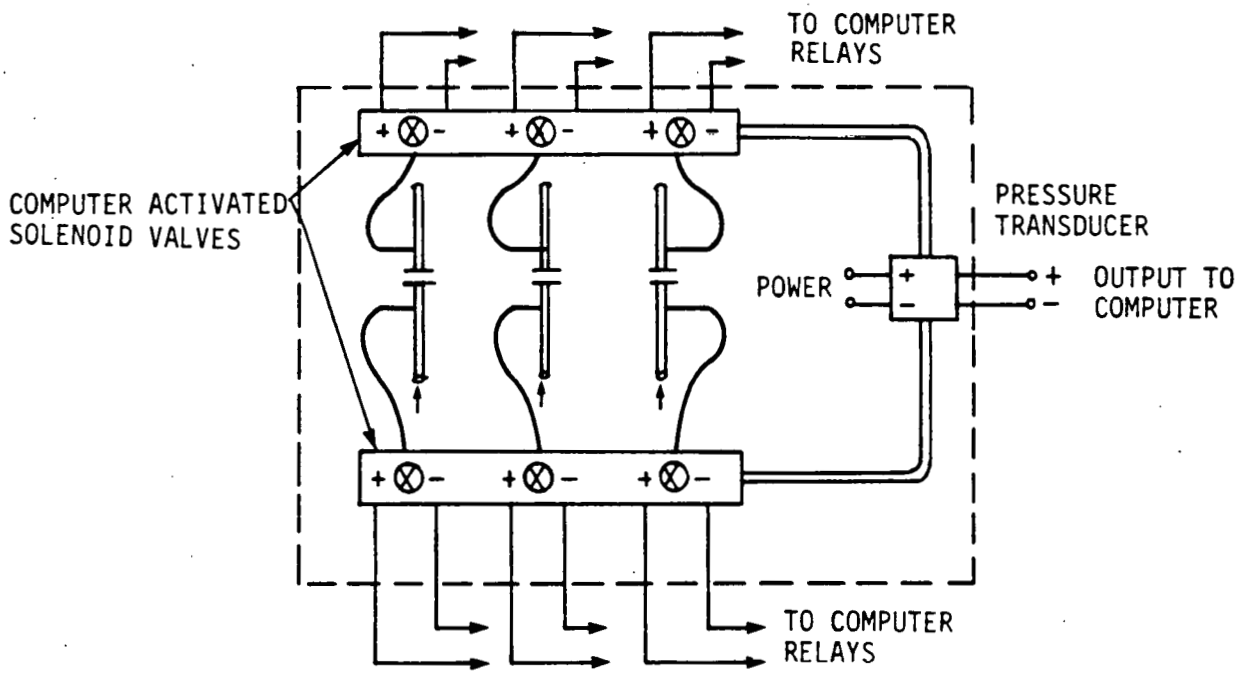

Fig. 12. Detail of flow metering system.

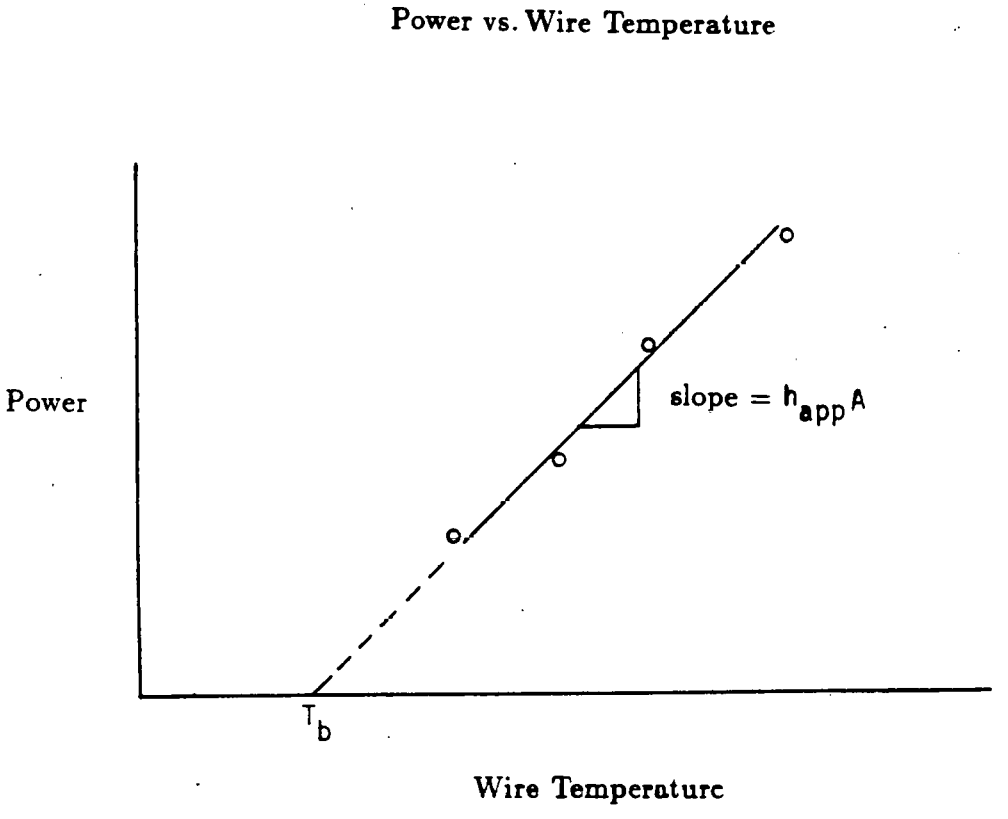

Fig. 13. Typical power vs. wire temperature curve

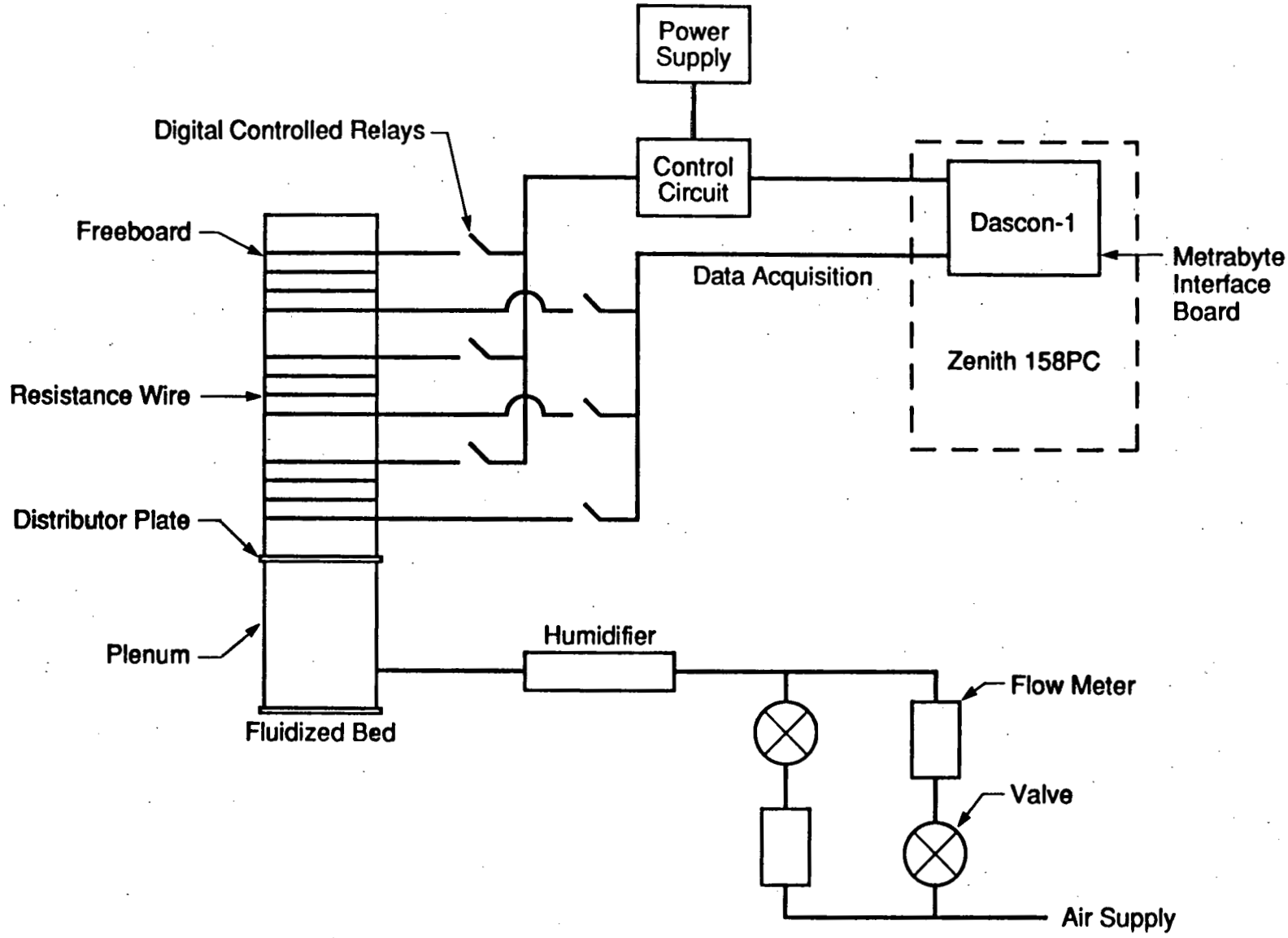

Fig. 14. Schematic of experimental apparatus.

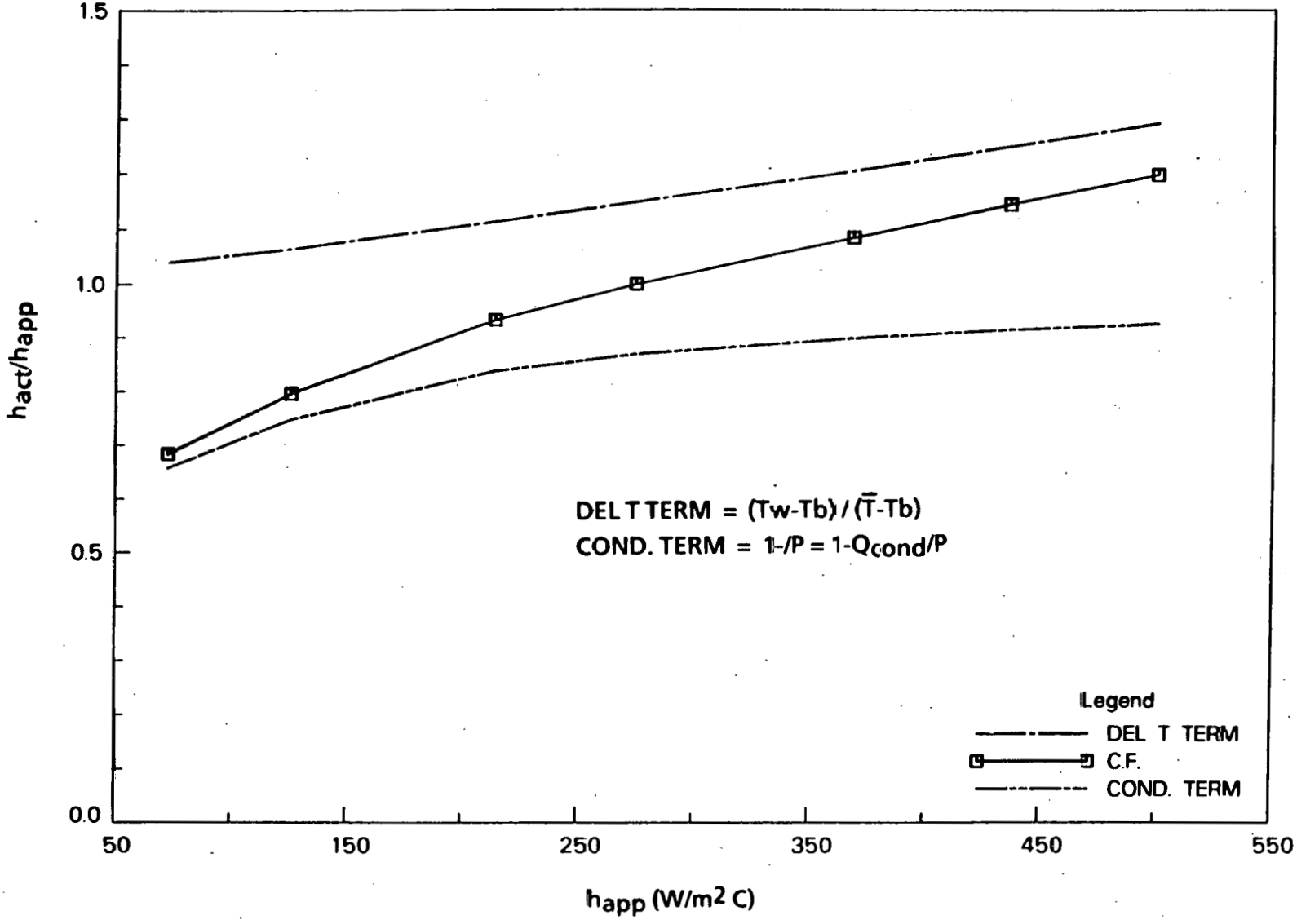

Fig. 15. Correction factor curve.

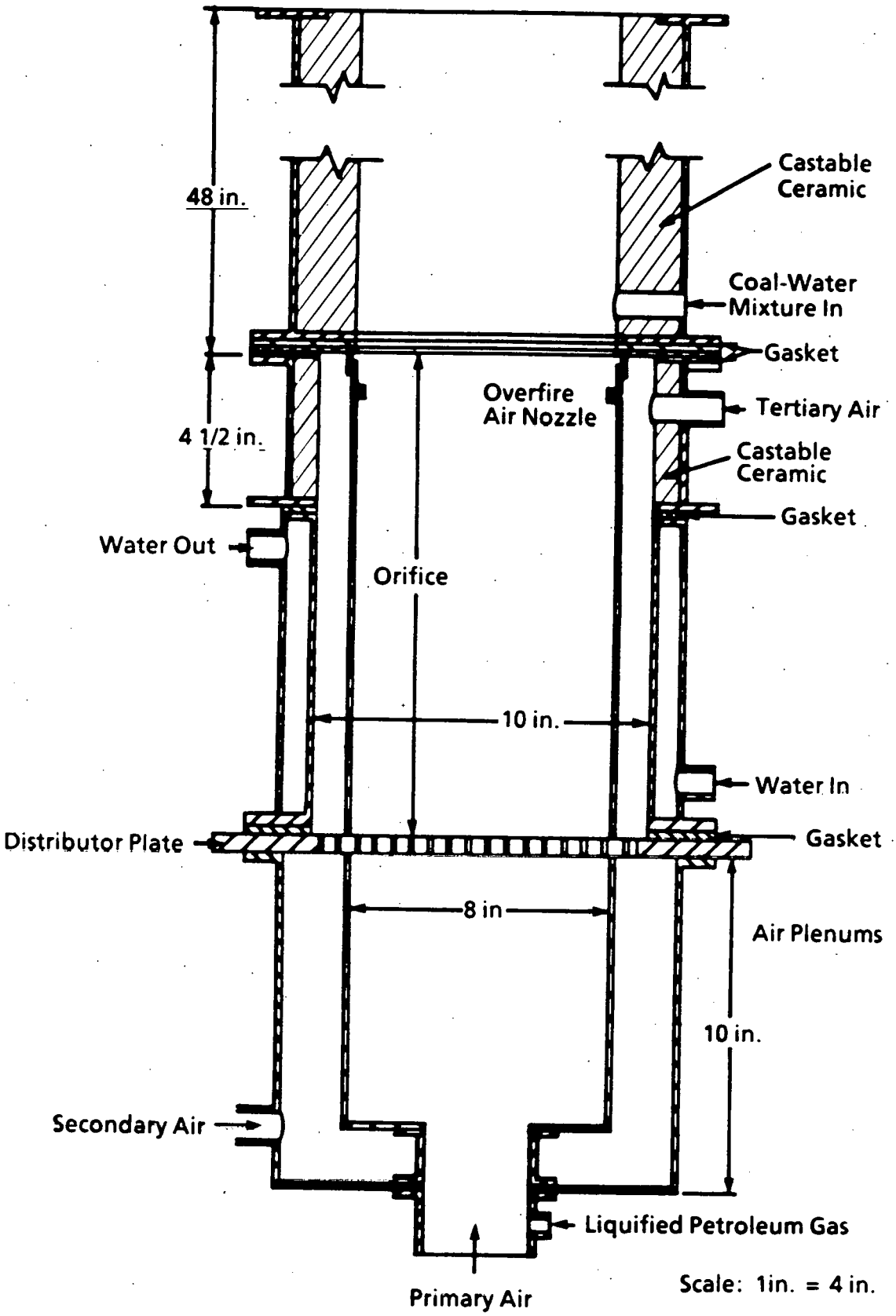

Fig. 16. Schematic of fluidized bed combustor.

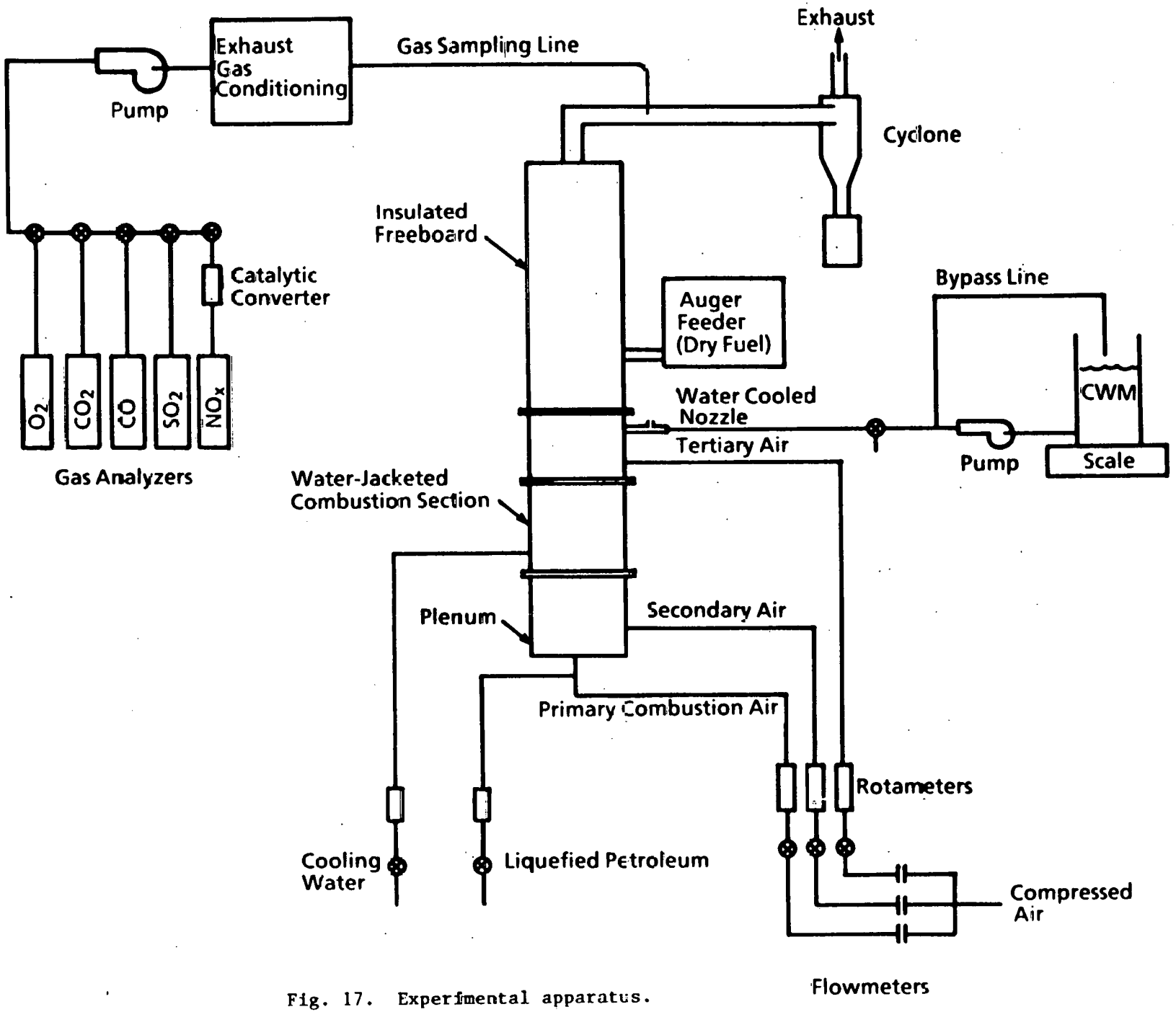

Fig. 17. Experimental apparatus.

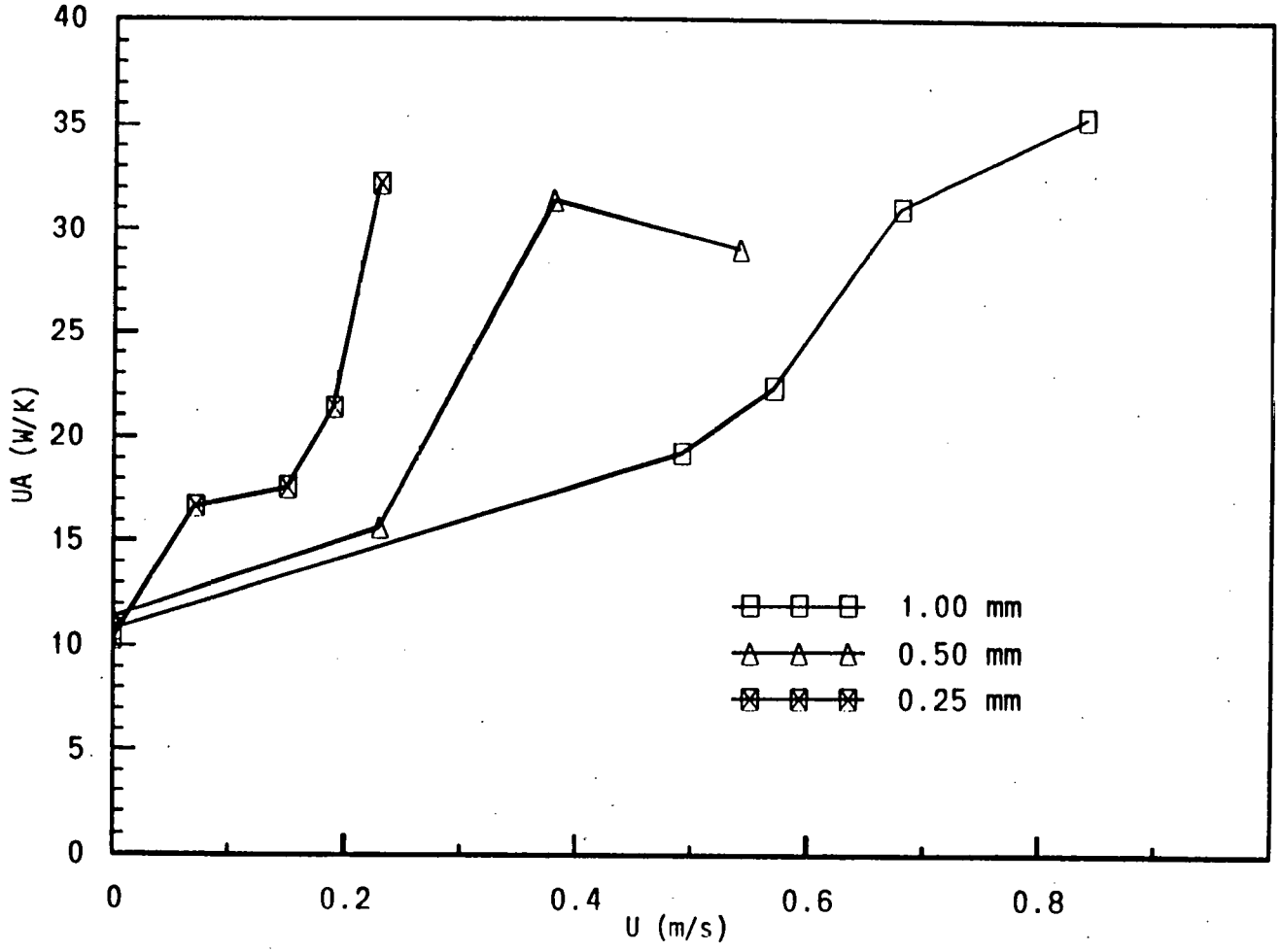

Fig. 18. Effect of bed particle size.

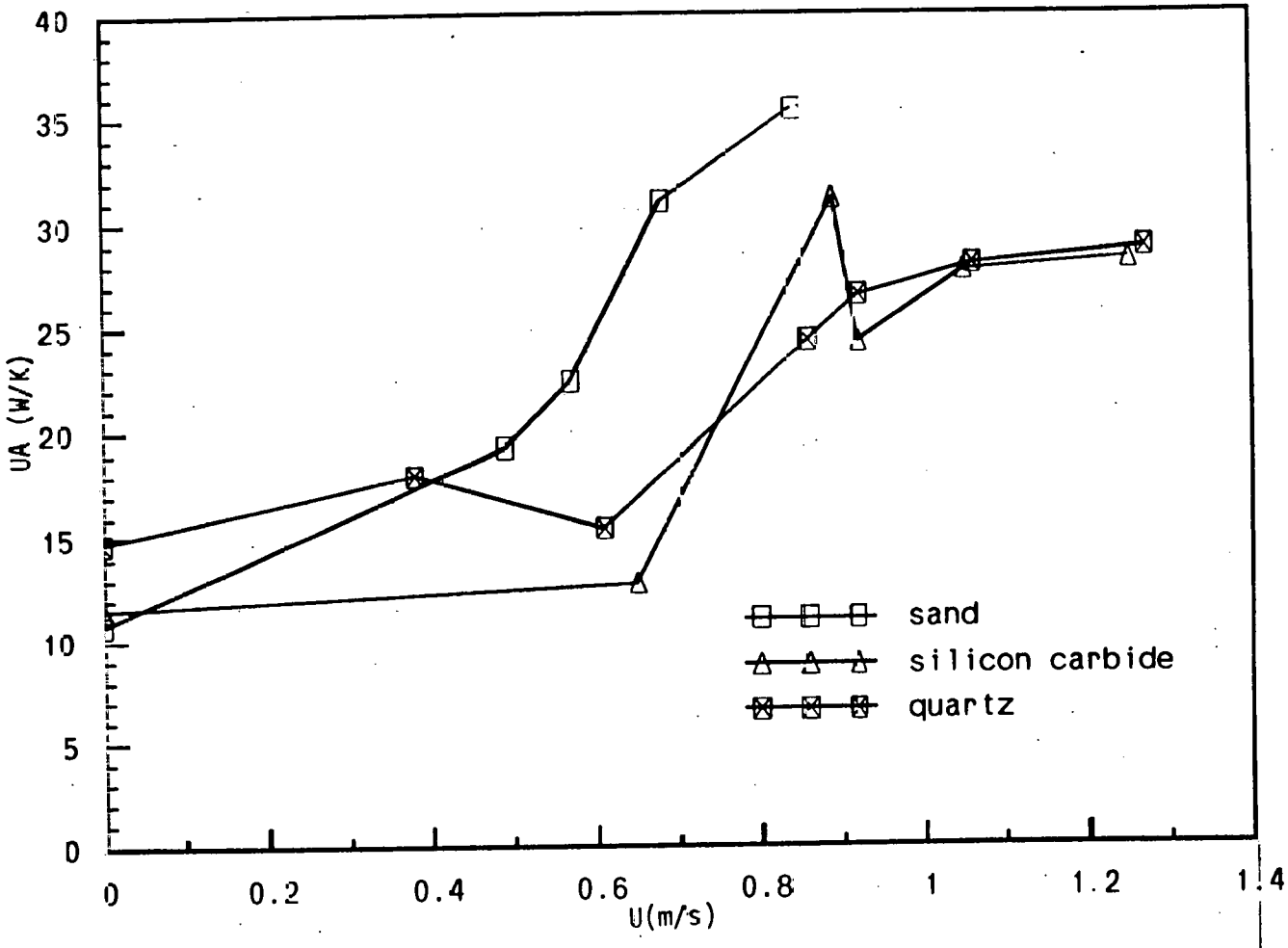

Fig. 19. Effect of particle thermal conductivity.

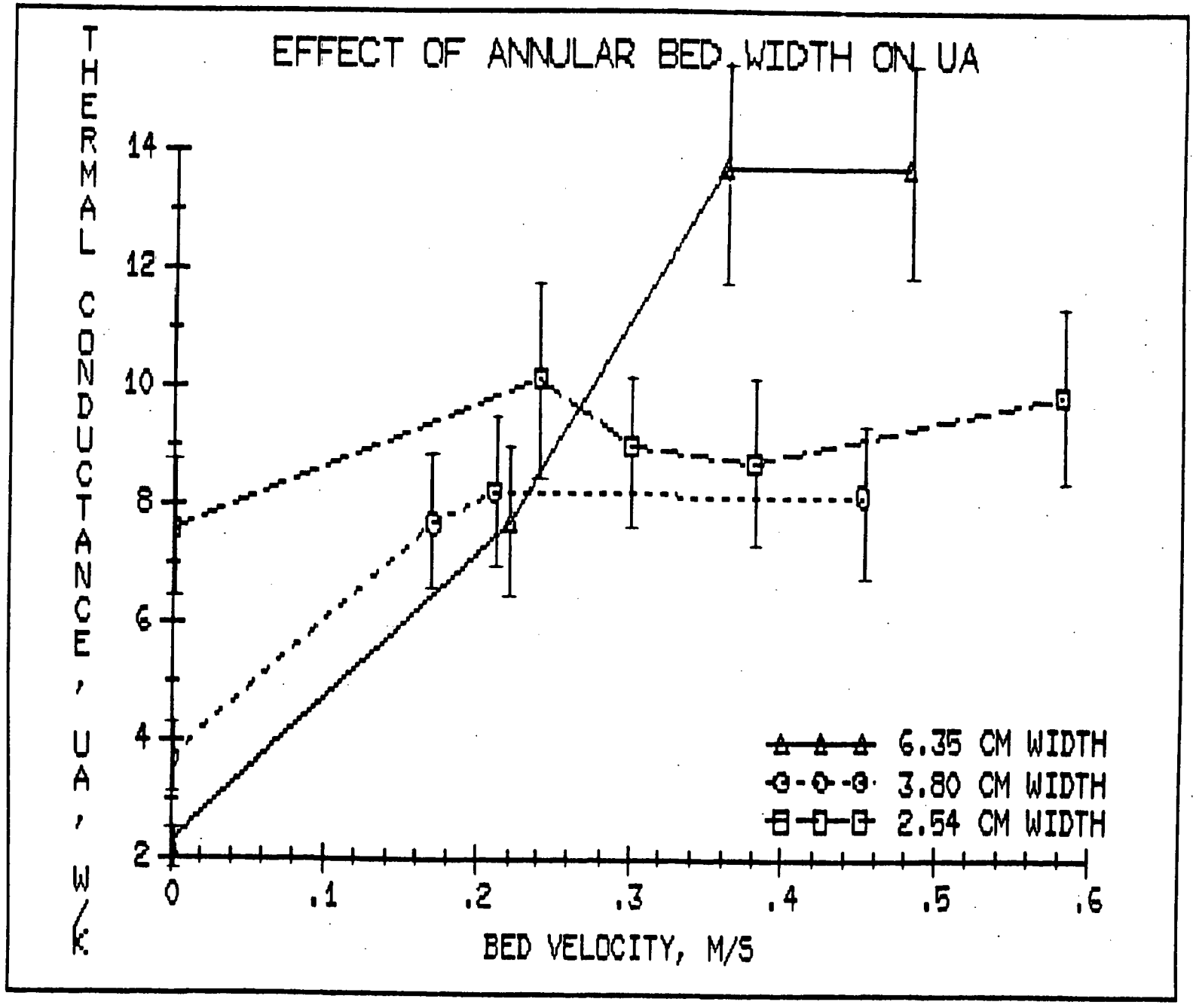

Fig. 20. Effect of annular bed width on UA (experimental data).

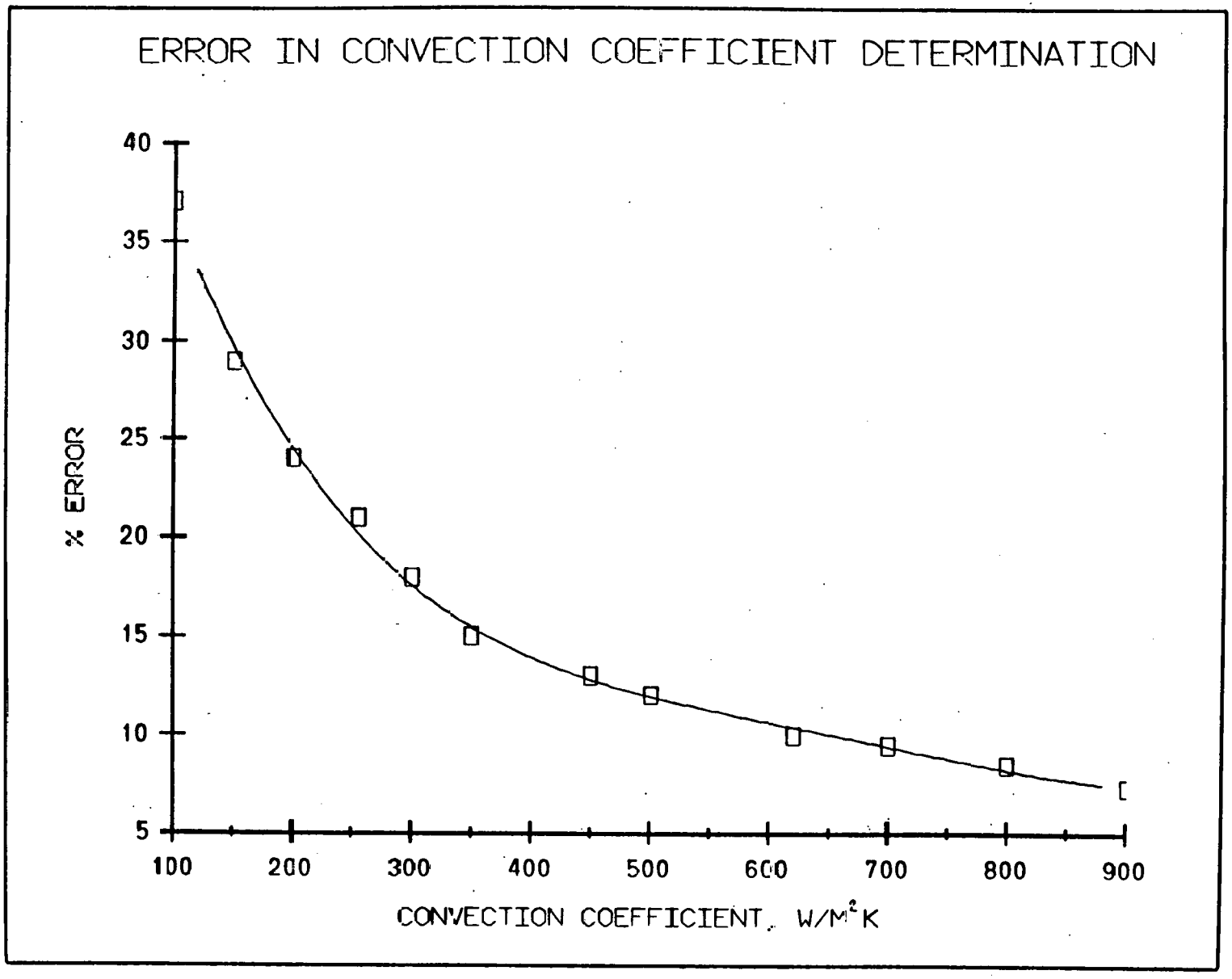

Fig. 21. Error in convection coefficient due to heat conduction along thermocouple wires.

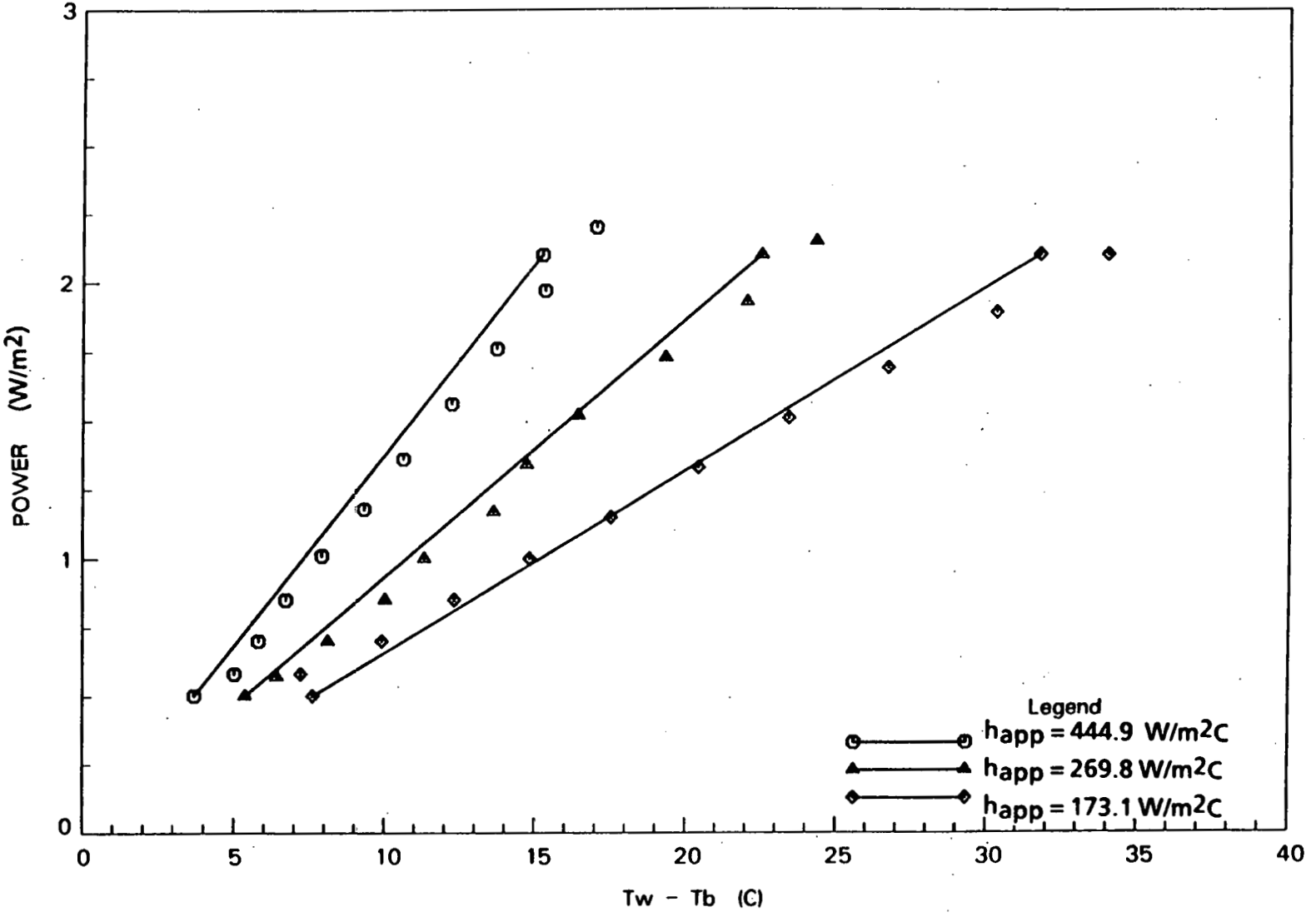

Fig. 22. Comparison of predicted and experimentally determined wire temperatures.

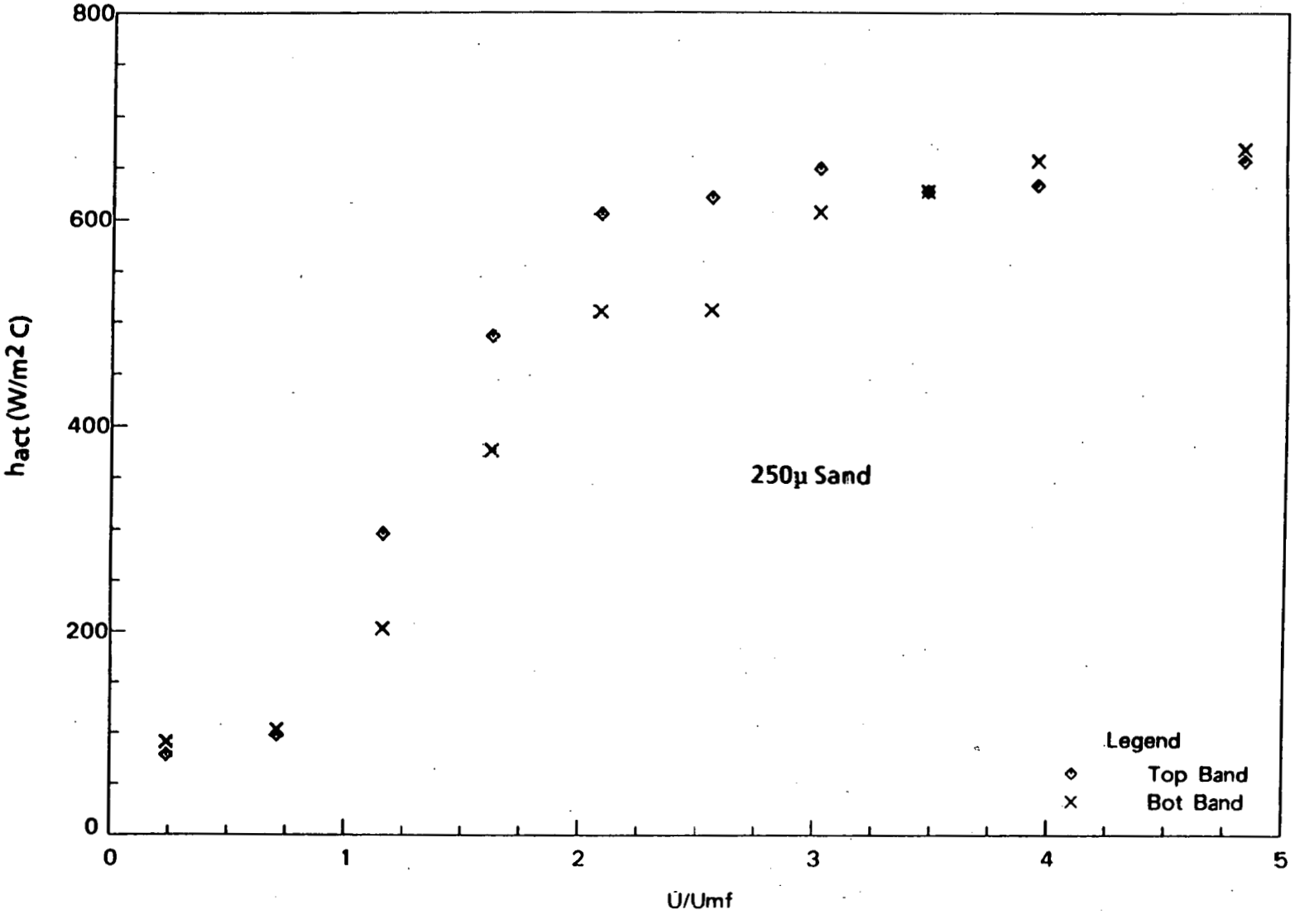

Fig. 23. Convection coefficients for 250 µ sand.

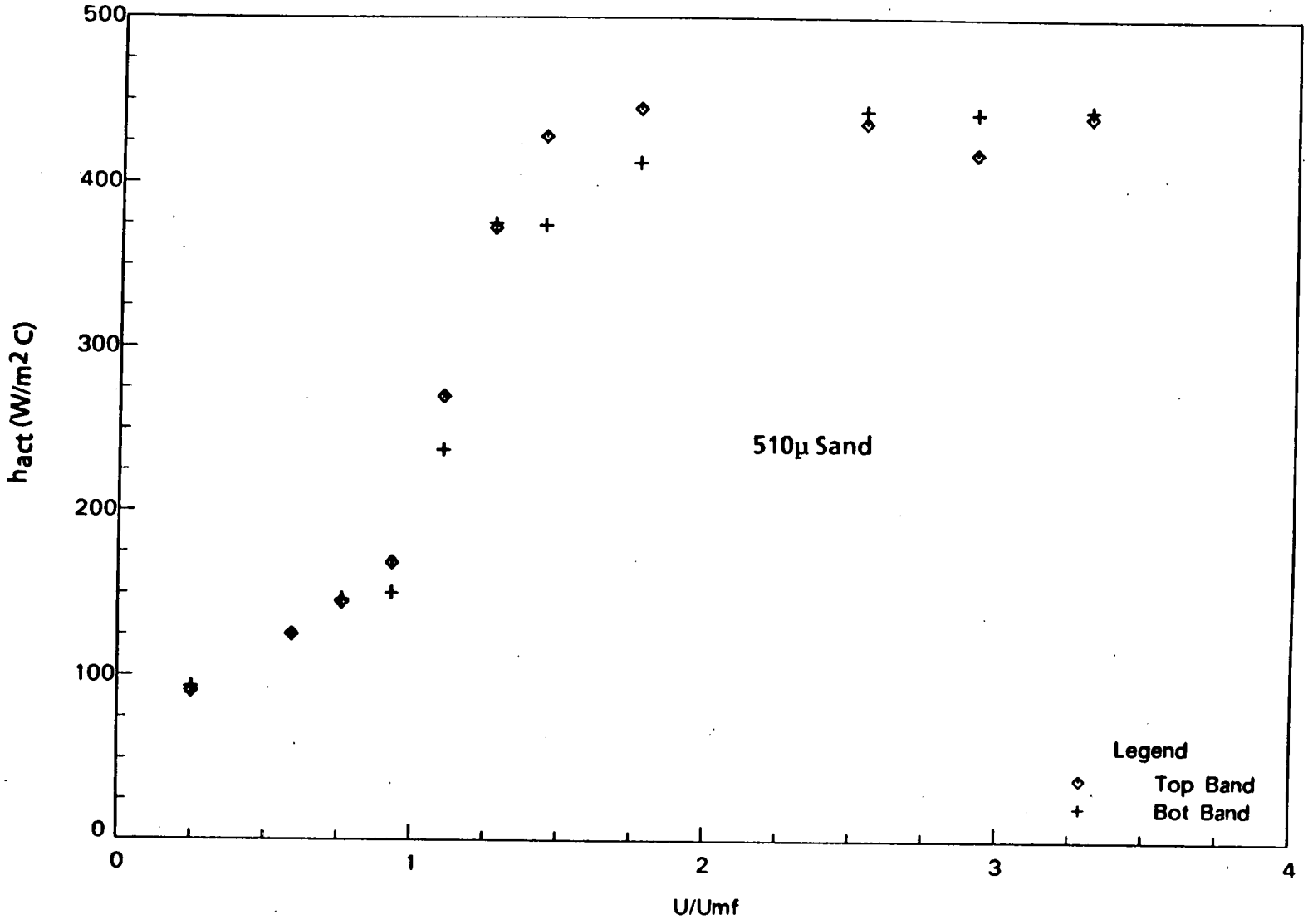

Fig. 24. Convection coefficients for 510 µ sand.

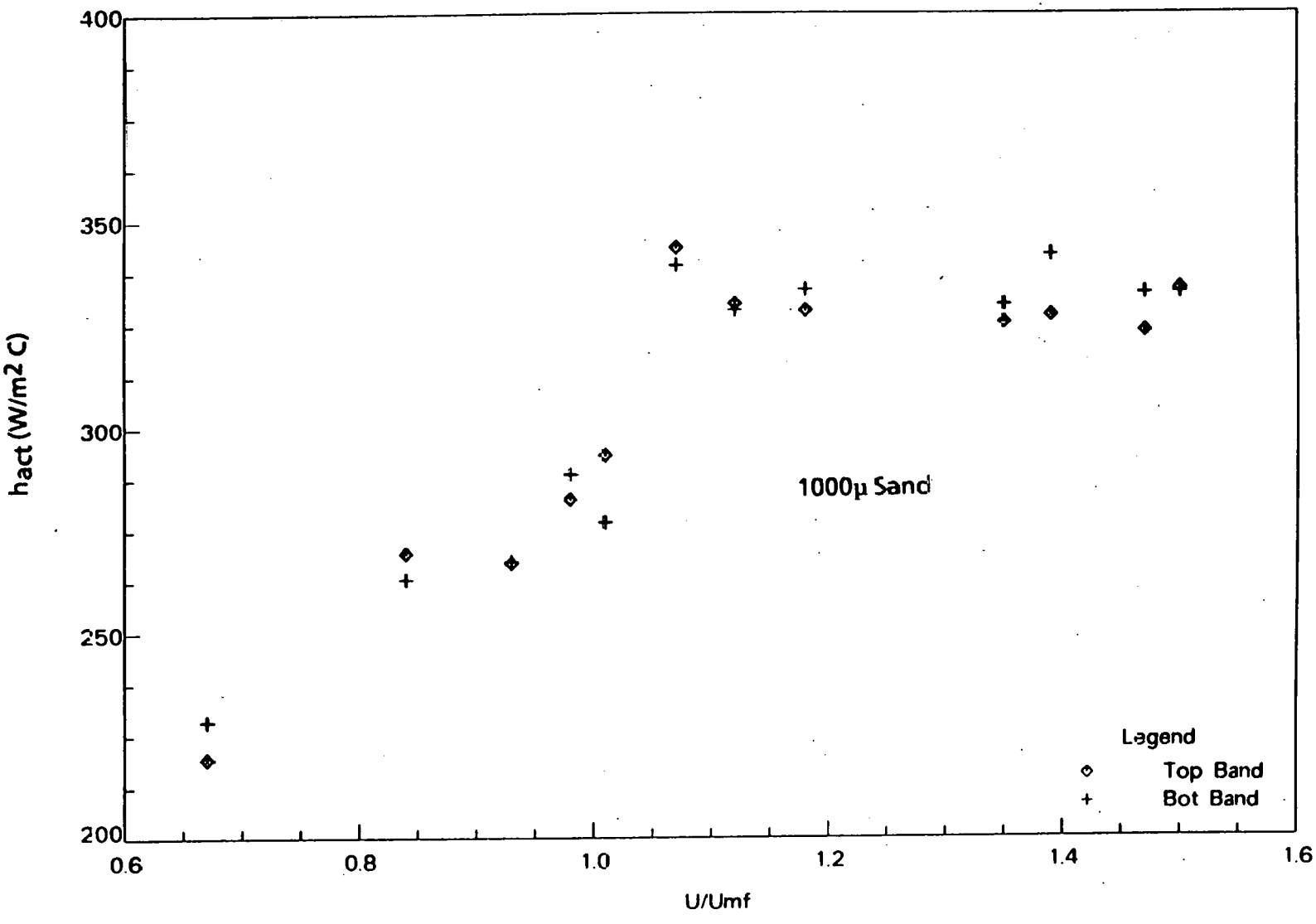

Fig. 25. Convection coefficients for 1000 µ sand.

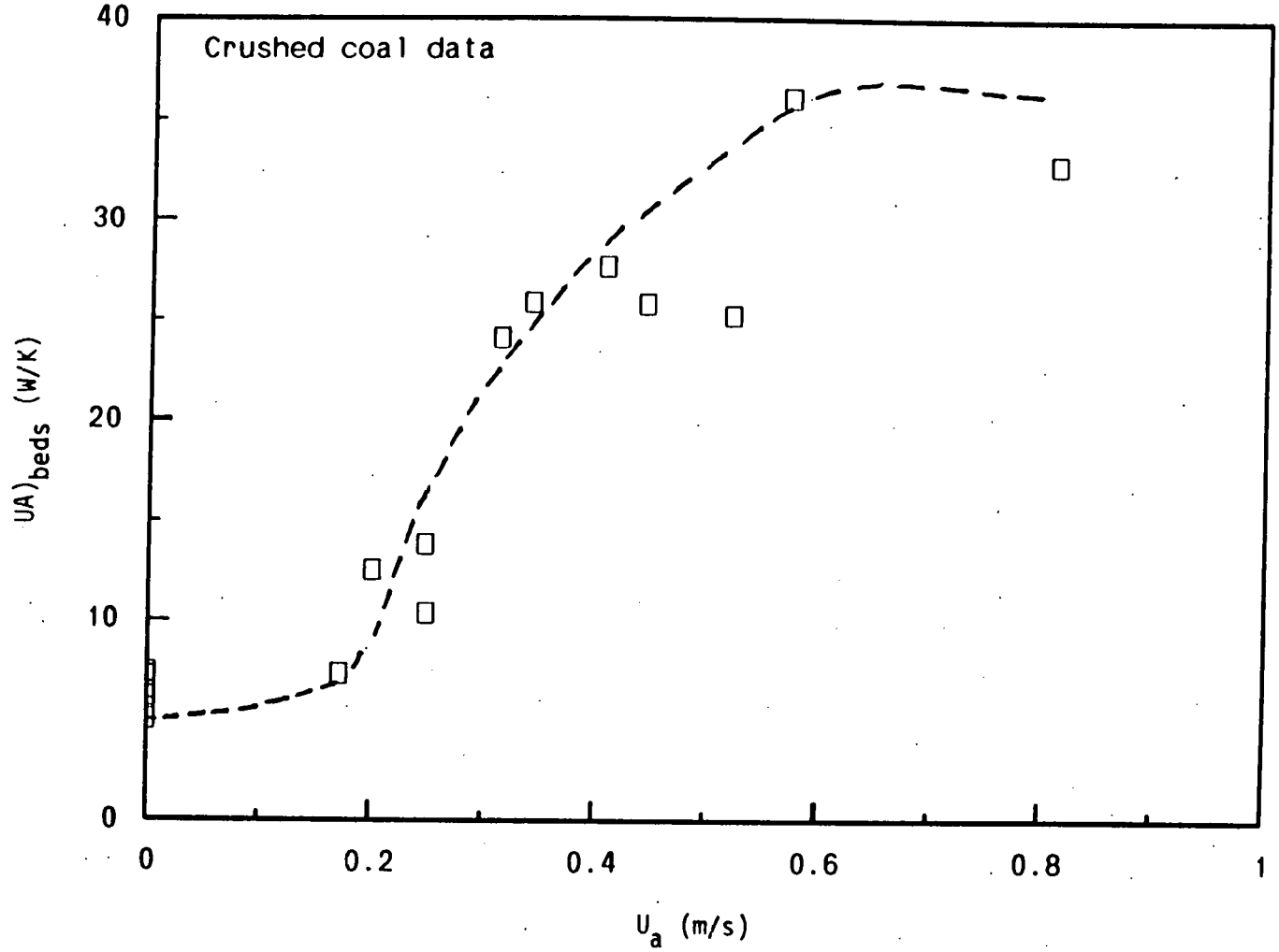

Fig. 26. Effect of angular bed velocity on overall heat transfer coefficient.

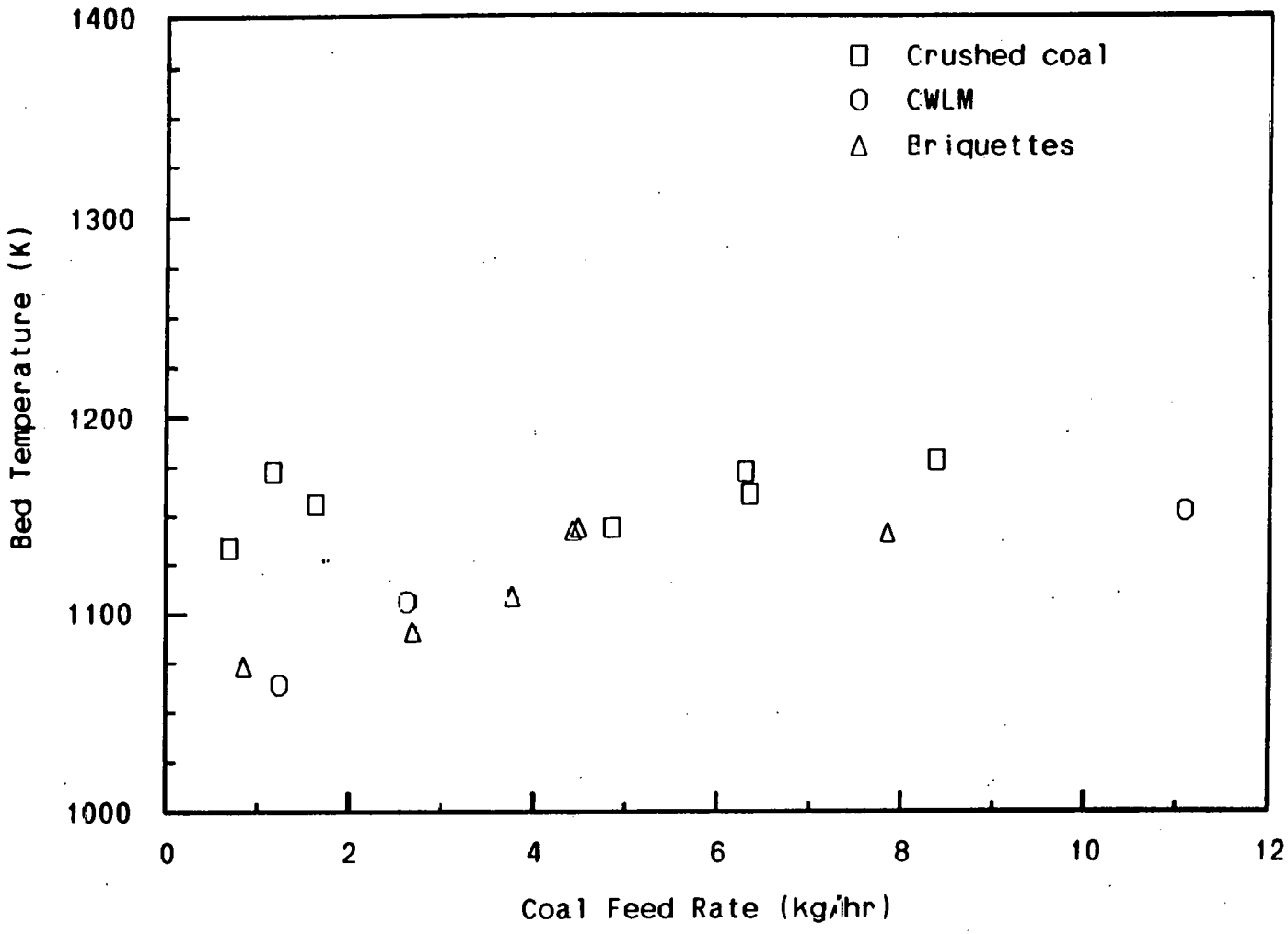

Fig. 27. Combustion bed temperature vs. coal feed rate.

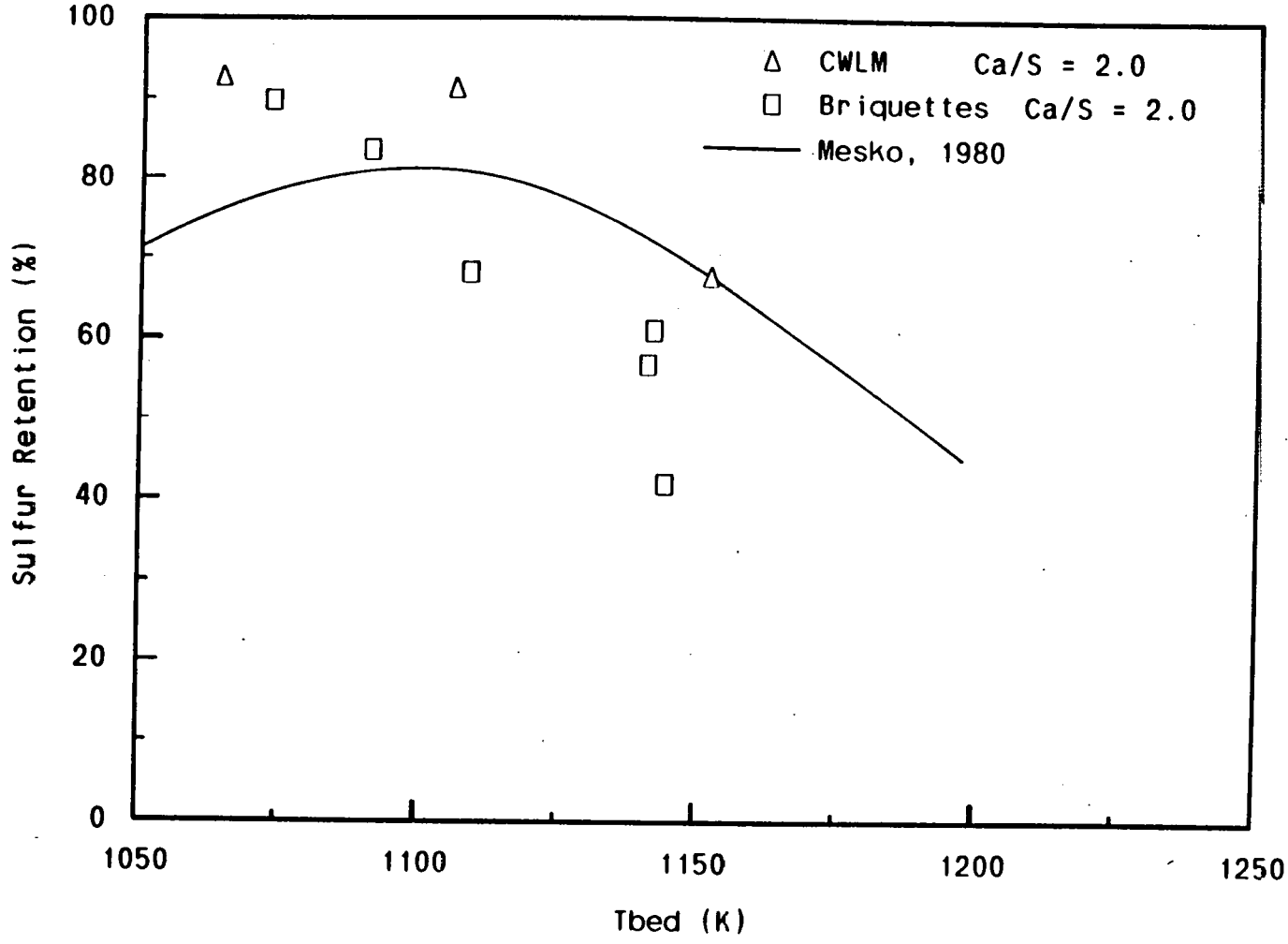

Fig. 28. Sulfur retention vs. combustion bed temperature.

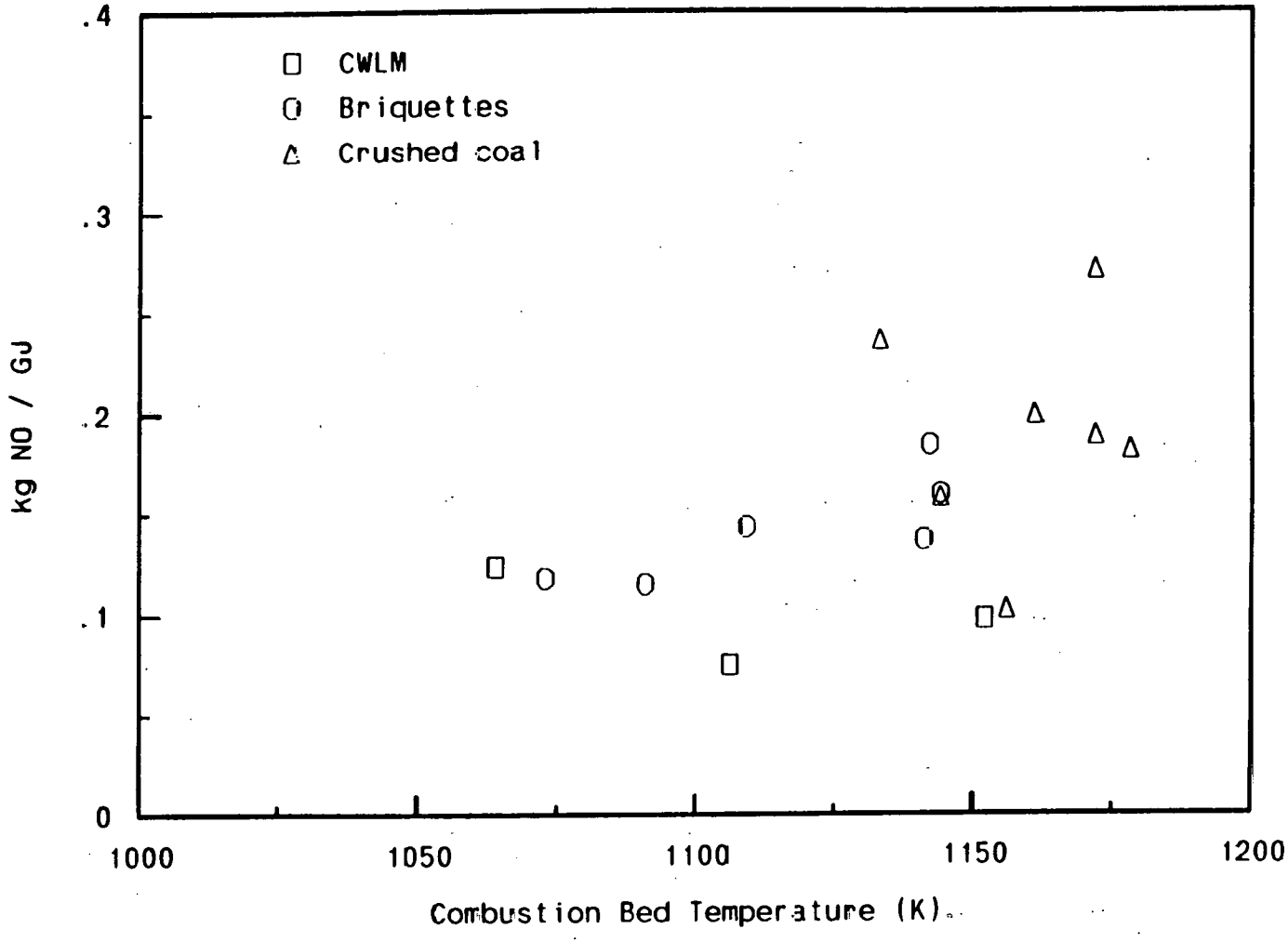

Fig. 29. Nitrogen oxide emission vs. combustion bed temperature.

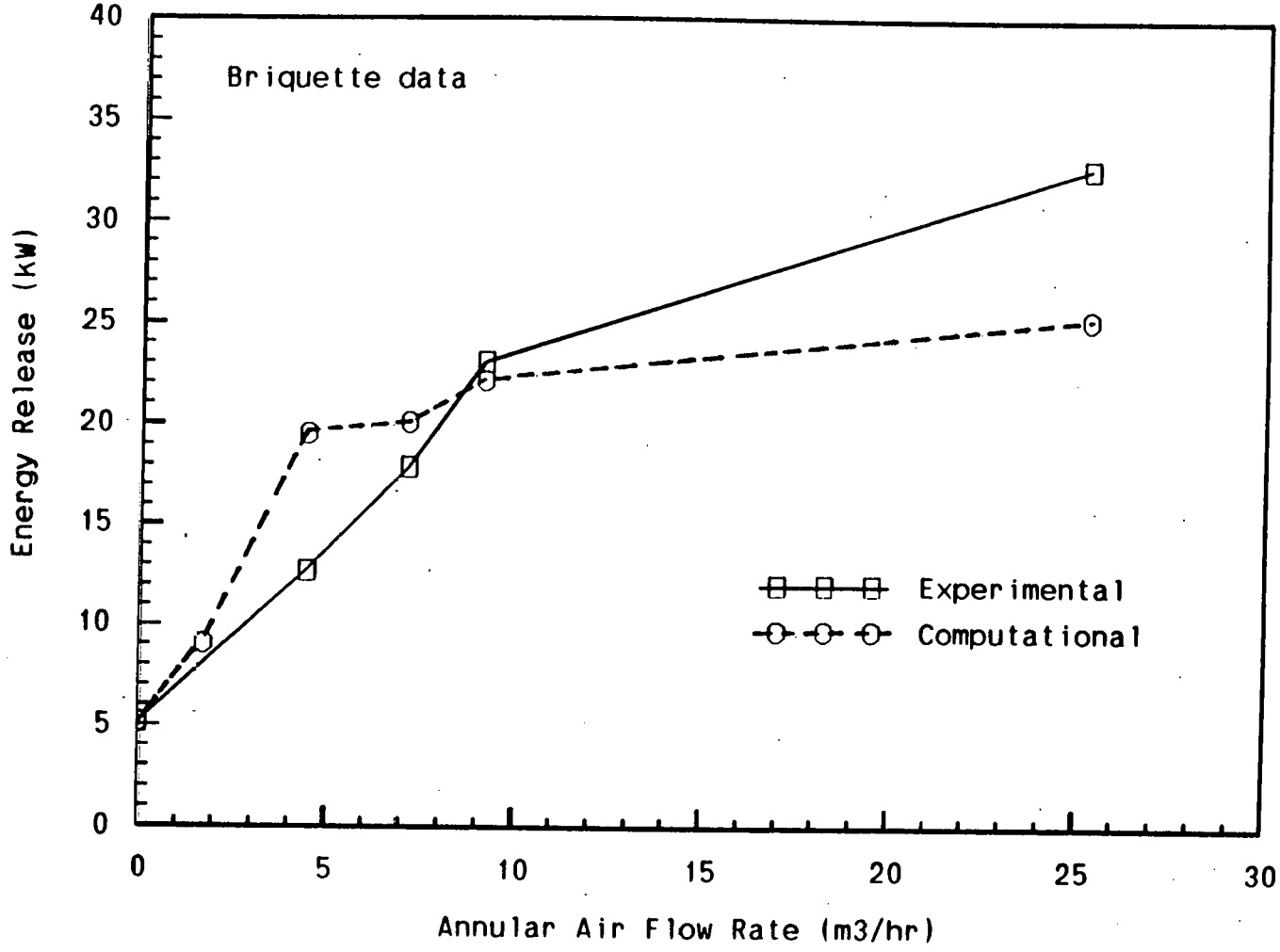

Fig. 30. Combustion rate vs. annular air flow rate.

X. APPENDIX

This appendix includes a computer program for calculating heat transfer in two-bed combustors.

```
C     This program solves the system of equations for temperature
C     and heat transfer in a two-bed fluidized bed combustor.

C     The equations for calculating heat transfer coefficients in
C     a fluidized bed are contained in the subroutine COEFF.


C     LAST UPDATE:  12/15/88 by Jim Foley


      IMPLICIT REAL*8 (A-H, O-Z)
      DIMENSION VAL(10), ERR(10)
      REAL*8 KMF,KEO,KS,KPB
      CHARACTER*3 HUH

C     INPUT DATA FOR FLUIDIZED BED :


      DATA AORIF, EPSB, EPSIW, EPSOW, EPSP,
     *     DPC, DPA, CPS, EMFA, EMFC,
     *     EOA, EOC, RM, RHOS, RMUW,
     *     HFG, G, RHOL, RHOV, SIG,
     *     CPW, CSF, PRANW
     *   /2.0268D-04, 0.8D0, 0.40D0, 0.40D0, 0.90D0,
     *     1000.0D-06, 300.0D-06, 800.0D0, 0.476D0, 0.476D0,
     *     0.40D0, 0.40D0, 6.0D0, 2600.0D0, 279.0D-06,
     *     2257.0D+03, 9.806D0, 957.9D0, 0.5955D0, 58.9D-03,
     *     4217.0D0, 0.0130D0, 1.76D0 /


      FLAGMF = 0
      IDIAG = 0
      ZMAXA = 0.3556D0
      ZMAXC = -1.0D0
      TNOT = 294.0D0

      PRINT*,'WHAT IS THE ANNULAR BED PARTICLE DIAMETER ? '
      PRINT*,'   IN MICRONS : '
      PRINT*,' '
      READ(5,*) DPA
      DPA = DPA*1.0D-06
      PRINT*,'WHAT IS THE CENTRAL BED PARTICLE DIAMETER ? '
      PRINT*,'   IN MICRONS : '
      READ(5,*) DPC
      DPC = DPC*1.0D-06
 3    PRINT*,' INPUT CENTRAL BED DIAMETER (IN INCHES) : '
      PRINT*,' FOR EXAMPLE:  5,7, OR 8 INCHES  . . . '
      PRINT*,' '
      READ(5,*) DC
      DC = DC*0.02540D0
C
      DA = 0.254D0
      BOILC = RMUW*HFG*DSQRT( G*(RHOL-RHOV)/SIG )*
     *        ( (CPW/(CSF*HFG*PRANW))**3 )
      DAVE = 0.50D0*(DC+DA)
      PI = 4.0D0*DATAN(1.0D0)
      AWIDTH = DA - DC
      CWIDTH = DC - 0.006350D0
```

```
      ABAREA = (  DA*DA - DC*DC )*PI/4.0D0
      CBAREA = PI*CWIDTH*CWIDTH/4.0D0
      AHDEAD = 0.229D0
      CBDEAD = 0.178D0
      CPNOT = 1.007D03
      HJACK = 0.2286D0
      RHONOT = 1.19D0
      GPMW = 1.50D0
      APARTS = ABAREA*AHDEAD*16.0D0/(3.0D0*DPA)

      RJUNK1 = DPC*1.0D+06
      RJUNK2 = DPA*1.0D+06
      WRITE(6,450)
      WRITE(6,451) CWIDTH,RJUNK1,CBDEAD
      WRITE(6,452) RJUNK2,AHDEAD
      WRITE(6,453)

450       FORMAT('1',X,'TWO-BED FLUIDIZED BED COMBUSTOR SIMULATION')
451       FORMAT(' ',/,/,/,X,'COMB BED DIAMETER : ',F6.3,' m',/,X,
     *      'COMB BED PARTICLE SIZE : ',F7.1,' MICRONS',/,X,
     *      'COMB BED DEAD HEIGHT :',F6.3,' m')
452       FORMAT(' ',/,X,'ANNULAR BED PARTICLE SIZE : ',F7.1,' MICRONS'
     *      ,/,X, 'ANN BED DEAD HEIGHT : ',F6.3,' m',//,X,
     *      'UNITS ARE AS FOLLOWS: ',/,6X,'U (m/s)  Q (kW)  V (scfm) ',
     *      'UA (W/K)  h (W/m2K)   T (K)   A/F (scfm/kW)',/,X )
453       FORMAT('0',/,X,T28,'COMB BED',T47,'HT BED',/,
     *      T9,'TB',T17,'QIN',T27,'A/F',T33,'U/UMF',T45,'V',T51,'U/UMF',
     *      T60,'  QH2O ',T69,'UABEDS',//,T6,'TIW',T15,'TP',T21,
     *      'THTAIR',T32,'TOW',T41,'HB',T50,'HA',T57,'QCAIR',
     *      T66,'QHTAIR' )



5     CONTINUE

      FLAGMF = 0

      PRINT*,'  INPUT ANNULAR AIR (scfm)  :'
      READ(5,*) ASCFM

7     PRINT*,'DO YOU KNOW :  1)  TBED AND SCFM '
      PRINT*,'               2)  QIN AND SCFM '
      PRINT*,'               3)  TBED AND A/F '

      READ(5,*) II

      IF (II.EQ.1) THEN

         PRINT*,'INPUT TBED'
         READ(5,*) TB
         PRINT*,'INPUT CSCFM'
         READ(5,*) CSCFM
         QIN = 20000.0D0

      ELSE

         IF (II.EQ.2) THEN

            PRINT*,'INPUT QIN (kW)'
            READ(5,*) QIN
```

```
            QIN=QIN*1.0D+03
            PRINT*,'INPUT CSCFM'
            READ(5,*) CSCFM
            TB = 1144.0D0

         ELSE

            IF (II.EQ.3) THEN

               PRINT*,'INPUT TBED'
               READ(5,*) TB
               PRINT*,'INPUT A/F RATIO  (scfm/kW) '
               READ(5,*) AFRAT
               QIN = 20.0D0
               CSCFM = AFRAT*QIN
               QIN = QIN*1.0D+03

            ELSE

               PRINT*,'-> -> -> -> ->  MUST BE 1,2,OR 3 . . . .'
               GOTO 7

            ENDIF
         ENDIF
      ENDIF


C     CALCULATE VALUES OF U :

      UBIW = 5.68D-08 / ( 1.0D0/EPSB+1.0D0/EPSIW-1.0D0 )
      UPIW = 5.68D-08 / ( 1.0D0/EPSP+1.0D0/EPSIW-1.0D0 )
      UPOW = 5.68D-08 / ( 1.0D0/EPSP+1.0D0/EPSOW-1.0D0 )



      TOL = 0.00005D0
      TW = 300.0D0
      TOW = 373.1D0
      THTAIR = 670.0D0
      TP = 700.0D0
      TIW = 900.0D0

      UHTNOT = ASCFM*4.719D-04/ABAREA
      UNOT = CSCFM*4.719D-04/CBAREA

      UHTAIR = UHTNOT*THTAIR/TNOT
      UAIR = UNOT*TB/TNOT


      IF (ASCFM.EQ.0.0D0) GOTO 777



      ITER = 0

 10   CONTINUE

C     ****************** START ITERATING   ****************************
```

```
      IF (II.EQ.3) CSCFM = AFRAT*QIN*1.0D-03
      UNOT = 4.719D-04*CSCFM/CBAREA
      UAIR = UNOT*TB/TNOT
      UHTAIR = UHTNOT*THTAIR/TNOT

C     DETERMINE HEAT TRANSFER COEFFICIENTS FOR CENTRAL AND ANNULAR BEDS:

C     HEAT TRANSFER BED:

      IF (FLAGMF.NE.0) UHTAIR = 0.8*UMFA


      CALL COEFF (THTAIR, UHTAIR, TP, AHDEAD, DPA, CPS,
     *     AWIDTH, EMFA, EOA, EBA, EA, RM, AORTF, RHOS, HGC, HPC,
     *     HGP,HA, RHOHT, CPHT, IDIAG, ZMAXA, AHITE, UMFA )

C
C     TO AVOID PROBLEMS WITH THE MIN FLUID. DISCONTINUITY,
C     SET U = .8 UMF ONCE U BECOMES LESS THAN UMF.

      IF (FLAGMF.NE.0) GOTO 277
      IF (UHTAIR.LT.UMFA) FLAGMF=1
  277 IF (FLAGMF.NE.0) UHTAIR = 0.8*UMFA



C     COMBUSTION BED


      CALL COEFF (TB, UAIR, TB, CBDEAD, DPC, CPS,
     *     CWIDTH, EMFC, EOC, EBC, EC, RM, AORIF, RHOS, DUM, DUMM,
     *     DUUM, HB, RHOAIR, CPAIR, IDIAG, ZMAXC, CBHITE, UMFC )


      IF (II.EQ.3) CSCFM = AFRAT*QIN*1.0D-03
      UNOT = 4.719D-04*CSCFM/CBAREA
      UAIR = UNOT*TB/TNOT

      ITER = ITER + 1

      VAL (1) = TOW
      VAL (2) = TP
      VAL (3) = TIW
      VAL (4) = TB

      FLUX = HPC*(TP-TOW) + HGC*(THTAIR-TOW)
     *   + UPOW*( (TP**4) - (TOW**4) )

      TOW = 373.0D0 + (FLUX/BOILC)**(1.0D0/3.0D0)

      CPHTAV = (CPNOT + CPHT)/2.0D0
      CONVEC = UHTAIR*RHOHT*CPHTAV*ABAREA

      TP =  (    ( HA + UPIW*(TIW*TIW + TP*TP)*(TIW+TP) )*DC*TIW  +
     *     ( HA + UPOW*(TOW*TOW + TP*TP)*(TOW+TP) )*DA*TOW  +
     *    CONVEC*TNOT/(PI*HJACK)     )  /
     *    (      (HA + UPIW*(TIW*TIW + TP*TP)*(TIW+TP))*DC +
     *    ( HA + UPOW*(TOW*TOW + TP*TP)*(TOW+TP) )*DA    +
     *    CONVEC/(PI*HJACK)    )
```

```
      THTAIR = TP

      TIW = ( HB*TB + HGC*THTAIR + HPC*TP + UBIW*(TB*TB +
     *   TIW*TIW)*(TB + TIW)*TB + UPIW*(TP*TP + TIW*TIW)*(TP
     *   + TIW)*TP ) / ( HB + HGC + HPC + UBIW*(TB*TB + TIW*
     *   TIW)*(TB + TIW) + UPIW*(TP*TP + TIW*TIW)*(TP + TIW) )

      CPAVE = (CPNOT + CPAIR)/2.0D0

      IF (II.EQ.2) THEN

         TB = ( QIN + PI*DC*HJACK*TIW*( HB + UBIW*
     *     (TIW*TIW + TB*TB)*(TIW+TB) ) +
     *     RHONOT*UNOT*CPAVE*CBAREA*TNOT ) /
     *     (   PI*DC*HJACK*( HB + UBIW*(TIW*TIW+TB*TB)*
     *     (TIW+TB) ) + ( RHONOT*UNOT*CPAVE*CBAREA )   )

      ELSE

         QIN = PI*DC*HJACK*( HB*(TB-TIW) + UBIW*(TB**4-TIW**4) )
     *         + RHONOT*UNOT*CPAVE*CBAREA*(TB-TNOT)

         IF (II.EQ.3) CSCFM = AFRAT*QIN*1.0D-03

      ENDIF


C     FIND DIFFERENCES AND TEST FOR CONVERGENCE :

      ERR(1) = DABS (TOW - VAL(1))
      ERR(2) = DABS (TP - VAL(2))
      ERR(3) = DABS (TIW - VAL(3))
      ERR(4) = DABS (TB - VAL(4))
      ERTOP = 0.0D0
      DO 100 I = 1,4
         IF (ERR(I) .GT. ERTOP) ERTOP = ERR(I)
  100 CONTINUE


      IF (ITER .GT. 500) GOTO 20
      IF (ERTOP .GT. TOL) GOTO 10

      PRINT*,'NUMBER OF ITERATIONS IS   :',ITER
      GOTO 55


   20 PRINT*,'   ITERATIONS EXCEEDED 500
      CONTINUE

   55 CONTINUE


C          **********     SOLUTION HAS CONVERGED     **********


      RATIOA = UHTAIR/UMFA
      RATIOC = UAIR/UMFC
```

```
      QIN = QIN*1.0D-03
      QCWALL = HB*HJACK*PI*DC*(TB-TIW)*1.0D-03
      QCAIR  = RHONOT*UNOT*CBAREA*CPAVE*(TB-TNOT)*1.0D-03
      QCRAD  = UBIW*(TB**4-TIW**4)*HJACK*PI*DC*1.0D-03
      QARADI = UPIW*(TIW**4-TP**4)*HJACK*PI*DC*1.0D-03
      QWALLI = HA*HJACK*PI*DC*(TIW-TP)*1.0D-03
      QWALLO = HA*HJACK*PI*DA*(TP-TOW)*1.0D-03
      QARADO = UPOW*(TP**4-TOW**4)*HJACK*PI*DA*1.0D-03
      QHTAIR = RHONOT*UHTNOT*ABAREA*CPHTAV*(THTAIR-TNOT)
     *         *1.0D-03
      QH2O = FLUX*HJACK*PI*DA*1.0D-03


      GOTO 888

  777 CONTINUE
C
C
C     THIS SECTION WILL CALCULATE THE AMOUNT OF HEAT TRANSFER
C     IF THERE IS NO AIR FLOWING IN THE HEAT TRANSFER BED.
C


      UAIR = UNOT*TB/TNOT

C     START ITERATING

      ITER = 0

  789 CONTINUE


      CALL COEFF (TB, UAIR, TB, CBDEAD, DPC, CPS,
     *     CWIDTH, EMFC, EOC, EBC, EC, RM, AORIF, RHOS, DUM, DUMM,
     *     DUUM, HB, RHOAIR, CPAIR, IDIAG, ZMAXC, CBHITE, UMFC )


      VAL(1) = TB
      VAL(2) = TIW

      KPB = 0.20D0 + 4.10D-04*TB

      CONDUC = 2.0D0*KPB/( DC*(DLOG(DA/DC)) )

      TIW = ( HB*TB + UBIW*(TB*TB+TIW*TIW)*(TB+TIW)*TB +
     *    CONDUC*TOW ) / ( HB + UBIW*(TB*TB+TIW*TIW)*(TB+TIW) +
     *    CONDUC )


      QCOND = HJACK*PI*DC*( HB*(TB-TIW) + UBIW*(TB**4-TIW**4) )


      TOW = ( QCOND/(BOILC*PI*DA*HJACK) )**(1.0D0/3.0D0) + 373.0D0

      TP = 0.50D0*(TIW+TOW)

      THTAIR = TP

      CPAVE = (CPNOT+CPAIR)/2.0D0
```

```
      IF (II.EQ.2) THEN

         TB = ( QIN + PI*DC*HJACK*TIW*( HB + UBIW*
     *      (TIW*TIW + TB*TB)*(TIW+TB) ) +
     *      RHONOT*UNOT*CPAVE*CBAREA*TNOT ) /
     *      (   PI*DC*HJACK*( HB + UBIW*(TIW*TIW+TB*TB)*
     *      (TIW+TB) ) + ( RHONOT*UNOT*CPAVE*CBAREA )   )

      ELSE

         QIN = QCOND + RHONOT*UNOT*CPAVE*(TB-TNOT)*CBAREA
         IF (II.EQ.3) CSCFM = AFRAT*QIN*1.0D-03
         UNOT = CSCFM*4.719D-04/CBAREA
         UAIR = UNOT*TB/TNOT

        END IF


        ITER = ITER + 1

C       CHECK FOR CONVERGENCE

        ERR(1) = DABS (TB - VAL(1))
        ERR(2) = DABS (TIW - VAL(2))
        ERTOP = 0.0D0
        DO 796 I = 1,2
           IF (ERR(I) .GT. ERTOP) ERTOP = ERR(I)
 796    CONTINUE

        IF (ITER.GT.2000) GOTO 797
        IF (ERTOP.GT.TOL) GOTO 789

 797    PRINT*,'ITERATIONS = ',ITER

        QCAIR  = RHONOT*UNOT*CPAVE*CBAREA*(TB-TNOT)*1.0D-03
        QCRAD = UBIW*HJACK*PI*DC*(TB**4-TIW**4)*1.0D-03
        HA = 0.0D-03
        QHTAIR = 0.0D-03
        QH2O = HJACK*PI*DA*BOILC*( (TOW-373.0)**3 )*1.0D-03
        QIN = QIN*1.0D-03
        QCWALL = HB*(TB-TIW)*HJACK*PI*DC*1.0D-03
        QWALLI = HA*(TIW-TP)*HJACK*PI*DC*1.0D-03
        RATIOA = 0.0
        RATIOC = UAIR/UMFC
 888    CONTINUE

        UABEDS = 1000.0D0*(QH2O+QHTAIR)/(TB-TP)
        RJUNK3 = CSCFM*1.69901D0
        RJUNK4 = ASCFM*1.69901D0
        IF (II.NE.3) AFRAT = CSCFM/QIN
        WRITE(6,301) TB,QIN,AFRAT,RATIOC,ASCFM,RATIOA,QH2O,UABEDS
        WRITE(6,302) TIW,TP,THTAIR,TOW,HB,HA,QCAIR,QHTAIR


        WRITE(7,321) QIN,TB,RATIOA,QCRAD,QCAIR,QCWALL
        WRITE(7,322) QWALLI, QARADI, QHTAIR, QWALLO, QARADO
        WRITE(7,323) QH2O
        WRITE(7,324)

          PRINT*,'WANT TO RUN AGAIN?  1 FOR YES, 2 FOR NO
```

```
      READ(5,*) IQUES
      IF(IQUES.EQ.1) GOTO 5

260   FORMAT(1H1,25X,'MAX NUMBER ITERS EXCEEDED IN GAUSS-SEIDEL')
301   FORMAT('0',4X,F7.1,2X,F6.2,3X,2(F7.3,2X,F6.2,3X),F6.2,3X,F6.2 )
302   FORMAT(' ',X,6(F7.1,2X),2(F6.2,3X),/ )
303   FORMAT('0','   TB          TIW        TP          TOW    ITER ')
304   FORMAT('0',4(F7.1,4X),I4 )
321   FORMAT('0',X,'  QIN    TB     RATIO  QCRAD    QCAIR     QCWALL',
     * /,X,F6.2,F9.1,F6.2,3(2X,F6.2) )
322   FORMAT('0',X,' QHTCONVI  QRADI   QHTAIR    QHTCONVO   QRADO ',
     * /,3X,5(F6.2,3X) )
323   FORMAT('0',X,'QH2O = : ',F6.2)
324   FORMAT(' ',X,'**************************************',/)


      STOP
      END



C-------- END OF MAIN ----------------------------------------------------


C     ==========================================================
      SUBROUTINE COEFF (TAIR, UAIR, TP, ZDEAD, DP, CPS,
     *   WIDTH, EMF, EO, EB, E, RM, AORIF, RHOS, HGC, HPC,
     *   HGP, HTOT, RHOAIR, CPAIR, IDIAG, ZMAX, HEIGHT, UMF )
C     ==========================================================


C---------------------------------------------------------------------
C
C   THIS ROUTINE WILL EVALUATE THE HEAT TRANSFER COEFFICIENTS FOR
C   A FLUIDIZED BED FOLLOWING THE MODEL OF XAVIER AND DAVIDSON.
C
C
C   CALL PARAMETERS:
C
C      TAIR              FLUIDIZING AIR TEMPERATURE
C      UAIR              FLUIDIZING AIR SUPERFICIAL VELOCITY
C      TP                FLUIDIZED BED PARTICLE TEMPERATURE
C      ZDEAD             PACKED BED HEIGHT
C      DP                PARTICLE DIAMETER
C      CPS               PARTICLE SPECIFIC HEIGHT
C      DELXA             HYDRAULIC COLUMN DIAMETER
C      EMF               BED VOIDAGE AT MINIMUM FLUIDIZATION
C      EO                BED VOIDAGE OF PACKED BED
C      EB                VOIDAGE CONTAINED IN BUBBLES
C      E                 BED VOIDAGE OF FLUIDIZED BED
C      RM                WALL FILM COEFFICIENT PARAMETER ( 4<M<10 )
C      AORIF             DISTRIBUTOR AREA PER ORIFICE
C      RHOS              PARTICLE DENSITY
C      HGC               GAS-CONVECTION HEAT TRANS. COEFF.
C      HPC               PARTICLE-CONVECTION HEAT TRANS. COEFF.
C      HGP               GAS-TO-PARTICLE HEAT TRANS. COEFF.
C      HTOT              TOTAL HEAT TRANSFER COEFF.
C      RHOAIR            AIR DENSITY ( AT TAIR )
C      CPAIR             AIR SPECIFIC HEAT ( AT TAIR )
```

```
C       IDIAG              DIAGNOSTIC ( PRINT VALUES IF IDIAG=1 )
C       ZMAX               BED CONSRAINT HEIGHT (IF ANY)
C                             ( IF NO CONSTRAINT THEN ZMAX= -1 )
C       HEIGHT             FLUIDIZED BED HEIGHT
C       UMF                SUPERFICIAL AIR VELOCITY AT MIN. FLUIDIZATION
C
C
C
C-----------------------------------------------------------------------


      IMPLICIT REAL*8 (A-H,O-Z)
      REAL*8 KMF,KEO,KS
      DIMENSION TEMP(35),RHO(35),CP(35),RMU(35),RK(35)
      DIMENSION DPP(16),RATIO(16)
      DATA (TEMP(I),I=1,35) /  100.0D0, 150.0D0, 200.0D0, 250.0D0,
     *     300.0D0, 350.0D0, 400.0D0, 450.0D0, 500.0D0, 550.0D0,
     *     600.0D0, 650.0D0, 700.0D0, 750.0D0, 800.0D0, 850.0D0,
     *     900.0D0, 950.0D0, 1000.0D0, 1100.0D0, 1200.0D0, 1300.0D0,
     *     1400.0D0, 1500.0D0, 1600.0D0, 1700.0D0, 1800.0D0, 1900.0D0,
     *     2000.0D0, 2100.0D0, 2200.0D0, 2300.0D0, 2400.0D0, 2500.0D0,
     *     3000.0D0 /
      DATA(RHO(I),I=1,35)/3.5562D0,2.3364D0,1.7458D0,1.3947D0,1.1614D0,
     *     .9950D0, .8711D0, .7740D0, .6964D0, .6329D0, .5804D0,
     *     .5356D0, .4975D0, .4643D0, .4354D0, .4097D0, .3868D0,
     *     .3666D0, .3482D0, .3166D0, .2902D0, .2679D0, .2488D0,
     *     .2322D0, .2177D0, .2049D0, .1935D0, .1833D0, .1741D0,
     *     .1658D0, .1582D0, .1513D0, .1448D0, .1389D0, .1135D0 /
      DATA (CP(I),I=1,35) / 1032.0D0, 1012.0D0, 1007.0D0, 1006.0D0,
     *     1007.0D0, 1009.0D0, 1014.0D0, 1021.0D0, 1030.0D0, 1040.0D0,
     *     1051.0D0, 1063.0D0, 1075.0D0, 1087.0D0, 1099.0D0, 1110.0D0,
     *     1121.0D0, 1131.0D0, 1141.0D0, 1159.0D0, 1175.0D0, 1189.0D0,
     *     1207.0D0, 1230.0D0, 1248.0D0, 1267.0D0, 1286.0D0, 1307.0D0,
     *     1337.0D0, 1372.0D0, 1417.0D0, 1478.0D0, 1558.0D0, 1665.0D0,
     *     2726.0D0 /
      DATA (RMU(I),I=1,35) / 71.1D-7, 103.4D-7, 132.5D-7, 159.6D-7,
     *     184.6D-7, 208.2D-7, 230.1D-7, 250.7D-7, 270.1D-7, 288.4D-7,
     *     305.4D-7, 322.5D-7, 338.8D-7, 354.6D-7, 369.8D-7, 384.3D-7,
     *     398.1D-7, 411.3D-7, 424.4D-7, 449.0D-7, 473.0D-7, 496.0D-7,
     *     530.0D-7, 557.0D-7, 584.0D-7, 611.0D-7,
     *     637.0D-7, 663.0D-7, 689.0D-7, 715.0D-7, 740.0D-7, 766.0D-7,
     *     792.0D-7, 818.0D-7, 955.0D-7 /
      DATA (RK(I),I=1,35)/ 9.34D-3, 13.8D-3, 18.1D-3, 22.3D-3, 26.3D-3,
     *     30.0D-3, 33.8D-3, 37.3D-3, 40.7D-3, 43.9D-3, 46.9D-3,
     *     49.7D-3, 52.4D-3, 54.9D-3, 57.3D-3, 59.6D-3, 62.0D-3,
     *     64.3D-3, 66.7D-3, 71.5D-3, 76.3D-3, 82.0D-3, 92.0D-3,
     *     100.D-3, 106.D-3, 113.D-3, 120.D-3, 128.D-3, 137.D-3,
     *     147.D-3, 160.D-3, 175.D-3, 196.D-3, 222.D-3, 486.D-3 /

C-----------------------------------------------------------------------
C
C   INTERPOLATE TO FIND THE PROPERTIES FROM THE ABOVE TABLES:
C
C-----------------------------------------------------------------------

      PI = 4.0D0*DATAN(1.0D0)
      G = 9.81D0

      DO 1 I = 1, 35
```

```
      IF(TAIR .GE. TEMP(I).AND. TAIR .LT. TEMP(I+1)) GOTO 2
1     CONTINUE
2     XX = (TAIR - TEMP(I)) / (TEMP(I+1) -  TEMP(I))
      CPAIR = XX*( CP(I+1) - CP(I) ) + CP(I)
      RHOAIR = XX*( RHO(I+1) - RHO(I) ) + RHO(I)
      RKAIR = XX*( RK(I+1) - RK(I) ) + RK(I)
      RMUAIR = XX*( RMU(I+1) - RMU(I) ) + RMU(I)



C     THIRD-ORDER POLYNOMIAL FIT FOR AIR PRANDTL NUMBER


      A1 = 7.5083D-04
      A2 = 1.04999D-06
      A3 = 4.1666D-10
      PRANA = .849 - A1*TAIR + A2*(TAIR*TAIR) - A3*(TAIR**3)

C     PARTICLE REYNOLDS NUMBER

      REP = UAIR*RHOAIR*DP/RMUAIR

      ZMF = ZDEAD*(1.0D0-EO)/(1.0D0-EMF)

      HGP = (2.0D0+1.1D0*(REP**0.6D0)*PRANA**(1.0D0/3.0D0))
     *  *RKAIR/DP
      KS = 1.90D0
      RHOCMF = RHOS*(1.0D0-EMF)*CPS
      AR = RHOAIR*(RHOS-RHOAIR)*G*(DP**3)/(RMUAIR*RMUAIR)
      UMF = RMUAIR/RHOAIR/DP*(((1.0D0+5.53D-05*AR)**(0.5)-1.0D0)
     *  *25.7D0)



      KEO = RKAIR*(KS/RKAIR)**(0.28D0-0.757D0*DLOG10(EO)-0.057D0*
     *  DLOG10(KS/RKAIR))
      KMF = KEO+0.1D0*RHOAIR*CPAIR*DP*UMF



      IF(UAIR .LT. UMF) GOTO 50

C     CALCULATE THE CONVECTION COEFFICIENT IF THE BED IS FLUIDIZED

      DB = (0.54D0*(UAIR-UMF)**(0.4D0)*(ZDEAD+4.0D0*DSQRT(AOR1F))
     *  **(0.8D0))/G**(0.2D0)

      PROD = DB/WIDTH

C     BUBBLE RISE VELOCITY:
C
C         IF        PROD > 0.6   SLUG FLOW
C         IF .125 < PROD < 0.6   BUBBLE FLOW WITH WALL EFFECTS
C         IF .125 > PROD         BUBBLE FLOW
C
C
C

      UB = 0.71D0*DSQRT(G*DB)
```

```
      IF( PROD .GE. 0.125D0 .AND. PROD .LE. 0.6D0 )
     *   UB = 1.13D0*0.71D0*DSQRT(G*DB)*DEXP(-PROD)

      IF( PROD .GT. 0.6D0 ) UB = 0.35*DSQRT(G*WIDTH)

      QUANT = UB/(UAIR-UMF+UB)

      EB = 1.0D0 - QUANT

C     CHECK TO SEE IF A HEIGHT CONSTRAINT IS REACHED

      EBMAX = 1.0D0
      IF (ZMAX.GT.0.0D0) EBMAX = 1.0D0 - ( 1.0D0 - EO )*ZDEAD/ZMAX

      IF (EB.GT.EBMAX) THEN

         EB = EBMAX
         QUANT = 1.0D0 - EB

      ELSE

         CONTINUE

      END IF


      E = 1.0D0 - (1.0D0-EB)*(1.0D0-EO)*ZDEAD/ZMF

      HEIGHT = ZMF/QUANT

      HP = 2.0D0*DSQRT(2.0D0*KMF*RHOCMF*(UAIR-UMF)/(PI*DB) )

      HF = RM*RKAIR/DP


      HPC = (1.0D0/(1.0D0/HP+1.0D0/HF))*QUANT

      U=UMF
      HAV=DSQRT(4.0D0*KMF*RHOAIR*CPAIR*U/(PI*HEIGHT))

      HGC = 1.0D0/(1.0D0/HAV+1.0D0/HF)

      HTOT = HPC + HGC

      GOTO 99


C     CALCULATE GAS CONVECTION WHEN THE BED IS UNFLUIDIZED


 50   E = EO
      HPC=0.0D0
      HF = RM*RKAIR/DP
      U = UAIR
      HAV = DSQRT(  (4.0D0*KMF*RHOAIR*CPAIR*U)/(PI*ZDEAD)  )
      IF (U.EQ.0.0D0) THEN
          HGC = 0.0D0
      ELSE
          HGC = 1.0D0/(1.0D0/HAV+1.0D0/HF)
```

```
      END IF

      HTOT = HGC


C     DIAGNOSTIC PRINT

 99   IF (IDIAG .EQ. 1)
     *   WRITE(6,*) 'UMF= ',UMF,'  HGC= ',HGC,'  HPC= ',HPC,
     *    '  HGP= ',HGP,'  HTOT= ',HTOT,'  --- SUBROUTINE ---'


      RETURN
      END

C---------------------- END OF SUBROUTINE "COEFF" --------------------
```

DOE/MC/23248-2709

DEVELOPMENT OF A NEW METHOD FOR IMPROVING LOAD TURNDOWN IN FLUIDIZED BED COMBUSTORS

USDOE